HIGH GAIN PARAMETRIC PROCESSES IN QUASI-PHASE-MATCHING PROTON-EXCHANGE LITHIUM NIOBATE WAVEGUIDES

A DISSERTATION

SUBMITTED TO THE DEPARTMENT OF APPLIED PHYSICS

AND THE COMMITTEE ON GRADUATE STUDIES

OF STANFORD UNIVERSITY

IN PARTIAL FULFILLMENT OF THE REQUIREMENTS

FOR THE DEGREE OF

DOCTOR OF PHILOSOPHY

Xiuping Xie

September 2006

© Copyright by Xiuping Xie 2006
All Rights Reserved

I certify that I have read this dissertation and that, in my opinion, it is fully adequate in scope and quality as a dissertation for the degree of Doctor of Philosophy.

(Martin M. Fejer) Principal Advisor

I certify that I have read this dissertation and that, in my opinion, it is fully adequate in scope and quality as a dissertation for the degree of Doctor of Philosophy.

(Robert L. Byer)

I certify that I have read this dissertation and that, in my opinion, it is fully adequate in scope and quality as a dissertation for the degree of Doctor of Philosophy.

(Olav Solgaard)

Approved for the University Committee on Graduate Studies.

ABSTRACT

Developments in nonlinear optical materials and solid-state lasers led to rapid progress in nonlinear optics in recent years. Among the many fields of nonlinear optics, $\chi^{(2)}$ parametric processes are among the major tools for generating coherent radiation indispensable in optical communication, spectroscopy and medical applications.

Involving short pulses with high peak power, high gain parametric processes, including optical parametric amplification (OPA) and optical parametric generation (OPG), have been widely used for near- and mid-infrared light sources. Most such research so far has been demonstrated in bulk crystals. On the other hand, waveguides can enhance the beam intensity along the whole device and significantly increase the gain in parametric processes, and have been widely applied in processes such as second-harmonic generation. However a thorough study of the use of waveguides in high-gain parametric processes is absent. This dissertation addresses the challenges in such applications and demonstrates how waveguide structures and quasi-phase-matching (QPM) gratings can be tailored to improve the performance of high gain parametric processes.

We demonstrate high parametric gain for OPA in reverse-proton-exchange lithium niobate waveguides with periodically-poled QPM gratings. Picojoule OPG threshold with picosecond pump pulses near 780 nm is illustrated, which is over two orders of magnitude lower than that in bulk crystal under similar conditions. Furthermore we demonstrate control over the temporal properties of the output products from OPG with picosecond pump pulses near 780 nm. By synthesizing either the QPM gratings or the waveguide structures we demonstrate one order of magnitude smaller time-bandwidth products at designed wavelengths and obtain near transform-limited output from OPG.

We also illustrate mode demultiplexing for OPA using asymmetric Y-junctions, in which the signal and idler in different waveguide modes are separated with a contrast of >27.5 dB. The high gain parametric processes in waveguides may therefore find practical application with the engineerable QPM gratings and waveguide structures.

ACKNOWLEDGMENTS

I might not have been able to finish the projects needed for this dissertation at Stanford without much support and assistance from colleagues, friends and family.

My advisor, Professor Martin M. Fejer has a high standard for research. He has a very broad knowledge in many branches of physical science and is astonishingly good at brainstorming. Several times he pointed out the right direction when I encountered seemingly formidable obstacles in research. I appreciate his patience in clarifying problems to me and the freedom I had in the research. One important lesson I learned from him was "to live actively instead of passively", which had been a problem for me.

I was so lucky to join the Byer-Fejer group and had a nice working environment. The ambitious projects that Professor Robert L. Byer is pursuing (including LIGO and LISA) open a window to me on how science can be done by collaboration with world-wide efforts. Vivian Drew, Tami Reynolds and other Byer-Fejer group administrators were essential for the operation of the group. The research staff~~s~~ (Roger Route, Brian Lantz, Konstantin Vodopyanov, Nora Robertson and Sheila Rowan) were so helpful with their enthusiasm and broad knowledge. Roger was especially helpful in research and I learned a lot from him about high temperature processes.

Professor Shanhui Fan, Professor Olav Solgaard and Professor Steven E. Harris served on my defense committee. Professor Fan also served my qualifying exam and Professor Solgaard read my thesis. I appreciate them for their valuable time and suggestions.

The students in the Fejer group are all talented and enthusiastic in research. I thank Andrew M. Schober for his help in adjusting the Ti:Sapphire laser and thank Carsten Langrock for the auto-correlator he built; both of these apparatus were essential for my projects. I am so grateful to Rostislav V. Roussev, Jonathan R. Kurz and Krishnan R. Parameswaran who taught me the waveguide fabrication techniques. Collaboration with Jie Huang was a pleasure and I appreciate him for reading my dissertation and giving me valuable suggestions. Discussions with David S. Hum, Paulina Kuo, Yin-wen Lee, Mathieu Charbonneau-Lefort, Takashi Saida and many other students and visiting scholars were both insightful and interesting.

Many thanks to the other staff members in Ginzton laboratory, including technical staff, Thomas Carver and Timothy Brand, who helped me so much in device fabrication, and administrative staff, Darla LeGrand-Sawyer, Jenny Kienitz, Amy Hornibrook, Mike Schlimmer, and especially Larry Randall who helped me in the machine shop.

Special thanks to my friends who made my life in Stanford more colorful and saved me from sinking into endless research projects. The adventurous hiking and camping experiences together with Jianyang Xu, Zhigang Xie and other friends were unforgettable. Photography and leisure trips together with Runchuan Zhao, Xueli Liu, Jinsong Liu and other friends were also lots of fun. Last but not least, I cannot thank more to one of my best friends, Jin Yu, for many hours of chat over the phone whenever I felt frustrated.

Although my parents and sister were far away and my only contact with them during the five years at Stanford was weekly phone calls, they never doubted my choice of pursuing a degree in a foreign country and they always encouraged me to follow my own heart. I dedicate this thesis to them.

TABLE OF CONTENTS

Abstract.........v

Acknowledgments.........vii

List of tables.........xiii

List of figures.........xv

Chapter 1: Introduction.........1

- 1.1 Optical frequency conversion and parametric processes.........2
- 1.2 Quasi-phase-matching, periodic poling and synthesis of QPM gratings.........4
- 1.3 Integrated high gain devices: reverse-proton-exchange lithium niobate waveguides and waveguide engineering.........8
- 1.4 Parametric interaction of ultra-short pulses.........14
- 1.5 Previously unsolved problems and overview of this dissertation.........16

Chapter 2: Theory and simulations of parametric processes and optical circuit components in lithium niobate waveguides.........19

- 2.1 Parametric processes in waveguides involving three waves.........19
- 2.2 Theory for pulsed OPG in waveguides.........24
- 2.3 Theory for cascaded $\chi^{(2)}$: $\chi^{(2)}$ processes.........30
    - *2.3.1 Theory for the cascading of SHG and OPA*.........30
    - *2.3.2 Theory for cascaded OPG*.........32
- 2.4 Parametric processes involving different waveguide modes.........37
- 2.5 Coupled mode theory and beam propagation method in waveguides.........39
- 2.6 Waveguide components for optical circuits: bends, directional couplers and asymmetric Y-junctions.........41
    - *2.6.1 Bends*.........41
    - *2.6.2 Directional couplers*.........43
    - *2.6.3 Design and shape optimization of asymmetric Y-junctions*.........44

2.7 Summary of Chapter 2 50

Chapter 3: High parametric gain in reverse-proton-exchange lithium niobate waveguides: OPA and low-threshold OPG..51

3.1 RPE waveguides for OPG and OPA 52

3.2 Continuous-wave OPA using the cascading of SHG and OPA 53

3.3 Experimental results for low-threshold OPG...57

3.4 Summary of Chapter 3 60

Chapter 4: Cascaded optical parametric generation in reverse-proton-exchange lithium niobate waveguides..63

4.1 Effects of cascaded OPG on photon conversion efficiency and pump depletion ..65

4.2 Effects of Cascaded OPG on temporal properties 67

4.2.1 Temporal properties of OPG output at different pump power levels for a 18-mm-long QPM grating...70

4.2.2 Cascaded OPG for QPM-grating lengths ranging from 6 mm to 42 mm at pump powers resulting in a constant photon conversion efficiency 72

4.2.3 Frequency-resolved cross-correlation measurements.................................74

4.2.4 Study of cascaded OPG and conventional OPG under different levels of pump depletion...75

4.2.5 Pulse shapes of the signal and the idler from OPG and the optimized grating length for cascaded OPG 78

4.3 Controlled cascaded OPG with engineered QPM gratings...................................79

4.4 Summary of Chapter 4 and problems in cascaded OPG.......................................82

Chapter 5: Application of quasi-group-velocity-matching in optical parametric generation in reverse-proton-exchange waveguides 85

5.1 Enabling technique: tight bends in RPE waveguides 86

5.1.1 Tight bends fabricated by a RPE process with a deeper proton-exchange depth..86

5.1.2 Tight bends fabricated by adding air trenches along the outside edge 88

5.2 Quasi-group-velocity-matching device design 91

5.3 Experimental results of OPG with QGVM 93
5.4 Summary of Chapter 5 98
Chapter 6: Two-mode optical parametric amplification using asymmetric Y-junctions 99
6.1 Experiments on the shape optimization of asymmetric Y-junctions 100
6.2 Waveguide structure and asymmetric Y-junctions for the OPG experiments 103
6.3 Optical parametric generation involving both TM_{00} and TM_{10} waveguide modes 105
6.4 Summary of Chapter 6 110
Chapter 7: Summary 111
7.1 Summary of contributions 111
7.2 Future directions and applications 113
Bibliography 117

LIST OF TABLES

Number *Page*

Table 5.1: The lowest loss measured for s-bends with air trenches and transition shifts ..89

Table 6.1: The mode contrast comparison between the conventional design and the design optimized by the "shifting" approach for asymmetric Y-junctions in \annealed-proton-exchange waveguides. 101

LIST OF FIGURES

Number *Page*

Figure 1.1: Diagram of sum-frequency generation, a $\chi^{(2)}$ parametric process between three waves....3

Figure 1.2: Diagrams of various $\chi^{(2)}$ parametric processes. The notation is the same as in Fig. 1.1. 4

Figure 1.3: (a) The phase-matching condition in a quasi-phase-matching scheme; (b) The effects of quasi-phase-matching on second-harmonic generation. L_c is the width of the ferroelectric domains. Λ is the period of quasi-phase-matching....5

Figure 1.4: Procedure of lithium niobate wafer poling with electrical fields. 6

Figure 1.5: (a) Diagram of uniform QPM gratings. (b) Demonstration of the QPM peaks for uniform gratings. The horizontal axis is the inverse of the spatial frequency. (c) Comparing effects of first-order and third-order quasi-phase-matching on second-harmonic generation. $L_c = \pi / \Delta k$ is the width of the ferroelectric domains. Λ is the QPM period. 7

Figure 1.6: Comparison of beam propagation in bulk material (confocal focusing condition) and waveguides. 8

Figure 1.7: Fabrication procedure of RPE lithium niobate waveguides....10

Figure 1.8: Various structures on the SiO_2 mask for proton exchange....12

Figure 1.9: Eigenmode profiles along an asymmetric Y-junction in RPE waveguides designed for 1550 nm waves....13

Figure 1.10: (a) Group index of the e-wave versus wavelength in z-cut lithium niobate wafers. δn is the difference between the group indices for 780 nm and 1560 nm waves. (b) Behavior of SHG in PPLN in the presence of GVM; illustrated using a gated mixer. The 780 nm pulse is the SHG of the 1560 nm gate pulse and its output pulse length is wider than the gate pulse due to group-velocity-mismatch. 15

Figure 2.1: Typical diagram of the group velocity walkoffs in optical parametric amplification or optical parametric generation. n_j^g (j = 1, 2, 3) is the group index. L is the QPM grating length. 27

Figure 2.2: Diagram of the cascading of SHG and OPA. 30

Figure 2.3: A diagram of the situation for cascaded OPG involving simultaneous quasi-phase-matching of optical parametric generation and sum-frequency generation between the pump and the signal. 33

Figure 2.4: (a) Diagram of group velocity walkoff for pulsed OPG with the pump group index being between those of the signal and the idler. (b) Diagram of group velocity walkoff for pulsed OPG with the pump group index being higher than those of the signal and the idler. (c) Group indices for the four waves involved in a typical cascaded OPG process like that shown in Fig. 2.3. (d) Diagram of group velocity walkoff for cascaded OPG, showing that the effective group index of the signal is the same as that of the sum frequency and is higher than that of the pump. The nonlinear material is lithium niobate for all the figures here. 35

Figure 2.5: The transform-limited output ranges permitted by cascaded OPG (OPG and SFG between the pump and the signal/idler) in bulk PPLN, if we limit the idler wavelength to <4 μm. The double-line shaded region is for the conventional OPG and the single-line part is the extra region permitted by cascaded OPG. 37

Figure 2.6: The effective index method. Bends are treated as equivalent straight waveguides. 42

Figure 2.7: The mask design of an adiabatic asymmetric Y-junction. The maximum separation d between the two arms is much smaller than the Y-junction length L. 44

Figure 2.8: The simulated refractive index difference between the first and second eigenmodes in typical RPE waveguides. n_0 and n_1 are the effective refractive indices for the first two modes. The solid and dashed curves are for 780 nm and 1550 nm waves respectively..45

Figure 2.9: (a) The shape of our conventional asymmetric Y-junctions. I and II are the center traces of the two arms. (b) Varying the device shape by the "shifting" approach. (c) Varying the device shape by the "stretching" approach. The dashed curves in (b) and (c) are the conventional designs.......46

Figure 2.10: (a) The two coupling coefficients between the first two modes in the conventional design in Fig. 2.9(a); (b) the optimal device shape obtained from the "shifting" approach. 48

Figure 3.1: The configuration for the cascading of SHG and OPA in a RPE waveguide. The pump and signal are combined using a WDM coupler and then launched into a waveguide..54

Figure 3.2: The power spectrum of the cascading of SHG and OPA in a RPE waveguide with a 58-mm-long QPM grating and 175 mW pump power. The gains shown are the internal gains..54

Figure 3.3: The external signal (idler) gain for the cascading of SHG and OPA in a RPE waveguide with a 58-mm-long QPM grating. The solid (dashed) curves are from simulations and the cross (circle) symbols are from measurements for the signal (idler). The black curves are from numerical simulations while the gray curves are from Eq. (2.26) in which pump depletion is neglected...55

Figure 3.4: The experimental setup for waveguide OPG. 57

Figure 3.5: The pump throughput and the internal signal-photon conversion efficiency in single-pass OPG with a 40-mm-long QPM grating in the absence of cascaded OPG. The 1.8-ps-long (FWHM) pump pulse is at 769.6 nm and the signal wavelength is centered at 1350 nm. 58

Figure 3.6: Pump tuning curve of a RPE PPLN waveguide at 120 °C. The dotted curve is a simulation based on our waveguide dispersion model. [49] The circle symbols are measurements. The output wavelength ranges from 1245 nm to 2005 nm for pump wavelength between 768.4 nm and 777.5 nm. 59

Figure 4.1: The internal pump throughput ratio and signal photon conversion efficiency. (a) for a 12-mm-long QPM grating, no cascaded OPG contributes; (b) for an 18-mm-long QPM grating, with contributions from cascaded OPG. 66

Figure 4.2: Illustration of the evolution of different pulse shapes for conventional OPG and cascaded OPG. No propagation loss is considered for the pump. L_0 is the build-up length for the sum-frequency generation in cascaded OPG, defined in Eq. (4.1). 67

Figure 4.3: A diagram of the frequency-resolved cross-correlator. The scan-delay ensures that the pump and signal pulses temporally overlap in the $LiIO_3$ crystal and have maximum efficiency for sum-frequency generation. By replacing the $LiIO_3$ crystal and the silicon detector with a GaAsP photodiode we obtain a cross-correlator without frequency resolvability. 69

Figure 4.4: (a) Power spectra from optical spectrum analyzer traces (b) Cross-correlation traces for the output from OPG in an 18-mm-long QPM grating. Both cover the same pump power range from 0.3 nJ to 1.2 nJ. Note the peak positions in the spectra shift from conventional-OPG to cascaded-OPG with increasing pump pulse energy. Cross-correlation traces also show both products. 71

Figure 4.5: (a) The power spectra and (b) the pulse shapes for the signal from optical parametric generation in lithium niobate waveguides with different QPM-grating lengths. The photon conversion efficiencies for all these traces are ~10% except for the 6-mm-long grating for which it is only 2%. The peak of the conventional OPG products is set as the time zero for all the curves in (b). All the curves are normalized to their maxima. 72

Figure 4.6: (a) The signal power spectrum at a pump power level resulting in a photon conversion efficiency of ~10% with a pump wavelength of 784.4 nm. (b) Pulse shapes of the OPG signal in different wavelength ranges with a 38-nm-wide sinc^2-shape band-pass filter. In order to show the correct relative power the curves in (b) are not normalized. Baselines are shifted to indicate center signal wavelength for each trace, which can be read out from the *x*-axis of (a). On each curve, peak 1 corresponds to the conventional OPG products and peak 2 corresponds to the cascaded OPG products. 74

Figure 4.7: (a) The signal power spectra and (b) the pulse shape for OPG in a waveguide with a 34-mm-long QPM grating. In both figures, the dash-dotted curves (1) correspond to a pump wavelength of 782.8 nm and a photon conversion efficiency of ~20%; cascaded OPG is absent. For the solid (2), dashed (3) and dotted (4) curves, the pump wavelength is 784.4 nm, strong cascaded OPG is present, and they respectively correspond to a total photon conversion efficiency of about 10%, 20% and 30%. All the curves in (a) are normalized to their maxima and the baselines are shifted for a clear comparison in their peak positions, while the curves in (b) are not normalized and hence show a correct comparison in photon conversion efficiencies. 76

Figure 4.8: The pulse shapes of the signal and idler obtained by summing up the frequency-resolved cross-correlation traces from a 42-mm-long QPM grating at a pump power resulting in a photon conversion efficiency of ~20%. The shadowed regions under the curves correspond to the cascaded OPG products while the other regions correspond to the conventional OPG products. 79

Figure 4.9: (a) A diagram of the phase modulated gratings. The center positions of the domains shift by an amount calculated from an optimized periodic phase function. Λ_{ph} is the phase modulation period. (b)(c) Simulated QPM peaks of phase-reversal gratings designed with $\Lambda_1 = \Lambda_{\mathrm{OPG}} = 16.45$ μm, $\delta = 0.4$ μm and $\Lambda_2 = \Lambda_1 - \delta = 16.05$ μm (see text for definition of the symbols). The grating duty cycle is 1/3 and the two peaks near Λ_1 and Λ_2 have the same area in the spatial frequency domain. 80

Figure 4.10: The wavelengths of the signal from the strongest cascaded OPG in different phase-modulated-gratings. δ is a parameter describing the QPM grating design, defined in the text and shown in Fig. 4.9. The solid line is from simulations without any adjustable parameter and the circle symbols are from experimental results...82

Figure 5.1: Diagram for the air trenched s-bends and a photo of s-bends on a chip. In the photo of s-bends, the white stripes are the waveguide openings on the SiO_2 mask and the curved dark stripes with black edges are the etched trenches. The photo on the bottom is the cross section of three adjacent etched trenches on a witness sample under microscope. 88

Figure 5.2: The throughput of the s-bends with different distances Δ between the trench and the waveguides and different transition shifts δ at the joints which are defined in Fig. 5.1. The minimum bend radius in the s-bends is 1.5 mm. 90

Figure 5.3: Diagram of near-degenerate optical parametric generation using waveguides with one quasi-group-velocity-matching section, designed for a pump wave near 785 nm and signal and idler waves near 1570 nm. L_g is the length of each section of QPM gratings, L_{DC} is the length of each directional coupler and L_1 is the length of the straight waveguide between the two directional couplers. 91

Figure 5.4: (a) Auto-correlation traces and power spectra of the output from a device with four QGVM sections; (b) those from a conventional device without

QGVM. The solid curves correspond to a device temperature of 130 °C while the dotted curves correspond to a device temperature of 121.3 °C. The pump wavelength is 785.1 nm for all. The total length of QPM gratings is 24 mm in both cases. The pulse lengths and bandwidths in the figures are FWHM. 94

Figure 5.5: The power spectra of the output from a waveguide with one QGVM section. The total length of QPM gratings is 9.6 mm. The device temperature T is fixed at 130 °C in (a). The pump wavelength λ_p is fixed at 781.2 nm in (b). The baselines of the curves in (b) indicate the device temperature, which can be read from the vertical axis. All the traces are normalized to their maxima. The bandwidths shown in the figures are FWHM. 96

Figure 6.1: Typical device for OPG with two waveguide modes. 103

Figure 6.2: Illustration of the measurement of mode contrast out of a mode multiplexer by using a camera. (a) Mode shape recorded on a camera for an almost pure TM_{10} mode, which has two lobes. (b) Simulated cross section of the output mode (in the width dimension of the waveguide) when different power ratios (noted in the legend) between the TM_{00} and TM_{10} mode contents are considered. 104

Figure 6.3: Threshold measurement for OPG with the pump in the TM_{10} mode. 105

Figure 6.4: Power spectra of the OPG signal for the processes in the insets. The solid (dotted) curves show the signal emerging from the wide (narrow) arm of a mode demultiplexer. The idler near 1843 nm is not recorded. 106

Figure 6.5: Power spectra of the OPG signal from the two near-degenerate processes with the pump in the TM_{10} mode. The solid curve centered at 1332 nm shows the signal in the TM_{00} mode (with the idler centered at 1908 nm in the TM_{10} mode); the dotted curve centered at 1346 nm shows the signal in the TM_{10} mode (with the idler centered at 1880 nm in the TM_{00} mode). 107

Figure 6.6: Spectra of the OPG products near degeneracy with the pump in the TM_{10} mode. The solid (dotted) curve shows the output from the wide (narrow) arm of a mode demultiplexer. 108

Figure 6.7: Wavelength tuning curves for OPG in a 9.5-μm-wide waveguide. The curves are from simulations. The dashed curve corresponds to OPG involving only TM_{00} modes. The solid (dotted) curve corresponds to the OPG products in the TM_{00} (TM_{10}) mode with the pump wave in the TM_{10} mode. The symbols are from measurements and correspond to the three processes in the inset. 109

Figure 7.1: Diagram of a singly-resonant waveguide OPO on a lithium niobate chip. The main difference from Fig. 6.1 is that the idler is coupled back to form a loop by using two U-turn circular bends and one directional coupler. 114

CHAPTER 1: INTRODUCTION

Nonlinear optics has been an important application of lasers since their discovery in the 1960s and has become widespread with the recent advances in nonlinear optical materials and solid-state lasers. Of the many fields of nonlinear optics, optical parametric processes [1] are among the most widely used tools that can extend the available wavelength ranges of coherent radiation via frequency conversion. Optical parametric processes have indispensable applications in optical communication, spectroscopy and medical instruments.

Many optical parametric processes involve high intensities and rely on high single-pass gain. High intensities are achieved by either using tightly focused beams in bulk materials or using waveguides; the latter is much more efficient. High parametric gain is usually achieved in appropriate nonlinear materials such as periodically-poled lithium niobate (PPLN), which is one of the most efficient nonlinear materials for near- and mid-infrared optics. Combining the advantages of waveguides and PPLN, reverse-proton-exchange (RPE) lithium niobate waveguides have been one of the most efficient devices for optical parametric processes. [2] RPE lithium niobate waveguides are also very versatile because both the waveguide structures and the quasi-phase-matching (QPM) gratings fabricated by periodic poling can be tailored for specific purposes, including engineering the tuning curves of second-harmonic generation (SHG), [3, 4] separating different wavelength components on chip by mode demultiplexing, [5] and facilitating device integration by using various waveguide structures. [6, 7]

As is shown in this dissertation, engineering of the RPE lithium niobate waveguides can greatly improve the performance of high gain parametric processes including optical parametric amplification (OPA) and optical parametric generation (OPG). For optical parametric generation with 2-ps-long pump pulses near 780 nm we report a record low threshold of 200 pJ. The temporal properties of the OPG output pulses are improved by using engineered QPM gratings or using periodic waveguide structures composed of s-bends and directional couplers in a quasi-group-velocity-matching scheme. [8] We also demonstrate mode demultiplexing of the different frequency components from optical parametric amplification. With these improvements to the high gain parametric processes, RPE lithium niobate waveguides have the potential to become integrated tunable light sources or photon-pair sources [9, 10] and play a more important role in practical applications.

In this chapter we briefly discuss the principle of optical parametric processes, describe the basic theory of QPM gratings and RPE waveguides and their fabrication procedures, and give an overview of this dissertation.

1.1 Optical frequency conversion and parametric processes

Parametric nonlinear optics originates from the polarization response P induced by an optical frequency electrical field E, which may contain higher order terms of E:

$$P = \varepsilon_0(\chi^{(1)}E + \chi^{(2)}E^2 + ...) \tag{1.1}$$

Here $\chi^{(j)}$ is the jth-order susceptibility tensor. The linear term determines the linear propagation of optical waves while the higher order terms correspond to nonlinear effects under strong electrical fields.

In materials like KDP, BBO and lithium niobate the second-order term $\chi^{(2)}E^2$ can be significant under appropriate conditions. As a result optical waves at new frequencies will appear; this phenomenon is known as frequency conversion. Such a process is called a $\chi^{(2)}$ parametric process, [11] in which both photon energy and photon momentum are conserved because the state of the dielectric medium is the same before and after the process. The constraints on photon energy and momentum are illustrated in Fig. 1.1, using sum-frequency generation (SFG) as an example. Here ω_j (j = 1, 2, 3) is the angular frequency and k_j is the wave vector of the jth interacting wave. The constraint on photon momentum is often called the phase-matching condition. [12]

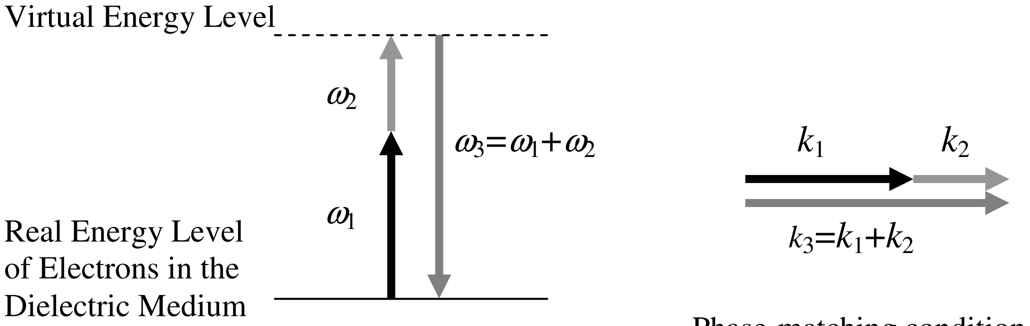
Virtual Energy Level
ω_2
$\omega_3=\omega_1+\omega_2$
ω_1
Real Energy Level of Electrons in the Dielectric Medium
k_1
k_2
$k_3=k_1+k_2$

Phase-matching condition

Manley-Rowe condition

Figure 1.1: Diagram of sum-frequency generation, a $\chi^{(2)}$ parametric process between three waves.

The simplest $\chi^{(2)}$ parametric process is second-harmonic generation, in which only two waves are involved and the constraints are simplified to $\omega_3 = 2\omega_1$, $k_3 = 2k_1$. Here the two subscripts 1 and 3 respectively denote the first-harmonic wave and the second-harmonic wave. Second-harmonic generation is widely used for generation of coherent radiation at short wavelengths in the visible or UV bands.

$\chi^{(2)}$ parametric processes involving three waves include sum-frequency generation, difference frequency generation (DFG) and optical parametric amplification, which are shown in Fig. 1.2. SFG and DFG are inverse processes of each other. Optical parametric amplification (OPA) and DFG are similar except for the much higher parametric gain in OPA. Interactions based on OPA include optical parametric generation and optical parametric oscillation (OPO). In optical parametric generation, vacuum noise is the input seed. OPO has an OPA in a resonant cavity. When the parametric gain is very low, the OPG process is often called parametric fluorescence.

Parametric processes can be more complex. We obtain a resonant parametric process by putting nonlinear crystals into a cavity, such as in OPO or resonant SHG. [13, 14] We obtain a cascaded $\chi^{(2)}$: $\chi^{(2)}$ process if the constraints for two $\chi^{(2)}$ parametric processes are simultaneously satisfied in the same device. [15-17] These processes add flexibility to frequency conversion and introduce new phenomena. Although we may have insights about them from the two conditions illustrated in Fig. 1.1, quantitative descriptions and device designs for these complex processes often require numerical simulations.

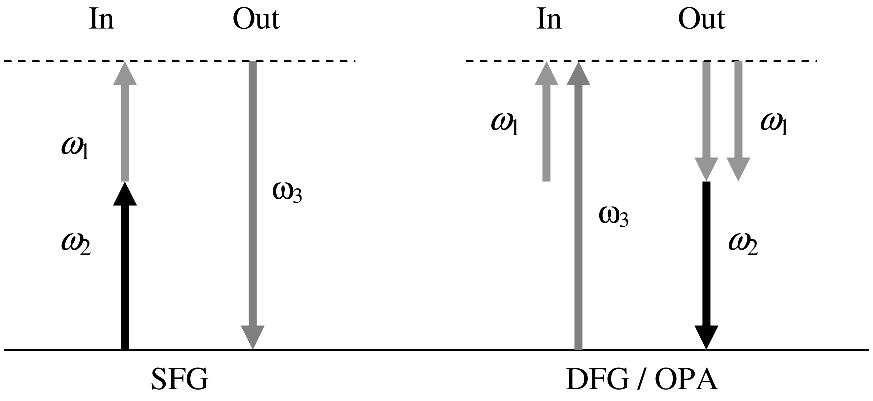

Figure 1.2: Diagrams of various $\chi^{(2)}$ parametric processes. The notation is the same as in Fig. 1.1.

This dissertation discusses high gain parametric processes including optical parametric amplification, optical parametric generation, and related cascaded processes. [15, 18, 19]

1.2 Quasi-phase-matching, periodic poling and synthesis of QPM gratings

Quasi-phase-matching was first proposed in theory in the early development of nonlinear optics. [12] Before parametric gains for quasi-phase-matching schemes were experimentally demonstrated as being comparable to other methods, [20-24] the phase-matching condition of parametric processes was often realized by temperature or angle tuning in birefringent crystals, which was often limited in applicability by available material properties.

The principle and effects of quasi-phase-matching on nonlinear frequency conversion are illustrated in Fig. 1.3. Figure 1.3(a) shows the phase-matching condition for a quasi-phase-matching scheme, where the wave vector associated with a periodic modulation of the properties of the nonlinear medium compensates for the wavevector mismatch of the interacting waves. Figure 1.3(b) shows the effect of quasi-phase-matching on second-harmonic generation using periodically reversed domains as an example. Instead of perfect phase-matching everywhere like in the phase-matched case, phase-mismatch is discretely compensated in QPM gratings.

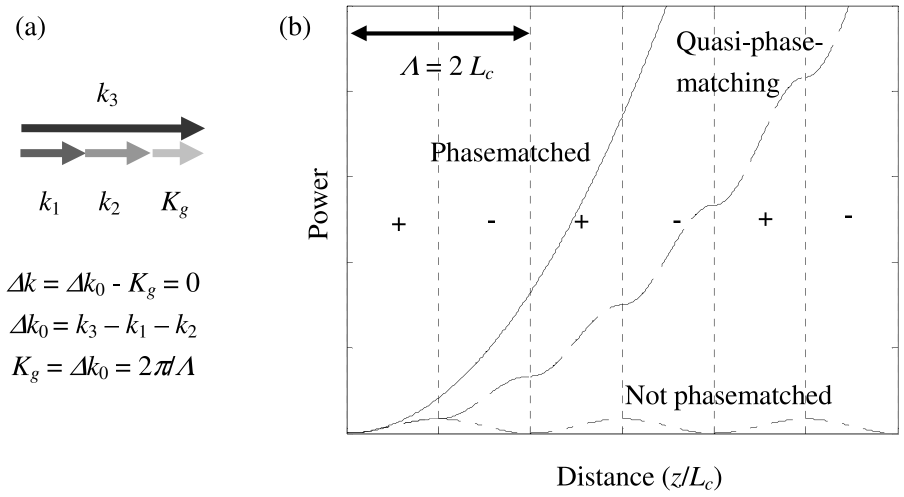

Figure 1.3: (a) The phase-matching condition in a quasi-phase-matching scheme; (b) The effects of quasi-phase-matching on second-harmonic generation. L_c is the width of the ferroelectric domains. Λ is the period of quasi-phase-matching.

Although quasi-phase-matching has lower conversion efficiency in SHG than perfect phase-matching, as shown in Fig. 1.3(b), brings useful flexibility into optical parametric processes. Among the advantages of QPM is that it allows the use of any convenient combination of polarizations in the nonlinear interaction, including the case where all waves are copolarized. Copolarized interactions have the largest nonlinear susceptibility in many materials and are necessary in cases when only optical waves of one polarization are supported in a waveguide, as is the case in reverse-proton-exchange waveguides fabricated on z-cut lithium niobate wafers. Quasi-phase-matching also enables parametric processes in isotropic crystals such as GaAs.

QPM structures are most commonly obtained by periodic poling of ferroelectric crystals like $LiNbO_3$, $LiTaO_3$, and KTP. The most widely used method for periodic poling makes use of electric fields, with the procedure shown in Fig. 1.4. [25] The principle is that the spontaneous polarization in a ferroelectric material such as lithium niobate can be reversed under the influence of a sufficiently large electric field. All the QPM devices involved in this thesis were fabricated in this way. A number of other techniques have been used to fabricate quasi-phasematched structures, including epitaxially-grown structures in semiconductors [26] and total-internal reflections in thin plates [27, 28].

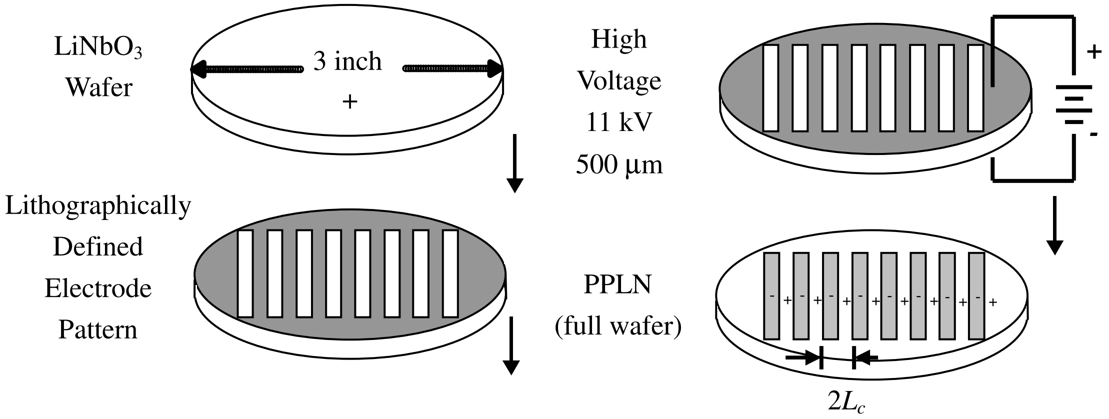
$LiNbO_3$ Wafer
3 inch
+
High Voltage 11 kV 500 µm
+
-
Lithographically Defined Electrode Pattern
PPLN (full wafer)
$2L_c$

Figure 1.4: Procedure of lithium niobate wafer poling with electrical fields.

The tuning behavior of QPM interactions depends on the Fourier transform of the QPM grating function. The periodic structure in a quasi-phase-matching scheme generally contains several discrete Fourier components which enable different orders of quasi-phase-matching. [29] For the simplest case shown in Fig. 1.5(a), a uniform QPM grating with a period of Λ, the Fourier transform of its grating function has a series of peaks, which are shown in Fig. 1.5(b). The peak at Λ/m is called the mth-order QPM peak and has an effective nonlinear coefficient of

$$d_{eff}^{m} = 2d_0 \sin(m\pi \times DC)/(m\pi) \tag{1.2}$$

where d_0 is the nonlinear coefficient of the bulk nonlinear crystal and DC is the domain duty cycle for the ferroelectric domains, defined as the ratio between the reversed domain width and the QPM period. As an example of higher order quasi-phase-matching the effects of first-order and third-order quasi-phase-matching on SHG are compared in Fig. 1.5(c).

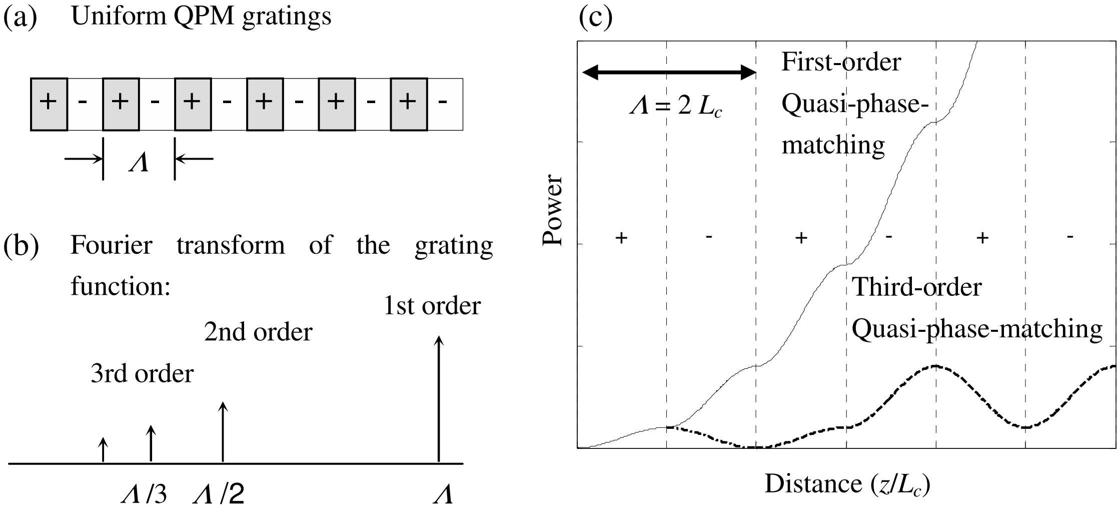
(a) Uniform QPM gratings
+
-
Λ
(b) Fourier transform of the grating function:
1st order
2nd order
3rd order
$\Lambda/3$
$\Lambda/2$
Λ
(c)
$\Lambda = 2\,L_c$
First-order Quasi-phase-matching
Third-order Quasi-phase-matching
Power
Distance (z/L_c)

Figure 1.5: (a) Diagram of uniform QPM gratings. (b) Demonstration of the QPM peaks for uniform gratings. The horizontal axis is the inverse of the spatial frequency. (c) Comparing effects of first-order and third-order quasi-phase-matching on second-harmonic generation. $L_c = \pi/\Delta k$ is the width of the ferroelectric domains. Λ is the QPM period.

In general the QPM gratings can be non-uniform and Fourier synthesis techniques can be applied conveniently to obtain desired tuning behavior. With such techniques, we can engineer the spectral amplitude and phases of the tuning curves of nonlinear interactions [3, 30, 31], fabricate tunable devices on a chip, [32, 33] increase nonlinear interaction length for short pulses, [34] practice nonlinear physical optics or create 2-dimensional nonlinear photonic crystals, [7, 35] and control cascaded parametric processes.[36]

Taking engineering of SHG tuning curves as an example, because the nonlinear conversion in QPM gratings can be conveniently described in terms of transfer functions in the frequency domain, [37, 38] we only need to synthesize QPM gratings with a grating function whose Fourier transform is the same as the scaled transfer function. Due to the limitations on the domain widths from electrical poling, we may need to optimize the grating domain designs under fabricability constraints to obtain the closest match to the transfer function. Various approaches had been tried to design QPM gratings satisfying strict or complex requirements and resulted in practical applications. [3, 4, 30, 31, 36]

1.3 Integrated high gain devices: reverse-proton-exchange lithium niobate waveguides and waveguide engineering

Waveguides have advantages over bulk materials for applications such as those in optical communications. [39] One advantage is device integration. Moreover, waveguides are more efficient than bulk devices in optical frequency conversion.

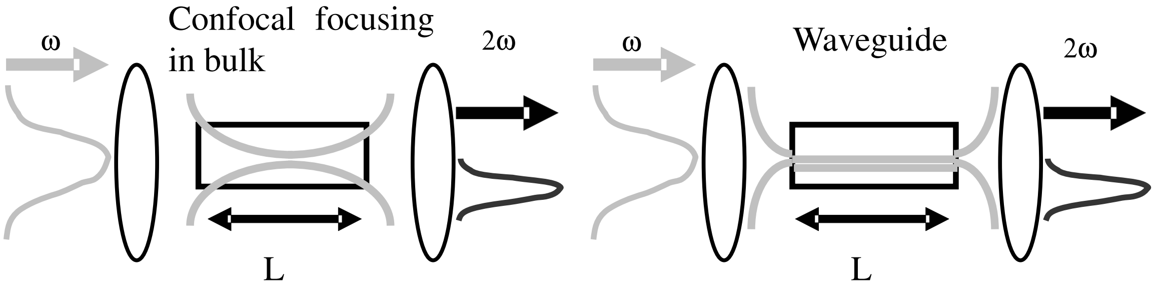

Figure 1.6: Comparison of beam propagation in bulk material (confocal focusing condition) and waveguides.

Figure 1.6 is a comparison between the beam propagation in bulk materials using confocal focusing and in waveguides. Although small beam size is obtainable in bulk materials by focusing tightly or creating solitons using nonlinear effects, [32, 40] the beam sizes in waveguides can be maintained over a longer distance than in bulk materials. Consequently the conversion efficiency for SHG is proportional to L^2 in waveguides instead of *L* in bulk materials using confocal focusing, [41, 42] meaning that waveguides are more efficient.

Another advantage of waveguides over bulk devices is that the waves involved in a parametric interaction in a waveguide interact as discrete entities. That is, power is added to or removed from the entire mode, so that there is no transverse variation in the conversion efficiency as generally occurs in interactions between Gaussian beams in bulk media. It is therefore easier to drive waveguide interactions towards depletion without deleterious effects like gain-induced diffraction or back conversion. [43, 44] Because the amplitude of the guided modes evolves only along the propagation direction, the mathematical description of interaction is one-dimensional (as in a plane-wave interaction), simulation of parametric processes in waveguide devices is simpler than that in bulk devices.

Several types of lithium niobate waveguides have been developed in the past 20 years, including Ti- or Ni-diffused waveguides, ridge waveguides and annealed- or reverse-proton-exchange waveguides. Reverse-proton-exchange waveguides are among the most efficient devices so far, with a normalized efficiency up to 150% /(W-cm^2) for SHG at 1.55 μm. [2] Ridge waveguides fabricated by liquid phase epitaxy or direct bonding [45, 46] have comparable efficiency but have higher propagation losses and are not appropriate for long devices that are desired for high-gain parametric processes. In contrast to ridge waveguides and Ti- or Ni- diffused waveguides which are able to guide both TM and TE modes, annealed- or reverse-proton-exchange waveguides fabricated on z-cut wafers only guide TM modes because the doping of protons lowers the refractive index for TE waves. Although TE modes are absent, TM modes in reverse-proton-exchange waveguides are well confined and thus enable high parametric gain.

The RPE process has been an important technique for the fabrication of low-loss optical waveguides in $LiNbO_3$ and is based on the annealed-proton-exchange (APE) process [47] which we will describe later. RPE buries proton-exchange lithium niobate waveguides and enhances the parametric gain by a factor of >2 over APE waveguides. [2, 48] An empirical model has recently been developed to accurately calculate the refractive-index profile in RPE waveguides based on the proton-exchange width and depth, and the annealing and reverse-proton-exchange times. [49]

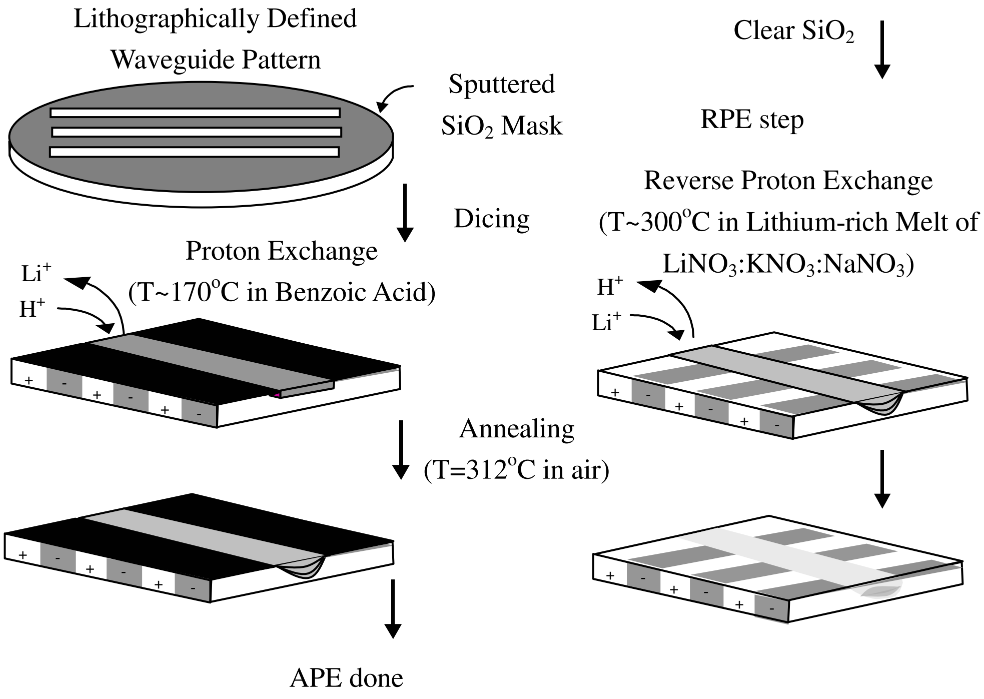
Lithographically Defined
Waveguide Pattern
Sputtered
SiO_2 Mask
Dicing
Proton Exchange
(T~170°C in Benzoic Acid)
Li^+
H^+
Annealing
(T=312°C in air)
APE done
Clear SiO_2
RPE step
Reverse Proton Exchange
(T~300°C in Lithium-rich Melt of
$LiNO_3$:KNO_3:$NaNO_3$)
H^+
Li^+

Figure 1.7: Fabrication procedure of RPE lithium niobate waveguides.

The fabrication procedure for RPE lithium niobate waveguides is illustrated in Fig. 1.7. Periodic poling as described in Fig. 1.4 is usually the first step before waveguides are fabricated. After that a ~50 nm-thick layer of SiO_2 is sputtered onto the $+z$ face of the poled congruent lithium niobate wafer. Then waveguides are patterned by contact lithography with a mask fabricated with a laser pattern generator. The exposed SiO_2 regions are etched with buffered oxide etchant (BOE, 1:6) forming a SiO_2 mask on the $+z$ face ready for proton-exchange. The width of the channels on this SiO_2 mask hereafter will be referred to as the waveguide width.

The–following steps are proton exchange, annealing, removing of the remnant SiO_2 layer in BOE and reverse proton exchange. As shown in Fig. 1.7, after waveguide patterns are ready wafers are diced and the chips obtained are put into benzoic acid for proton exchange, in which protons from the acid replace lithium ions in the patterned waveguide channels on the chips. When we use z-cut lithium niobate wafers, the proton-exchanged regions will have a higher refractive index for the TM modes and thus form waveguides. .

However such waveguides are not stable and the $\chi^{(2)}$ nonlinearity is lost in the proton-exchanged region. To solve these problems we anneal the chips at about 312 ^{o}C in a furnace. In this annealing procedure protons in the proton-exchanged waveguide channels are diffused deeper into the chips and form more stable waveguides. The $\chi^{(2)}$ nonlinearity is also restored after annealing. [47] The waveguides thus obtained are called annealed-proton-exchange waveguides.

The last step in the fabrication of RPE waveguides is reverse proton exchange, before which the SiO_2 mask must be removed to ensure uniformity in the following procedure. For reverse proton exchange the chips are put into a mixture melt at ~300 ^{o}C which is composed of $LiNO_3$, KNO_3 and $NaNO_3$ with an empirical mass ratio of. 30:52.2:17.8. [2, 48] Under such a condition part of the protons in the waveguides will be replaced by lithium ions in the melt, resulting in a more symmetric proton distribution in the depth dimension, increasing the mode overlap in parametric interactions and making a more efficient waveguide for frequency conversion. [2]

In a typical recipe for RPE waveguides designed for SHG of 1.55 μm waves, the proton-exchange time is ~24 hrs, the annealing time is ~23 hrs and the reverse-proton-exchange time is ~25 hrs. The fabrication times for proton exchange and RPE are affected by the temperature of the baths and the concentration of protons and lithium ions in the baths. However, we can adequately determine the fabrication time by monitoring the proton concentration in witness chips that are processed prior to the device chips. [49]

We have shown the waveguide fabrication procedure for separate chips in Fig. 1.7. Dicing is done before proton-exchange using dicing markers on the SiO_2 layer. To save device processing time we must fabricate RPE waveguides on a full wafer. [7] Different from in Fig. 1.7, dicing would be the last step. Proton exchange, annealing and reverse-proton-exchange are all done in full wafer. Because the layer of SiO_2 is gone in the dicing step, we add extra poling markers on the edges of the chips as dicing markers. After poling the –z face of the wafers must be etched in HF for >30 minutes to make these markers visible on wafer saws.

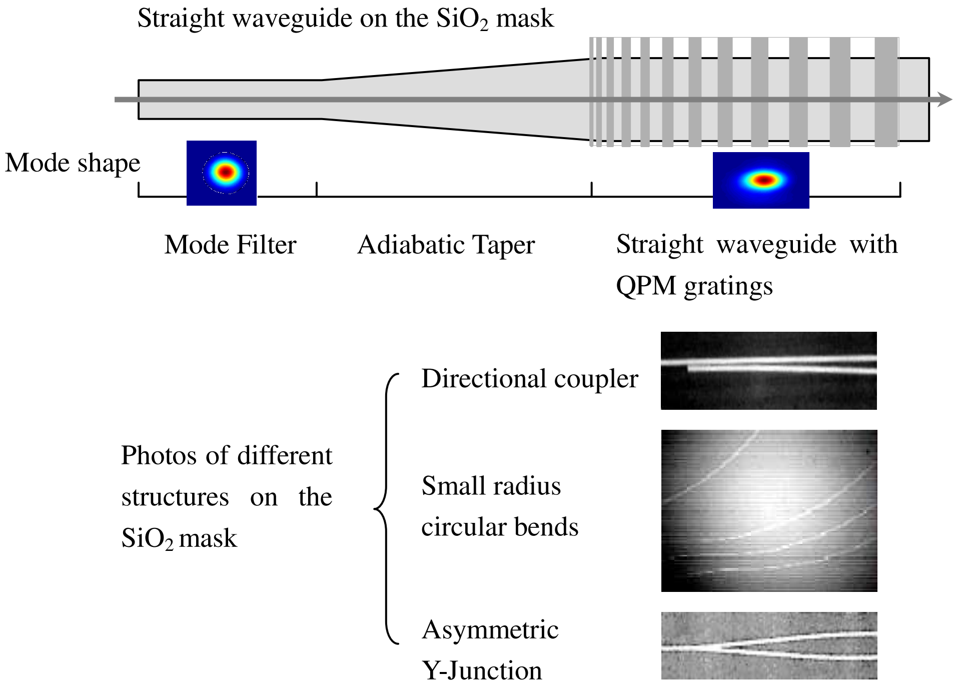
Straight waveguide on the SiO₂ mask
Mode shape
Mode Filter
Adiabatic Taper
Straight waveguide with QPM gratings
Photos of different structures on the SiO₂ mask
Directional coupler
Small radius circular bends
Asymmetric Y-Junction

Figure 1.8: Various structures on the SiO_2 mask for proton exchange.

We can engineer waveguide structures by varying the features on the mask for waveguide lithography. Figure 1.8 shows various structures developed for device integration on a lithium niobate chip, including straight structures (mode filters and tapers [50]) and structures with bends (directional couplers, circular bends [7], s-bends and Y-junctions [8, 51]). Combination of the different structures enables complicated tasks such as quasi-group-velocity-matching (QGVM). [8]

For devices with bends, we desire tight bends to accommodate more structures on the same device. The typical bend radius without introducing extra bend loss is 4 mm for APE or RPE waveguides fabricated with the conventional processes. [7, 8] This is small enough for many demonstration tasks but may be too large for optical circuits. In Section 5.1 we will discuss approaches to reduce this bend radius.

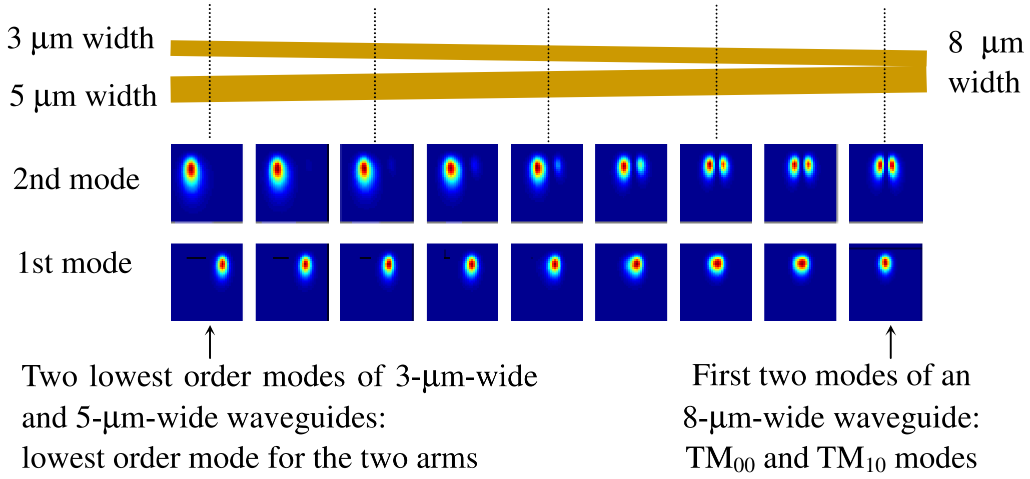
3 μm width
5 μm width
8 μm width
2nd mode
1st mode
Two lowest order modes of 3-μm-wide and 5-μm-wide waveguides: lowest order mode for the two arms
First two modes of an 8-μm-wide waveguide: TM$_{00}$ and TM$_{10}$ modes

Figure 1.9: Eigenmode profiles along an asymmetric Y-junction in RPE waveguides designed for 1550 nm waves.

Tapers are designed to connect waveguides of different widths; asymmetric Y-junctions are designed for mode multiplexing or demultiplexing. [50, 52] Although they are different in shape and function, for both of them we desire the optical waves to stay in the same waveguide mode as they propagate through the device. For good performance, tapers and asymmetric Y-junctions must change slowly enough that the modes evolve adiabatically. The detailed design method for such devices will be described in Section 2.6.3 using asymmetric Y-junctions as an example.

In both the APE and the RPE waveguides that we fabricated, adiabatic tapers successfully connected waveguides of different widths (such as 1.5 μm and 14 μm) and kept the waves in almost pure TM$_{00}$ modes. [50] Appropriately designed asymmetric Y-junctions in APE waveguides were very successful for mode multiplexing and mode-demultiplexing, and showed a mode separation contrast of > 30 dB for 1560 nm waves. [5]

Asymmetric Y-junctions in RPE waveguides also performed well. Figure 1.9 shows the eigenmode profiles for 1550-nm waves along an asymmetric Y-junction in RPE waveguides. For a 4-mm-long asymmetric Y-junction, if we launch a beam as the first (second) mode at the beginning, it will stay in the first (second) eigenmode along the whole device. In other words, if we launch the beam from the 3-μm-wide arm, the output would be in the TM_{10} mode as shown in Fig. 1.9; if we launch the beam from the 5-μm-wide arm, the output would be in the TM_{00} mode. The requirement for mode multiplexing is therefore fulfilled. If a beam propagates backwards, the asymmetric Y-junction serves as a mode demultiplexer. In Chapter 6 we use such a design for mode demultiplexing in optical parametric generation.

1.4 Parametric interaction of ultra-short pulses

Ultra-short pulses are involved in the high gain parametric processes in this thesis. The term “transform-limited” is often used when the temporal properties of the ultra-short pulses are concerned. A transform-limited optical pulse has unvarying instantaneous frequency in the time domain and equivalently has a flat spectral phase in the frequency domain; otherwise the pulse has chirp. The time-bandwidth product for a transform-limited pulse is ~0.4 for a well defined pulse shape such as Gaussian or hyperbolic secant. [38] We can use the time-bandwidth product to characterize the temporal property of a pulse and check if it is transform-limited.

Group velocity mismatch (GVM) plays an important role in frequency conversion of ultra-short pulses. The phenomena of parametric processes involving ultra-short pulses are much different from those involving CW waves because of GVM. An example is optical switching using a gated mixer, shown in Fig. 1.10.

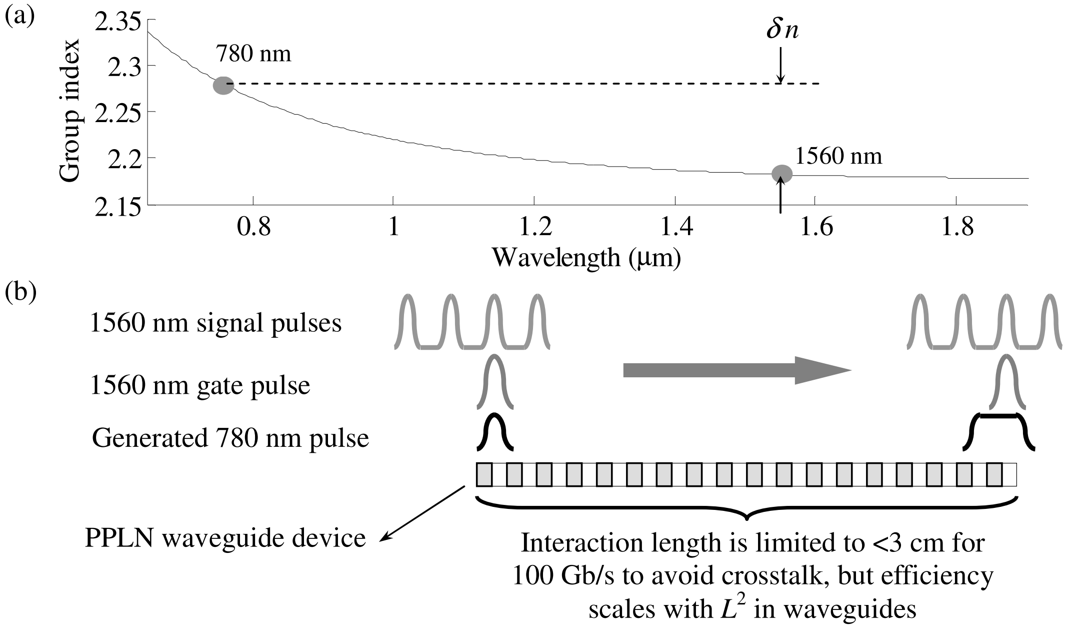

Figure 1.10: (a) Group index of the e-wave versus wavelength in z-cut lithium niobate wafers. δn is the difference between the group indices for 780 nm and 1560 nm waves. (b) Behavior of SHG in PPLN in the presence of GVM; illustrated using a gated mixer. The 780 nm pulse is the SHG of the 1560 nm gate pulse and its output pulse length is wider than the gate pulse due to group-velocity-mismatch.

We define the group-velocity-walkoff length as $c\tau/\delta n$ where c is the velocity of light in vacuum, τ is the pulse length and δn is the difference between the group indices for 780 nm and 1560 nm waves. SHG of the 1560 nm gate pulse is used to select a pulse from the 1560 nm signal pulse train for optical parametric mixing. Because the group index in lithium niobate is higher at 780 nm than at 1560 nm, the generated 780 nm pulse would be longer than the 1560 nm gate pulse and cause crosstalk if the nonlinear interaction length is longer than the group-velocity-walkoff length. The group velocity mismatch therefore demands a tradeoff between speed and the parametric gain.

Group velocity mismatch is also a key in optical parametric generation. Due to group velocity mismatch the parametric gain in OPG in long QPM gratings is much lower for ultra-short pump pulses than for CW pump. Moreover, the temporal properties of pulsed OPG are determined by the group velocity mismatches.

In the typical experiments involved in this thesis, the pulse length τ is 1.6 ps and the group-velocity-walkoff length between 780 and 1560 nm waves is ~5 mm. If the device length is much longer than 5 mm and the pump propagation loss is negligible, the output from OPG would be flat-top pulses whose length is proportional to the group velocity walkoff between the pump and the signal/idler. On the other hand the signal/idler bandwidth is inversely proportional to the group velocity walkoff between the signal and the idler (off degeneracy). The time-bandwidth-product of the signal/idler pulses therefore is proportional to the ratio between the group velocity walkoffs of the interacting waves and is inherently determined by the dispersion. This behavior will be discussed in detail in Chapter 2. In Chapter 4 and Chapter 5 we will discuss approaches to bypass this limitation. If not specifically noted, in this thesis we define the signal and the idler in OPA/OPG as the output at the shorter and the longer wavelengths, respectively.

In reverse-proton-exchange waveguides the material dispersion dominates over waveguide dispersion and the discussions above are still valid.

Besides GVM, higher order dispersion terms may become significant if the pulse length is < 100 fs. However in this dissertation the FWHM pump pulse length is between 1.6 ps and 2 ps. GVM therefore dominates and only the GVM and group-velocity-dispersion terms are considered in the analyses and simulations for this thesis.

1.5 Previously unsolved problems and overview of this dissertation

Optical parametric amplification and optical parametric generation had previously been studied in bulk lithium niobate and annealed-proton-exchange waveguides. [38] However the parametric gains were lower than in RPE waveguides, the output pulses from OPG in general were far from transform-limited and were not thoroughly studied, and the signal/idler generated in OPG and OPA were not separated on-chip. These issues are addressed in this dissertation by using engineerable QPM gratings and reverse-proton-exchange waveguides.

Chapter 2 reviews the theoretical descriptions of $\chi^{(2)}$ parametric processes in waveguides and lists important analytical and numerical results for OPA/OPG and related cascaded processes. Being essential for engineering of waveguide structures, coupled mode theory and bend theory are briefly discussed and used to analyze the waveguide structures including bends, directional couplers and asymmetric Y-junctions.

Chapter 3 demonstrates experiments of high gain optical parametric amplification with CW waves by the cascading of SHG and OPA and experiments of pulsed optical parametric generation showing a record-low threshold of 200 pJ/pulse for 2-ps-long pump pulses near 780 nm.

Chapter 4 discusses the improved temporal properties of the signal and idler from cascaded OPG which involves simultaneous quasi-phase-matching of two $\chi^{(2)}$ parametric processes using two different orders of QPM peaks. The temporal properties of the output from OPG are controllable by synthesizing QPM gratings to quasi-phase-match two parametric processes at desired signal (idler) wavelengths.

Chapter 5 demonstrates the application of quasi-group-velocity-matching in OPG. Quasi-group-velocity-matching improves the temporal properties of the output from OPG by arranging the apparent group velocities and the phases of the interacting waves. Approaches to fabricate tight bends are discussed in Section 5.1.

Chapter 6 reports two-mode optical parametric amplification and demonstrates mode demultiplexing for OPA using asymmetric Y-junctions. We describe experiments on shape optimization of asymmetric Y-junctions in Section 6.1.

Chapter 7 is a summary of this dissertation and discusses future directions and applications of high gain parametric processes using RPE waveguides.

CHAPTER 2: THEORY AND SIMULATIONS OF PARAMETRIC PROCESSES AND OPTICAL CIRCUIT COMPONENTS IN LITHIUM NIOBATE WAVEGUIDES

This chapter contains a theoretical description of $\chi^{(2)}$ parametric processes in lithium niobate waveguides and the theory for optical circuit components including bends, directional couplers and asymmetric Y-junctions.

Theoretical background for $\chi^{(2)}$ parametric processes is discussed in Sections 2.1 through 2.3. In Section 2.1 the coupled equations for OPA/OPG are derived and analytical results are listed for special cases. Section 2.2 discusses the mechanism of pulsed optical parametric generation and lists important numerical results obtained from solving the coupled nonlinear equations. The effects of group-velocity-mismatch on the temporal properties of the OPG output are discussed. Section 2.3 contains the theory for cascaded $\chi^{(2)}$:$\chi^{(2)}$ processes, including the cascading of SHG and OPA for CW pump waves and cascaded OPG involving simultaneous quasi-phase-matching of SFG and OPG. With waveguide structures, parametric processes can be integrated into optical circuits for better performance. One example is mode demultiplexing in OPA. Parametric processes involving different waveguide modes are described in Section 2.4. The coupled mode theory and the beam propagation method are briefly discussed in Section 2.5. Based on numerical simulations from these theories, in Section 2.6 we describe the design of bends, directional couplers and asymmetric Y-junctions in RPE waveguides.

2.1 Parametric processes in waveguides involving three waves

The optical frequency electric fields in waveguides can be expanded into a weighted sum of orthonormal modes. The electric field in a particular mode of a waveguide at frequency ω_j can be given as:

$$E_j(x,\ y,\ z,\ t)\ =\ \mathrm{Re}\{\gamma_j \tilde{E}_j(x,\ y) A_j(z,\ t)\ \exp[i(\omega_j t - k_j z)]\} \tag{2.1}$$

where $\tilde{E}_j(x,\ y)$ is a waveguide eigenmode in the waveguide cross section, k_j is the wave-vector, $A_j(z,\ t)$ is a slow-varying complex amplitude, and $\gamma_j = \sqrt{2/(n_j c\varepsilon_0)}$ is a normalization constant, where n_j is the refractive index at ω_j, c is the velocity of light in vacuum and ε_0 is the permittivity in vacuum. [7] Using this kind of expansion, the form of the coupled equations for parametric processes in waveguides are the same as those for plane waves, for cases where only one waveguide mode is involved at each interacting frequency. Hereafter we will make this assumption.

The optical frequency electric fields in dielectric media satisfy the following equation: [11]

$$\begin{aligned} &\partial^2 E(z,t)/\partial z^2 = \varepsilon_0 \mu_0 [\varepsilon(\omega)\partial^2 E(z,t)/\partial t^2 + \chi^{(2)} E^2(z,t)] \\ &\varepsilon(\omega) = c^2 k^2(\omega)/\omega^2 \end{aligned} \tag{2.2}$$

Supposing three waves with frequencies around ω_1, ω_2 and ω_3 ($\omega_3 = \omega_1 + \omega_2$) are involved in a $\chi^{(2)}$ parametric process, the electric field can be approximated as

$$E(z,t) = [\gamma_1 A_1(z,t) e^{i(\omega_1 t - k_1 z)} + \gamma_2 A_2(z,t) e^{i(\omega_2 t - k_2 z)} + \gamma_3 A_3(z,t) e^{i(\omega_3 t - k_3 z)}]/2 + c.c. \tag{2.3}$$

Here c.c is the complex conjugate of the other part in the expression, and $A_j(z,\ t)$ is the slowly-varying amplitude envelope of the jth field. For OPA and OPG, the wave near ω_3 is called the pump and the waves near ω_1 and ω_2 are called the signal and the idler, respectively. As long as the pulse length is much greater than one optical cycle, Eq. (2.2) can be written as three coupled equations with the slow varying envelope approximation (SVEA):

$$\begin{aligned}
&\partial A_1/\partial z + (1/u_1)\partial A_1/\partial t - i(\beta_1/2)\partial^2 A_1/\partial t^2 \\
&\qquad\qquad = -i\Gamma_1 A_2^* A_3 d(z)\exp(-i\Delta k z) - (\alpha_1/2)A_1 \\
&\partial A_2/\partial z + (1/u_2)\partial A_2/\partial t - i(\beta_2/2)\partial^2 A_2/\partial t^2 \\
&\qquad\qquad = -i\Gamma_2 A_1^* A_3 d(z)\exp(-i\Delta k z) - (\alpha_2/2)A_2 \\
&\partial A_3/\partial z + (1/u_3)\partial A_3/\partial t - i(\beta_3/2)\partial^2 A_3/\partial t^2 \\
&\qquad\qquad = -i\Gamma_3 A_1 A_2 d(z)\exp(i\Delta k z) - (\alpha_3/2)A_3
\end{aligned} \tag{2.4}$$

Only the group velocity mismatch and group velocity dispersion terms are included in Eq. (2.4) since higher order terms are negligible for all the processes considered in this dissertation. Here $u_j = 1/(\partial k_j/\partial \omega_j)$ is the group velocity, k_j is the wavevector, and $\beta_j = \partial^2 k_j/\partial \omega_j^2$ is the group velocity dispersion coefficient at ω_j with j = 1, 2 or 3. $d(z)$ is the normalized QPM grating function; for a uniform QPM grating $d(z) = 1$. $\Delta k = k_3 - k_1 - k_2 - K_g$ is the wave-vector-mismatch of the interacting waves in QPM grating, and $\Gamma_j = [(8\pi^2 d_0^2)/(n_1 n_2 n_3 c \varepsilon_0 \lambda_j^2 A_{eff})]^{1/2}$ is the parametric gain coefficient. n_1, n_2 and n_3 and α_1, α_2, and α_3 are the refractive indices and the power attenuation coefficients of the three waves involved in the $\chi^{(2)}$ process, λ_j is the vacuum wavelength, and d_0 is the nonlinear coefficient of the bulk nonlinear crystal. A_{eff} is the effective area for the nonlinear process in a waveguide: [39, 53]

$$A_{eff} = 1/\left|\int_{-\infty}^{\infty}\int_{-\infty}^{\infty} \bar{d}(x,y)\tilde{E}_1(x,y)\tilde{E}_2(x,y)\tilde{E}_3^*(x,y)\,dxdy\right|^2 \tag{2.5}$$

This area is the inverse square of the weighted mode overlap integral of the eigenmode functions for the three waves in the cross section of the waveguide. The weight function $\bar{d}(x,y)$ is the QPM grating function in the same cross section, which would be the same as $d(z)$ if the gratings are pependicular to the waveguides.

Near degeneracy, i.e. for $\omega_1 \approx \omega_2 \approx \omega_3/2$, $\Gamma_3^2/4$ is equal to η_{SHG}, the normalized nonlinear conversion efficiency for SHG, where:

$$\eta_{SHG} = P_{SH}/(P_{FH}^2 L^2) \tag{2.6}$$

In general the parametric gain coefficients Γ_j in Eq. (2.4) are functions of the center frequencies of the three waves; corrections are needed when the bandwidths of the interacting waves are comparable to the center frequencies, as has been observed in the case of QPM OPG in GaAs. [54] However, in this dissertation the approximation of Eq. (2.3) is valid since the largest bandwidth is much smaller than the center frequencies.

For convenience in simulation, we replace the electric field envelopes $A_j(z, t)$ with a variable $B_j(z, t) = A_j(z, t)/\ \omega_j^{1/2}$. The photon number density $N_j(z, t)$ is proportional to $B_j^2(z, t)$. The equations for $B_j(z, t)$ are

$$\begin{aligned}
&\partial B_1/\partial z + (1/u_1)\partial B_1/\partial t - i(\beta_1/2)\partial^2 B_1/\partial t^2 = -i\Gamma B_2^* B_3 d(z)\exp(-i\Delta kz)\\
&\partial B_2/\partial z + (1/u_2)\partial B_2/\partial t - i(\beta_2/2)\partial^2 B_2/\partial t^2 = -i\Gamma B_1^* B_3 d(z)\exp(-i\Delta kz)\\
&\partial B_3/\partial z + (1/u_3)\partial B_3/\partial t - i(\beta_3/2)\partial^2 B_3/\partial t^2 = -i\Gamma B_1 B_2 d(z)\exp(i\Delta kz)
\end{aligned} \tag{2.7}$$

Here $\Gamma = [(16\pi^3 d_0^2)/(n_j n_k n_l \varepsilon_0 \lambda_1 \lambda_2 \lambda_3 A_{eff})]^{1/2}$ is the adjusted parametric gain coefficient. We have neglected loss terms in Eq. (2.7). The propagation losses in RPE waveguides are as small as <0.15 dB/cm and do not significantly affect the qualitative properties of high gain parametric processes.

Eq. (2.7) can be further simplified for CW waves by neglecting the time-derivative terms on the left hand side. For OPA in uniform QPM gratings without pump depletion, we can further omit the last equation and obtain:

$$\begin{aligned}
&\partial B_1/\partial z = -i\Gamma B_2^* B_3 \exp(-i\Delta kz)\\
&\partial B_2/\partial z = -i\Gamma B_1^* B_3 \exp(-i\Delta kz)
\end{aligned} \tag{2.8}$$

For these equations we have analytical solutions for the signal and idler at the end of a straight waveguide with a QPM grating length of L:

$$\begin{aligned}
B_1(L) &= \exp[-i\Delta kL/2 + i\varphi_1(0)]\times \\
&\quad \{B_1(0)[\cosh(\Gamma''^{*} L) - i\Delta kL/(2\Gamma''^{*})\sinh(\Gamma''^{*} L)] \\
&\quad + B_2^{*}(0)(\Gamma'/\Gamma''^{*})\exp(i\Delta\varphi)\sinh(\Gamma''^{*} L)\} \\
B_2(L) &= \exp[-i\Delta kL/2 + i\varphi_2(0)]\times \\
&\quad \{B_1^{*}(0)(\Gamma'/\Gamma'')\exp(i\Delta\varphi)\sinh(\Gamma'' L) \\
&\quad + B_2(0)[\cosh(\Gamma'' L) - i\Delta kL/(2\Gamma'')\sinh(\Gamma'' L)]\}
\end{aligned} \tag{2.9}$$

Here $\Gamma' = \Gamma L B_3$, $\Gamma''^2 = \Gamma'^2 - (\Delta kL/2)^2$, $\varphi_j(0)$ is the initial phase of the *j*th wave and $\Delta\varphi = \varphi_3(0) - \varphi_1(0) - \varphi_2(0) - \pi/2$ is the initial phase difference. Assuming that the gain term Γ' is larger than the phase-mismatch term $\Delta kL/2$, the photon number densities from OPA are

$$\begin{aligned}
N_1(L) &= N_1(0)[\cosh^2(\Gamma'' L) + (\Delta kL/2\Gamma'')^2\sinh^2(\Gamma'' L)] \\
&\quad + N_2(0)(\Gamma'/\Gamma'')^2\sinh^2(\Gamma'' L) \\
&\quad + 2(\Gamma'/\Gamma'')[N_1(0)N_2(0)]^{1/2}\sinh(\Gamma'' L) \\
&\qquad [\cosh(\Gamma'' L)\cos\Delta\varphi + (\Delta kL/2\Gamma'')\sinh(\Gamma'' L)\sin\Delta\varphi] \\
N_2(L) &= N_2(0)[\cosh^2(\Gamma'' L) + (\Delta kL/2\Gamma'')^2\sinh^2(\Gamma'' L)] \\
&\quad + N_1(0)(\Gamma'/\Gamma'')^2\sinh^2(\Gamma'' L) \\
&\quad + 2(\Gamma'/\Gamma'')[N_1(0)N_2(0)]^{1/2}\sinh(\Gamma'' L) \\
&\qquad [\cosh(\Gamma'' L)\cos\Delta\varphi + (\Delta kL/2\Gamma'')\sinh(\Gamma'' L)\sin\Delta\varphi]
\end{aligned} \tag{2.10}$$

If $N_2(0) = 0$ the photon number densities at *L* are

$$\begin{aligned}
N_1(L) &= N_1(0)[\cosh^2(\Gamma'' L) + (\Delta kL/2\Gamma'')^2\sinh^2(\Gamma'' L)] \\
N_2(L) &= N_1(0)(\Gamma'/\Gamma'')^2\sinh^2(\Gamma'' L)
\end{aligned} \tag{2.11}$$

When the phase-matching condition is satisfied, i.e. $\Delta k = 0$, we have

$$\begin{aligned}
N_1(L) &= N_1(0)\cosh^2(\Gamma' L) \\
N_2(L) &= N_1(0)\sinh^2(\Gamma' L)
\end{aligned} \tag{2.12}$$

Under the high gain limit [38]

$$N_1(L) \approx N_2(L) \approx N_1(0)\exp(2\sqrt{\eta_{SHG}P}L)/2 \tag{2.13}$$

which can be used to estimate the threshold of OPG. The OPG threshold is conventionally defined as the pump pulse energy corresponding to a gain of 10^{10} or 100 dB. For a 1-ps-long pump pulse and a 1-cm-long QPM grating in RPE waveguides with η_{SHG} ~ 100%/(W-cm^2), the OPG threshold $E_{thr} = P\tau = \ln^2(10^{10})\tau/(4\eta_{SHG}L^2)$ is ~130 pJ. The practical OPG threshold for picosecond pulses would be higher than this rough estimation since the group velocity mismatch is neglected in deriving Eq. (2.13). More precise OPG threshold can be obtained from numerical methods which we will describe in Section 2.2.

As another special case, if $N_2(0) = N_1(0)$, $\Delta k = 0$ and the gain is high, for which we obtain

$$N_1(L) \sim N_2(L) \sim 4N_1(0)\cosh^2(\Gamma' L)\cos^2(\Delta\varphi/2) \tag{2.14}$$

In Section 5.3 we will use this result to explain the output spectra of OPG from quasi-group-velocity-matching devices.

2.2 Theory for pulsed OPG in waveguides

In SHG and OPO experiments using short pulses, appropriately adding chirps to the QPM gratings and pump pulses could result in a compressed output pulse. [55, 56] We may expect that such a technique will also work for OPG and improve the temporal properties of the output from pulsed OPG. However the situation is different in OPG because it is seeded with vacuum noise and different signal (idler) frequencies inherently have random phases, which cannot be removed by simply adding chirps. In this section we will describe the numerical simulation methods for waveguide OPG and discuss the temporal properties of pulsed OPG.

For an exponential process like OPG, the pulse length and bandwidth are mainly determined in the process before the pump is depleted. Therefore a good approximation is to solve the coupled nonlinear equations for OPG without pump depletion. Ignoring the third equation in Eq. (2.7) and neglecting the second order dispersion terms, the first two equations become

$$\begin{aligned}
&\partial B_1/\partial z+(1/u_1-1/u_3)\partial B_1/\partial\eta_3=-i\Gamma B_3(\eta_3)B_2^{*}d(z)\exp(-i\Delta kz)\\
&\partial B_2/\partial z+(1/u_2-1/u_3)\partial B_2/\partial\eta_3=-i\Gamma B_3(\eta_3)B_1^{*}d(z)\exp(-i\Delta kz)
\end{aligned}\tag{2.15}$$

where $\eta_3 = t - z/u_3$ is the shifted time variable centered on the peak of the pump pulse.

Suppose the signal input for OPG (random noises) is a sum of fields at a series of discrete frequencies ($\omega_1 + \Omega_n$, n = 1, 2, 3 …) with random phases φ_n while the idler input is zero:

$$\begin{aligned}
&B_1(0,t)=\sum_n B_{1n}(0)\exp(-i\Omega_n t-i\varphi_n)\\
&B_2(0,t)=0
\end{aligned}\tag{2.16}$$

We may directly use Eq. (2.16) as the initial fields. The properties of pulsed OPG can be derived by using many sets of $\{\varphi_n\}$ and averaging their different outputs.

Alternatively we use the following approach to study the OPG process more deterministically. Because Eq. (2.15) can be converted into a second-order partial differential equation for either B_1 or B_2, the output at z would be

$$\begin{aligned}
&B_1(z,t)=\sum_n B_{1n}(z,t)\exp(-i\varphi_n)\\
&B_2(z,t)=\sum_n B_{2n}(z,t)\exp(-i\varphi_n)
\end{aligned}\tag{2.17}$$

where $B_{1n}(z, t)$ and $B_{2n}(z, t)$ are independent of the random phases. We therefore may solve Eq (2.15) for a series of different Ω_n with initial fields $B_1(0,t) = B_{1n}(0)\exp(-i\Omega_n t)$ and $B_2(0,t) = 0$, and obtain $B_{1n}(z, t)$ and $B_{2n}(z, t)$.

In the time domain $<|B_j(z,t)|^2> = \sum_n |B_{jn}(z,t)|^2$; in the frequency domain $<|\tilde{B}_j(z,\Omega)|^2> = \sum_n |\tilde{B}_{jn}(z,\Omega)|^2$ (j = 1 or 2). We thereby are able to obtain the parametric gain and the temporal properties of the signal and the idler without explicitly including the random phases in the simulation.

Under special conditions the coupled equations in Eq. (2.15) have analytical solutions. If $B_2(0, t) = 0$ and $d(z) = 1$ (for a uniform QPM grating), Eq. (2.15) is comparable to the up-conversion problem in Ref. [57] and we can derive:

$$B_2(z,\eta_2) = -i\Gamma \int_0^z dy B_1^*(0,\eta_2 + \nu_{21} y) B_3(\eta_2 + \nu_{23} y) \bar{R} \exp(-i\Delta k y) \tag{2.18}$$

where $\eta_2 = t - z/u_2$, $\nu_{21} = 1/u_2 - 1/u_1$ and $\nu_{23} = 1/u_2 - 1/u_3$ are group velocity walkoffs, and $\bar{R}$ is the normalized Riemann function [58] which depends on the pump and the group velocity walkoffs.

When the pump is a continuous wave satisfying $B_3(0) = B_{30}$, the normalized Riemann function is

$$\bar{R} = iI_0(2\Gamma B_{30}\sqrt{y(z-y)}) \tag{2.19}$$

where I_0 is the modified bessel function of the second kind. When the pump is a hyperbolic secant pulse satisfying $B_3(0, \mathrm{t}) = B_{30}\,\mathrm{sech}(t/\tau_3)$, where τ_3 is the pulse length, the normalized Riemann function is a hypergeometric function: [57, 58]

$$\bar{R} = F^{*}(n, -n; 1, b)$$
$$n = i\Gamma B_{30}\tau_3 / \sqrt{\nu_{13}\nu_{23}}, \quad (2.20)$$
$$b = \sinh(y\nu_{13}/\tau_3)\sinh[(z-y)\nu_{23}/\tau_3]\operatorname{sech}(\eta_3/\tau_3)\sinh[(\eta_1 - \nu_{21}y)/\tau_3)$$

We can use these anaylytical solutions under special conditions to validate our numerical simulation codes. Solutions to Eq. (2.15) obtained by the Split-Step Fast-Fourier-Transform (FFT) method [59] match well with these analytical solutions.

For the rest of this section we will show that the temporal properties of OPA and OPG are mainly determined by the group velocity mismatches between the three interacting waves, as is also verified by numerical simulations. We only consider up to the second order dispersion terms.

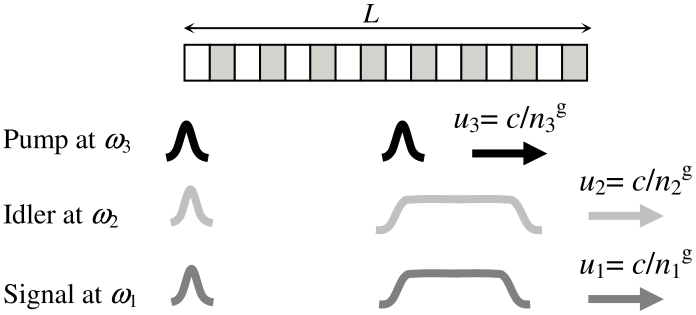

Figure 2.1: Typical diagram of the group velocity walkoffs in optical parametric amplification or optical parametric generation. n_j^g (j = 1, 2, 3) is the group index. L is the QPM grating length.

To understand the scaling behavior of the pulse lengths and bandwidths in OPG, consider the following qualitative arguments. Suppose the OPA input wavelength is ω_1 and both the QPM gratings and the pump pulse has no chirp. As shown in Fig. 2.1, for typical cases in PPLN the group velocity walkoff between the idler and the pump is much larger than that between the signal and the idler. The idler pulse length τ_2 therefore is proportional to $\nu_{32}L = L(1/u_3 - 1/u_2) = (n_3^g - n_2^g)L/c$ which is the group velocity walkoff. Similarly the signal pulse length τ_1 is proportional to $\nu_{31}L = L(1/u_3 - 1/u_1) = (n_3^g - n_1^g)$

L/c . For OPG, the input is vacuum noise and its bandwidth is wide. However, as long as group velocity dispersion is negligible in the signal (idler) band, the above estimates of pulse length are valid.

To obtain the bandwidth for the OPG output, we must consider the phase-matching conditions for various input signal (idler) frequency components. [60] The wave-vector mismatch for OPG in a uniform QPM grating is

$$\begin{aligned} \Delta k &= k_3 - k_1 - k_2 - K_g \\ &= \Delta\omega_3 \nu_{32} - \Delta\omega_1 \nu_{12} + \beta_3 \Delta\omega_3^2/2 - (\beta_1 + \beta_2)\Delta\omega_1^2/2 \end{aligned} \tag{2.21}$$

We have a constraint $\Delta k(\Delta\omega_1/2) \sim 2\sqrt{G \ln 2}$ [61] for the FWHM bandwidth of OPA/OPG with a fixed parametric gain $G=\Gamma L$. If the pump frequency is fixed, i.e. $\Delta\omega_3 = 0$, we can derive the OPG signal bandwidth $\Delta\omega_1$: [41, 62, 63]

$$\begin{aligned} &\Delta\omega_1 \propto 1/(\nu_{12}L) && \text{off degeneracy} \\ &\Delta\omega_1 \propto 1/\sqrt{(\beta_1 + \beta_2)L} && \text{near degeneracy} \end{aligned} \tag{2.22}$$

From Eq. (2.22), the signal bandwidth is inversely proportional to the group velocity mismatch between the signal and the idler ($\nu_{12}L$) for off-degeneracy conditions ($\omega_1 >> \omega_2$). For near-degeneracy conditions ($\omega_1 \approx \omega_2$) it is inversely proportional to the square root of the sum of the second order dispersion coefficients ($\beta_1 + \beta_2$). The same conclusion holds for the idler.

For the case of off-degenerate operation, the time-bandwidth products for the signal and the idler can be estimated from the above pulse lengths and bandwidths:

$$\begin{aligned} \tau_1 \Delta\omega_1 &\sim \nu_{31}/\nu_{21} = \delta n_{31}/\delta n_{21} \\ \tau_2 \Delta\omega_2 &\sim \nu_{32}/\nu_{21} = \delta n_{32}/\delta n_{21} \end{aligned} \tag{2.23}$$

which are proportional to the group velocity walkoff ratio of the three interacting waves, revealing the strong connection between the temporal properties of OPG and the group velocity mismatches. Here $\delta n_{31} = | n_3^g - n_1^g |$, $\delta n_{12} = | n_1^g - n_2^g |$ and n_j^g (j = 1, 2, 3) is the group index. Note that the behavior of the time-bandwidth can be qualitatively different for cases where the signal and idler group velocities lie on opposite sides of the pump group velocity [64], and is discussed in section 2.3.2.

By numerically solving Eq. (2.15) we confirmed that the time-bandwidth product of the signal/idler from OPG has a minimum determined by the ratios shown in Eq. (2.23). [15, 65] We further verified that the temporal properties of OPG products cannot be improved by simply adding chirps to the QPM gratings and the pump pulses like in the case of SHG or OPO. [37, 38, 66, 67]

The complete set of Eq. (2.7) is necessary for quantitative analyses such as calculating photon conversion efficiency of pulsed OPG in the limit of strong pump depletion, for which we can no longer obtain a solution in the form of Eq. (2.17). The random phases therefore must be incorporated in the input signal like in Eq. (2.16) and we must average the numerical results for many different sets of random phases to compare to experimental results. For these simulations we also need to estimate the amplitudes of the initial noise field in RPE waveguides. Using the approximation of one photon per mode [32, 61] we can estimate the noise power level at

$$P_{\text{noise}} \sim \hbar\omega\delta\nu = \frac{\hbar\omega c\delta\lambda}{\lambda^2} \tag{2.24}$$

Here $\delta\lambda$ is the noise bandwidth. For OPG in typical RPE waveguides with 1-cm-long QPM gratings, the vacuum noise power in the 10 nm gain bandwidth around 1560 nm is ~0.16 μW.

2.3 Theory for cascaded $\chi^{(2)}$: $\chi^{(2)}$ processes

Cascaded $\chi^{(2)}$: $\chi^{(2)}$ processes are more complex than single-step $\chi^{(2)}$ processes like SHG or OPA. Here we describe the theory for the cascading of SHG and OPA with CW waves [7, 17, 42] and the theory for cascaded OPG [15] with a pulsed pump. Both processes are in waveguides and only one waveguide mode is considered for each wave.

2.3.1 Theory for the cascading of SHG and OPA

Cascading of SHG and DFG/OPA is a preferred operation mode for optical frequency mixers used in optical communications because all the inputs are in the communication band.

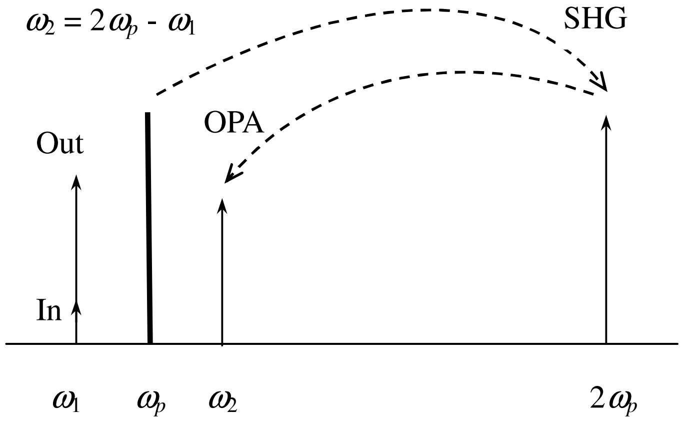

Figure 2.2: Diagram of the cascading of SHG and OPA.

We may directly use a 780-nm-band CW wave as the pump for a 1.5-μm-band OPA. However this scheme needs mode filters and directional couplers to combine the two input waves and also requires a high power CW pump laser in the 780-nm band, which is less convenient than a pump also in the communication band. Alternatively, we use the scheme shown in Fig. 2.2, where the pump for the 1550-nm band OPA is the SHG of a strong pump near 1550 nm. The pump and the signal are launched into the same fiber with a wavelength division multiplexing (WDM) coupler and then coupled into a RPE waveguide. In Section 3.1 we will demonstrate high parametric gain for OPA in RPE waveguides with this approach.

The cascading of SHG and OPA in uniform QPM gratings can be described with four coupled equations: [17]

$$\begin{aligned}
dA_p / dz &= -i\Gamma A_{SHG} A_p^{\ *} \exp(-i\Delta k_{SHG} z) - \alpha A_p \\
dA_{SHG} / dz &= -i\Gamma A_p^{\ 2} \exp(i\Delta k_{SHG} z) - 2i\Gamma A_1 A_2 \exp(i\Delta k_{OPA} z) - \alpha_{SHG} A_{SHG} \\
dA_1 / dz &= -i\Gamma A_{SHG} A_2^{\ *} \exp(-i\Delta k_{OPA} z) - \alpha A_1 \\
dA_2 / dz &= -i\Gamma A_{SHG} A_1^{\ *} \exp(-i\Delta k_{OPA} z) - \alpha A_2
\end{aligned} \tag{2.25}$$

Here A_j is the envelope of the optical-frequency electrical field. The subscripts 1, 2, p, SHG are for the input signal, the idler, the pump and the SHG of the pump, respectively. α is the propagation loss for the pump, the signal and the idler in the 1550-nm band; α_{SHG} is that for the SHG product in the 780-nm band. $\Delta k_{SHG} = k_{SHG} - 2k_p - K_g$ and $\Delta k_{OPA} = k_{SHG} - k_1 - k_2 - K_g$ are the mismatches in wave vectors for the SHG and OPA processes in uniform QPM gratings, respectively. The same gain parameter $\Gamma = [(8\pi^2 d_0^{\ 2})/(n_{SHG}\, n_p^{\ 2} c\varepsilon_0 \lambda_p^{\ 2} A_{eff})]^{1/2}$ can be used in all the equations because $\lambda_1 \sim \lambda_2 \sim \lambda_p = 2\lambda_{SHG}$ and the refractive indices of the three waves in the 1550-nm band are close to each other. The parameters involved in the calculation of Γ have the same definition as those in Eq. (2.4). We have $\eta_{SHG} = \Gamma^2, P_p = A_p^2$ from the definition of A_p. Here P_p is the pump power.

When phase matching conditions are satisfied for both the SHG and OPA processes, the depletion of the pump wave and the SHG product is negligible, and the losses satisfy $\alpha_{SHG} \sim 2\alpha$ (a good approximation for APE and RPE waveguides), we have analytical solutions to Eq. (2.25):

$$\begin{aligned}
A_p(z) &= A_p(0)\exp(-\alpha z) = A_p \exp(-\alpha z) \\
A_{SHG}(z) &= \Gamma A_p{}^2 z \exp(-2\alpha z) \\
A_1(z) &= A_1(0)\exp(-\alpha z)\cosh\{\Gamma^2 A_p{}^2[1-(1+2\alpha z)\exp(-2\alpha z)]/(4\alpha^2)\} \\
A_2(z) &= A_1(0)\exp(-\alpha z)\sinh\{\Gamma^2 A_p{}^2[1-(1+2\alpha z)\exp(-2\alpha z)]/(4\alpha^2)\}
\end{aligned} \tag{2.26}$$

If the losses are negligible, the conversion efficiency η from signal to idler in the low gain limit for the cascading of SHG and OPA is the same as that for the cascading of SHG and DFG: [16, 17]

$$\eta\ (\mathrm{dB}) \approx 10\log(\eta_{SHG}{}^2 P_p{}^2 L^4 / 4) \tag{2.27}$$

In the high gain limit, the parametric gain for the signal and the idler is

$$G\ (\mathrm{dB}) \approx 10\log[\exp(\eta_{SHG} P_p L^2)/4] \tag{2.28}$$

Real devices have much lower parametric gains than Eq. (2.28) due to propagation losses, pump depletion in SHG or OPA and parasitic processes through higher-order quasi-phase-matching. We can numerically solve Eq. (2.25) to fully consider the losses and pump depletion. In the absence of defects in the devices and the parasitic processes, the parametric gain monotonically increases with the length of the QPM gratings. We therefore fabricate waveguides with the longest possible QPM gratings for experiments of cascading SHG and OPA.

2.3.2 Theory for cascaded OPG

Cascaded OPG, in which the sum of the signal or idler wave with the pump wave is involved in the interaction, can improve the temporal properties of OPG with ultra-short pump pulses. [15] Figure 2.3 illustrates the situation for cascaded OPG involving sum-frequency generation between the signal and the pump. k_p, k_s, k_i and k_{SFG} are the wave-numbers of the pump, signal, idler and the sum-frequency waves. Δk^{OPG} (Δk^{SFG}) is the wave-vector mismatch in the OPG (SFG) process. We may engineer QPM gratings to simultaneously satisfy both phase-matching conditions.

(a) Photon energy conservation conditions

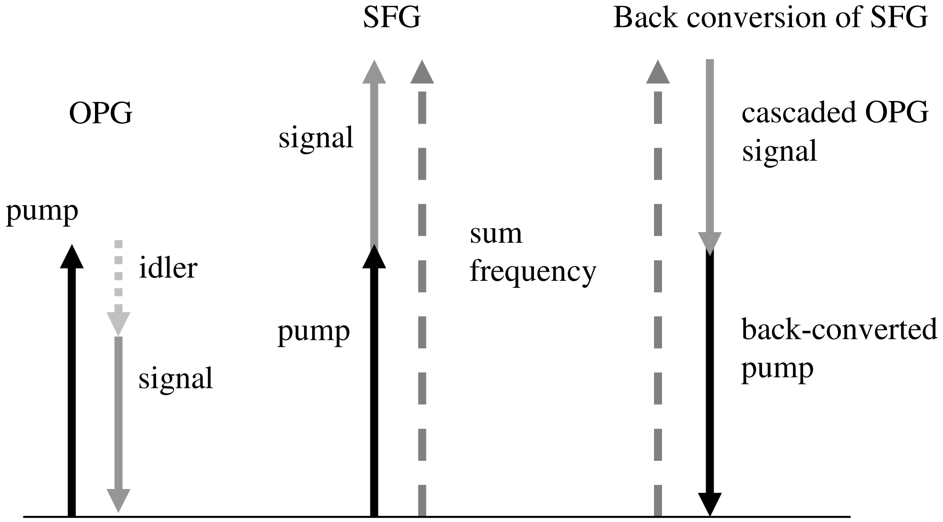
SFG
Back conversion of SFG
OPG
signal
cascaded OPG signal
pump
idler
sum frequency
pump
back-converted pump
signal

(b) Phase-matching conditions

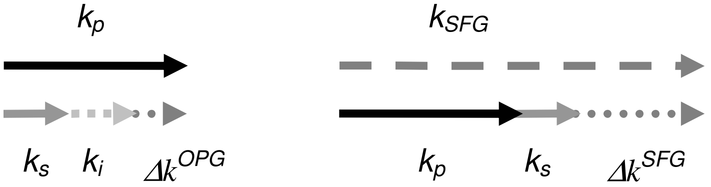
k_p
k_{SFG}
k_s
k_i
Δk^{OPG}
k_p
k_s
Δk^{SFG}

Figure 2.3: A diagram of the situation for cascaded OPG involving simultaneous quasi-phase-matching of optical parametric generation and sum-frequency generation between the pump and the signal.

Conventional OPG has been described in Eq. (2.4) while equations for cascaded OPG can be obtained by adding terms for the sum-frequency generation:

$$
\begin{aligned}
&\partial A_s / \partial z + (1/u_s)\partial A_s / \partial t = \\
&\qquad i\Gamma_{1s} A_i^* A_p d(z)\exp(-i\Delta k_1 z) + i\Gamma_{2s} A_p^* A_g d(z)\exp(-i\Delta k_2 z) \\
&\partial A_i / \partial z + (1/u_i)\partial A_i / \partial t = i\Gamma_{1i} A_s^* A_p d(z)\exp(-i\Delta k_1 z) \\
&\partial A_p / \partial z + (1/u_p)\partial A_p / \partial t = \\
&\qquad i\Gamma_{1p} A_s A_i d(z)\exp(i\Delta k_1 z) + i\Gamma_{2p} A_s^* A_g d(z)\exp(-i\Delta k_2 z) \\
&\partial A_g / \partial z + (1/u_g)\partial A_g / \partial t = i\Gamma_{2g} A_s A_p d(z)\exp(i\Delta k_2 z)
\end{aligned}
\qquad (2.29)
$$

Here we use the subscripts $j =$ s,i,p,g for signal, idler, pump and the sum-frequency wave. $\Gamma_{qj}= [(8\pi^2 d_0^2)/(n_j n_k n_l c\varepsilon_0\lambda_j^2 A_{eff}^q)]^{1/2}$ and A_{eff}^q are the parametric gain coefficient and the effective area for OPG (q = 1) and SFG (q = 2), and $\Delta k_1 = k_p - k_s - k_i - K_g^{OPG}$ and $\Delta k_2 = k_g - k_s - k_p - K_g^{SFG}$ are the wave-vector mismatches in the OPG and SFG processes, respectively. We assume that pulse durations and device lengths are such that group velocity dispersion can be neglected.

As we discussed in Section 2.2, it is difficult to find analytical solutions in general that could give insight into the dynamics of even the conventional OPG, so we carry out numerical simulations using a fast Fourier transform (FFT) split-step method to solve Eq. (2.29). [59] The simulation results show that the cascaded processes can lead to a variety of additional phenomena and may improve the temporal properties of OPG output.

Reviewing the properties of conventional OPG will help us understand the properties of cascaded OPG. For conventional OPG, numerical simulations gave results similar to Eq. (2.23). The time-bandwidth product of the signal has a minimum determined by the ratio between the group index differences $\delta n_{sp}/\delta n_{si}$. Here $\delta n_{sp} = | n_s^g - n_p^g |$, $\delta n_{si} = | n_s^g - n_i^g |$, and n_j^g is the group index.

Recall the discussion in section 1.4 that we can use the time-bandwidth product to check if a pulse is transform-limited; it is therefore possible to obtain transform-limited signal when $\delta n_{sp}/\delta n_{si} < 1$, especially if the group index of the pump is between those of the signal and the idler. [64, 68, 69]

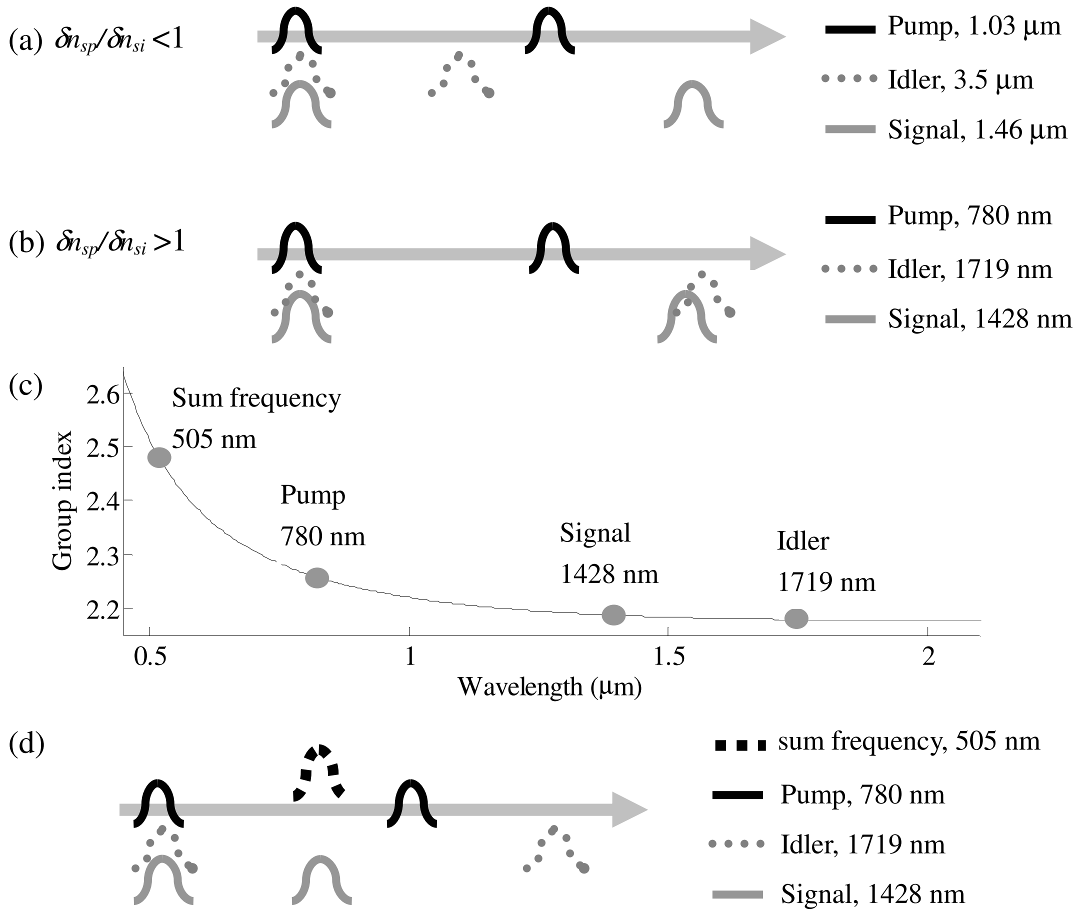

Figure 2.4: (a) Diagram of group velocity walkoff for pulsed OPG with the pump group index being between those of the signal and the idler. (b) Diagram of group velocity walkoff for pulsed OPG with the pump group index being higher than those of the signal and the idler. (c) Group indices for the four waves involved in a typical cascaded OPG process like that shown in Fig. 2.3. (d) Diagram of group velocity walkoff for cascaded OPG, showing that the effective group index of the signal is the same as that of the sum frequency and is higher than that of the pump. The nonlinear material is lithium niobate for all the figures here.

The diagram in Fig. 2.4(a) illustrates the group velocity walkoff in such a case. As a practical example, this condition holds in both $LiNbO_3$ and $LiTaO_3$ for a signal wavelength between 1.38 μm and 1.63 μm when the pump wavelength is 1.03 μm. [64]

Figure 2.4(b) illustrates the more common situation, where the group index of the pump is larger than those of the signal and the idler and $\delta n_{sp}/\delta n_{si} > 1$. In this case the minimum time-bandwidth product is approached at the high gain limit with a grating length of about 2.5 times the group-velocity-mismatch length between the signal and pump. Transform-limited output can not be easily obtained. In materials like BBO, transform limited output had been realized by collinear or noncollinear birefringent phase matching in bulk materials using the particular material properties (which is typically pumped with blue or green lasers). [70, 71] However, in proton-exchange lithium niobate waveguides all three waves are collinear and TM polarized and such configurations are not possible.

Alternatively we can use cascaded OPG to obtain transform-limited output because the extra wave involved may have higher group index than the pump so that the signal (idler) involved in the extra parametric process would have an effective group index higher than that of the pump.

This is illustrated in Fig. 2.4(c) and (d), where the sum frequency wave of the 780-nm pump and the 1430-nm signal is at 505 nm. As shown in Fig. 2.3, SFG and its back conversion co-exist in cascaded OPG. Signal photons generated in the back conversion of SFG interact somewhat as though they had the same group index as that of the sum frequency wave, which is higher than that of the pump. We thereby are able to alter the effective group velocity and control the temporal properties of the OPG products using cascaded OPG, bypassing the material limitations.

From the material dispersions and the above discussion we can predict the wavelength ranges that permit transform-limited output pulses for a selected cascaded OPG process. The extended range of transform-limited OPG output in bulk PPLN is shown in Fig. 2.5. Similar effects would also appear in RPE waveguides and other nonlinear materials.

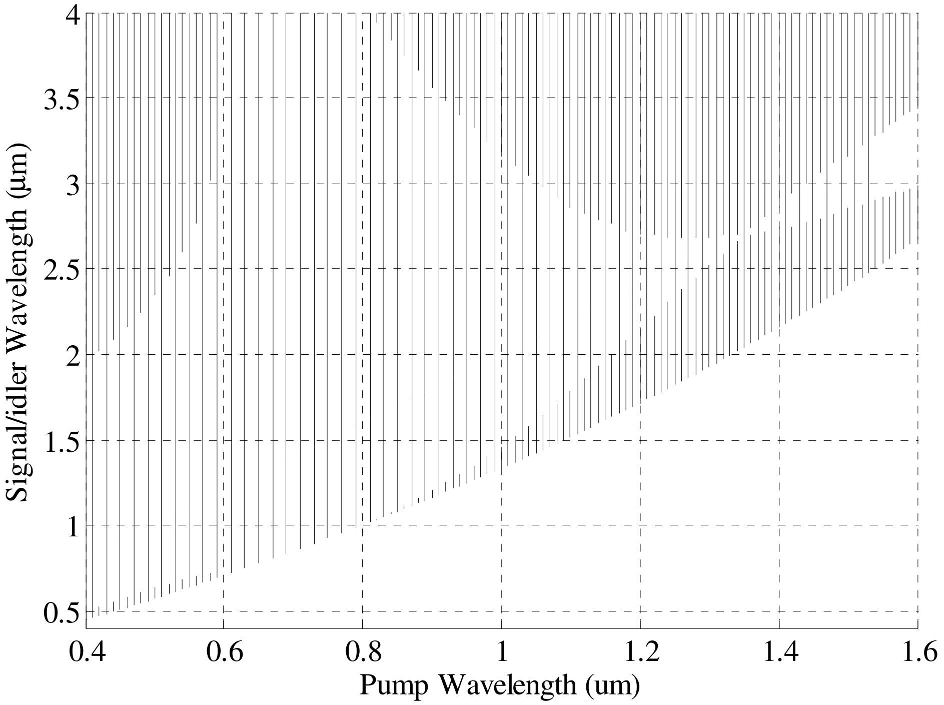

Figure 2.5: The transform-limited output ranges permitted by cascaded OPG (OPG and SFG between the pump and the signal/idler) in bulk PPLN, if we limit the idler wavelength to <4 μm. The double-line shaded region is for the conventional OPG and the single-line part is the extra region permitted by cascaded OPG.

2.4 Parametric processes involving different waveguide modes

The nonlinear efficiency of parametric processes in waveguides is inversely proportional to the effective area defined in Eq. (2.5):

$$\eta \propto 1/A_{eff} = \left| \int_{\infty}^{-\infty} \int \bar{d}(x,y)\, E_{1,jk}(x,y) E_{2,lm}(x,y)\, E_{3,np}^{*}(x,y)\, dx\, dy \right|^{2} \tag{2.30}$$

Here $\bar{d}(x,y)$ is the grating function in the cross section of the waveguide, which can be engineered by controlling the distribution of the reversed domains in the QPM gratings. [7, 51] $E_{1,jk}(x,y)$, $E_{2,lm}(x,y)$ and $E_{3,np}^{*}(x,y)$ are the normalized electric fields for the eigenmodes of the three interacting waves in the same cross section.

Eigenmodes can be obtained by solving the scalar eigenmode equation for a refractive index profile $n(x,y)$

$$(\partial^2/\partial x^2+\partial^2/\partial y^2)E(x,y)+[n(x,y)^2-n_{eff}{}^2]k_0{}^2E(x,y)=0 \tag{2.31}$$

Here k_0 is the vacuum wave-vector for the propagating wave and n_{eff} is the effective refractive index for the eigenmodes, and the refractive index profile $n(x,y)$ can be obtained from a diffusion model [47, 49] for RPE waveguides: [63].

RPE waveguides can be designed so that the quasi-phase-matching condition has no first-order dependence on the waveguide width, referred to as a non-critical design, which can greatly ease fabrication tolerances. [53] If we define the parity of a parametric process as the sum of the parity of the interacting waveguide modes in the width dimension, empirically only the "even" parametric processes have a noncritical waveguide width while the "odd" processes have a monotonically varying QPM period as a function of the waveguide width. An example of an "even" process is one in which the pump and the signal are in the TM_{10} mode and the idler is in the TM_{00} mode, which is used to demonstrate mode demultiplexing for OPG in Chapter 6. Such an "even" process requires regular QPM gratings that are relatively easier to fabricate than the tilted or staggered QPM gratings required for odd processes. [51] The theoretical noncritical waveguide width can be obtained by solving Eq. (2.31) for different waveguide widths, calculating the QPM periods for the desired parametric process and then finding the minimum in the curve of QPM period versus waveguide width.

To prepare different waveguide modes for parametric processes we need complex waveguide structures such as asymmetric Y-junctions. In the next section we will describe theories needed to design and optimize such waveguide structures.

2.5 Coupled mode theory and beam propagation method in waveguides

We may use either coupled mode theory or the beam propagation method (BPM) to simulate wave propagation in waveguides. [43, 44, 72, 73]

If the refractive index profile along the propagation dimension is slowly varying, the evolution of mode content along a waveguide can be treated with the local coupled-mode theory. [43, 44] The coupled mode equations for such a problem are:

$$\begin{aligned} \frac{dA_p(z)}{dz} &= \sum_{q\neq p} \kappa_{pq}(z) A_q(z) \exp\left[j\int_0^z \left(\beta_p(z)-\beta_q(z)\right)dz \right] \\ \kappa_{pq}(z) &= \frac{1}{2\sqrt{n_p(z)n_q(z)}[n_p(z)-n_q(z)]} \\ &\qquad \iint_{A_\infty} \frac{\partial n^2(x,y,z)}{\partial z} E_p^{\,*}(x,y,z) E_q(x,y,z)\,dxdy \end{aligned} \tag{2.32}$$

Here $\kappa_{pq}(z)$ is the coupling coefficient between the pth and qth modes, which is inversely proportional to the difference between the effective refractive indices of the two coupled local modes. $A_p(z)$, $n_p(z)$, $\beta_p(z)$ and $E_p(x, y, z)$ are the slowly varying amplitude, the effective refractive index, the propagation constant and the normalized modal electric field of the p-th order local normal mode. $n(x, y, z)$ is the refractive index profile.

Hereafter we normalize the z dimension to the device length L. Suppose only the coupling between the pth and qth modes is considered and a beam is launched at the start of the device in the qth mode.

In the low conversion limit, the power converted into the pth mode at the end of the device is

$$
\begin{aligned}
P_p &= \left| \int_0^1 [\kappa_{pq}(z)\exp(j\ \delta\beta(z) L\ z)] dz \right|^2 \\
\delta\beta(z) &= \frac{1}{z}\int_0^z (\beta_p(z') - \beta_q(z'))dz' = \frac{2\pi}{z\lambda}\int_0^z (n_p(z') - n_q(z'))dz' \\
&= \frac{2\pi}{z\lambda}\int_0^z \Delta n_{pq}(z')dz'
\end{aligned}
\tag{2.33}
$$

Here λ is the wavelength of the beam and $\delta\beta(z)$ is the average difference between the propagation constants of the pth and qth local eigenmodes from 0 to z. For the devices considered here, typically $\delta\beta(z)$ monotonically decreases only by a factor of ~2 from the beginning to the end of the device. The power conversion as a function of the device length L therefore is determined by the amplitude of the Fourier transform of the coupling coefficient $\kappa_{pq}(z)$ at spatial frequencies close to the average value of $\delta\beta(z)L$ over the length of the device. A larger $\delta\beta(z)L$ results in less power conversion due to more cancellations in the integration. To minimize coupling between two target modes we therefore prefer a longer device length L and a larger index difference $\Delta n_{pq}(z)$. Alternatively we may choose appropriate shapes for the devices to lower the coupling for a fixed length; in Section 2.6.3 we will discuss the shape optimization of asymmetric Y-junctions using the coupled mode theory.

Although the coupled mode theory is more appropriate for devices such as Y-junctions [52] and multimode interference devices [74], the beam propagation method is preferable if visualization of the mode conversion along the propagation is desired or nonlinear interactions are considered. With the slowly-varying-envelope approximation and paraxial wave approximation the wave equation for a weakly guided waveguide is:

$$
\begin{aligned}
&2ik_0\bar{n}\partial u / \partial z = (\partial^2/\partial x^2 + \partial^2/\partial y^2)u + [n(x,y,z)^2 - \bar{n}^2]k_0{}^2 u \\
&u = u(x,y,z)
\end{aligned}
\tag{2.34}
$$

Here $E(x, y, z) = u(x, y, z)\exp[i(\omega t - \bar{n}k_0 z)]$ is the scalar electric field, $n(x, y, z)$ is the index profile, k_0 is the vacuum wave-vector and $\bar{n}$ is a reference refractive index. Once the refractive index profile is known and the input field is given, the scalar electrical field along the device can be obtained using the BPM. If nonlinear processes are considered in BPM, the BPM equations will be similar to the nonlinear equations for parametric processes like Eq. (2.4). The difference is that two transverse spatial dimensions are involved in BPM instead of the one time dimension is involved in Eq. (2.4). The Split-Step-FFT method [59] therefore can also be used to solve the BPM equations.

In the next section we discuss the design of various waveguide components by considering the coupled mode theory or using the beam propagation method.

2.6 Waveguide components for optical circuits: bends, directional couplers and asymmetric Y-junctions

Basic components for optical circuits in RPE waveguides are shown in Fig. 1.8 and are used for various purposes in this dissertation. The quasi-group-velocity-matching structure in Chapter 5 is composed of directional couplers and s-bends, and the two-mode OPA devices in Chapter 6 depend on asymmetric Y-junctions for mode demultiplexing. In this section we will describe the theory and design of bends, directional couplers and asymmetric Y-junctions in RPE waveguides.

2.6.1 Bends

There are two types of bends in waveguides: a circular bend and an s-bend. The former has a constant curvature over the whole length while the latter has a varying curvature along its length. If the minimum bend radii are the same, it is often difficult to fabricate a circular bend with a loss comparable to an s-bend. For the applications in this thesis we use cosine-type s-bends with a shape function:

$$y = (A/2)\{1 + \cos[\pi(1 + x/L)]\} \tag{2.35}$$

where x, y are the length and height dimensions respectively, A is the height and L is the length. For RPE waveguides, this shape function is the center line of the waveguides defined on the SiO_2 mask for proton exchange.

Tight bends with small radii are desired in optical circuits for denser integration. The limiting factor is the increasing loss with smaller bend radii. Propagation loss in bends includes radiation loss coming from mode coupling into radiation modes, transition loss coming from the mode mismatch at the junction of curvature discontinuity and scattering loss coming from the roughness or defects in the waveguide structure. The scattering loss is the same in bends as in straight waveguides and is often negligible in RPE waveguides. Therefore we can obtain tighter bends only by reducing radiation loss and transition loss.

The minimum bend radius without significant radiation loss and the waveguide shift required to compensate for the transition loss can be obtained by using BPM [75, 76] or solving Eq. (2.31) with the effective index method using absorbing boundary conditions. [77, 78]

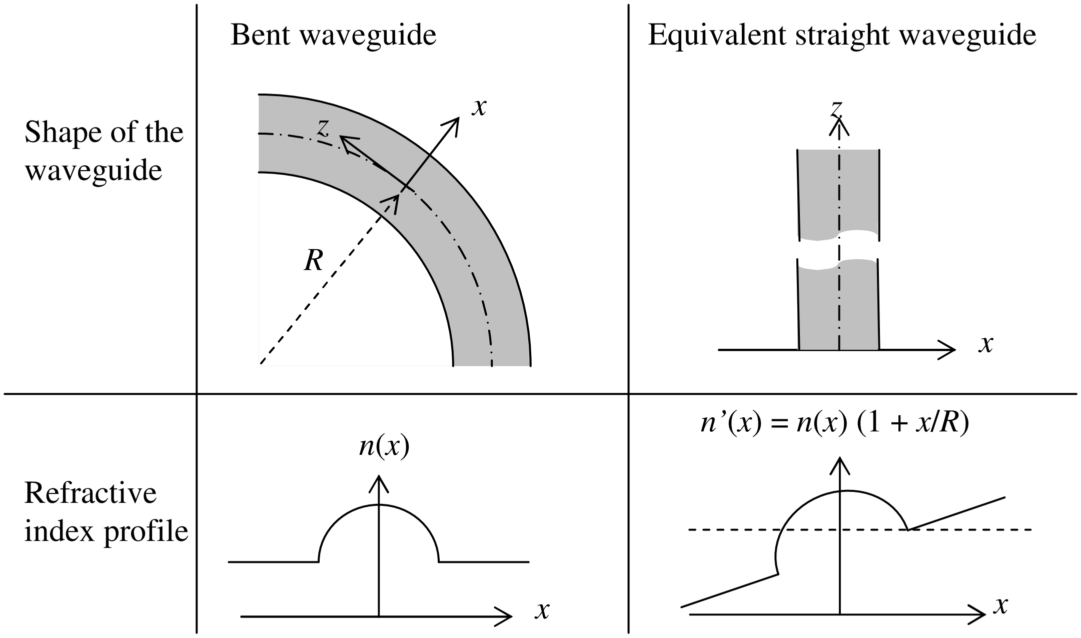

Figure 2.6: The effective index method. Bends are treated as equivalent straight waveguides.

The effective index method is illustrated in Fig. 2.6, in which a bent waveguide is treated as an equivalent straight waveguide with an adjusted index profile. This approximation is valid when the bend radius is much larger than the mode size in the waveguide. Estimated by this method, the smallest bend radius without significant radiation loss for a desired waveguide mode is approximately [79]

$$R_{min} \sim \rho\, n_{max}/(n_{eff} - n_0) \tag{2.36}$$

where n_{eff} is the effective index of the desired eigenmode in a straight waveguide, ρ is the mode size, and n_{max} and n_0 are respectively the maximum and minimum refractive index in the waveguide. We will use this formula in Section 5.1.1.

Because the major difference between the eigenmodes of a tight bend and those of a straight waveguide is a shift of the mode center, we may minimize the transition loss by shifting the relative center position of the waveguides at the joints of different curvatures. Mode coupling can be maximized with an approximate shift of $(\pi^2 n_{eff}^2 \rho^4)/(\lambda^2 R)$ in the correct direction, [76] where n_{eff}, ρ, λ, and R are the effective mode index, the mode size, the wavelength in vacuum and the radius of curvature, respectively. Examples will be discussed in Section 5.1.2.

2.6.2 Directional couplers

Directional couplers are composed of two nearby waveguides that often have the same index profiles. Based on the coupled mode theory the power transfer rate in a directional coupler is: [44, 80]

$$P(z) = P_0 \sin^2[\pi L/(2L_{DC})] \tag{2.37}$$

Here L_{DC} is the coupling length for complete power transfer, which can be estimated from $L_{DC} \sim (\lambda/2)/\,(n_1 - n_2)$, where n_1 and n_2 are the effective refractive indices for the two lowest-order eigenmodes in the cross-section of the directional coupler. Although we can solve Eq. (2.31) to obtain the eigenmodes for a directional coupler and estimate the coupling length, our current waveguide model may have >20% error in such an estimation. In practice we empirically determine the length of a directional coupler for a chosen spacing between the two arms.

2.6.3 Design and shape optimization of asymmetric Y-junctions

Based on the discussion in Section 2.5, a higher mode contrast for mode multiplexing using asymmetric Y-junctions generally requires a more adiabatic device. The result is a smaller branching angle and a longer device, which limits the integration capability. Here we describe how to shorten the length of asymmetric Y-junctions in diffused waveguides such as RPE lithium niobate waveguides while maintaining a high mode contrast in mode multiplexing. In the approach, we engineer the local mode coupling coefficients by modifying the shape of the Y-junctions on waveguide masks.

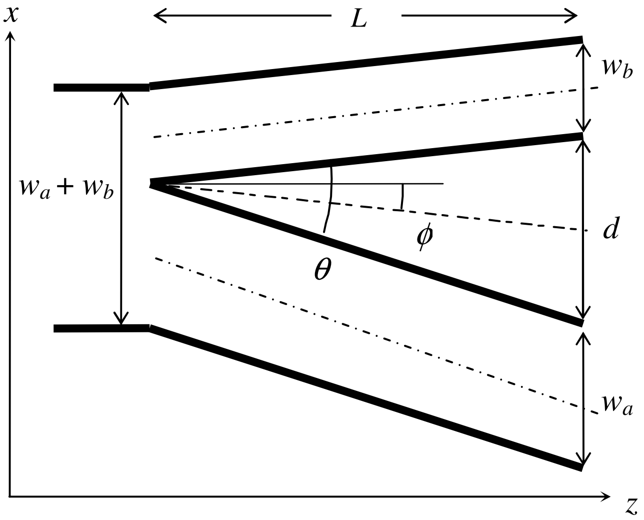

Figure 2.7: The mask design of an adiabatic asymmetric Y-junction. The maximum separation d between the two arms is much smaller than the Y-junction length L.

For the asymmetric Y-junction mask design in Fig. 2.7 θ and ϕ are the branching and tilt angle, respectively. The waveguide widths w_a and w_b are constant along the two arms.

In more complex designs these parameters are functions of z. To simplify the description, hereafter we normalize the z dimension to the device length L.

Suppose a beam is launched at the start of the device in the qth mode and only the coupling between the pth and qth modes is considered. According to the discussion in Section 2.5, to minimize the power conversion we usually prefer a longer device and a larger index difference $\Delta n_{pq}(z)$. If we want to reach the design target with relatively shorter devices the only way is to choose appropriate shapes for the asymmetric Y-junctions. To focus on the effects of the device shape we adhere to the optimal waveguide widths that are obtained by considering the coupled mode theory.

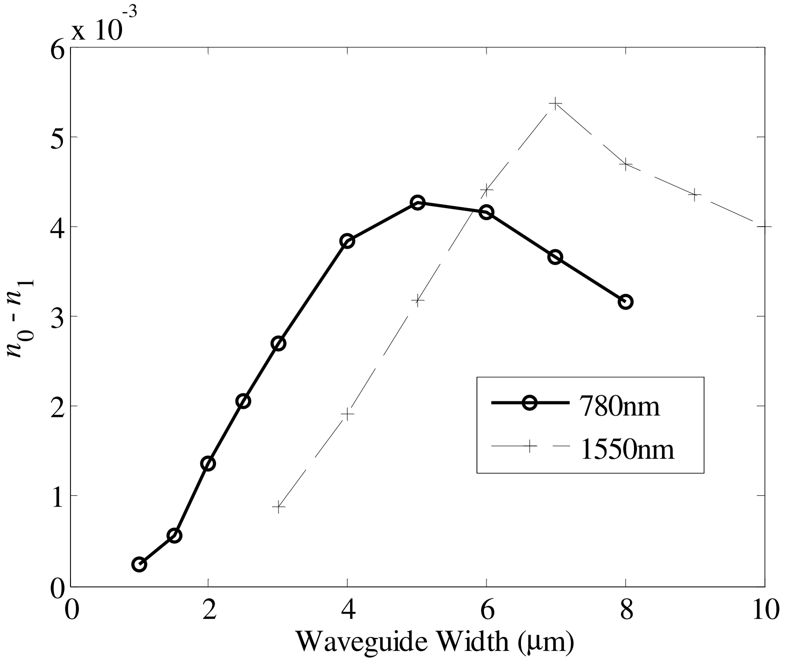

Figure 2.8: The simulated refractive index difference between the first and second eigenmodes in typical RPE waveguides. n_0 and n_1 are the effective refractive indices for the first two modes. The solid and dashed curves are for 780 nm and 1550 nm waves respectively.

The waveguide width at the start of the device in Fig. 2.7 ($w = w_a + w_b$) is chosen to maximize the index difference between the first two eigenmodes there. The optimal values of w correspond to the non-critical maxima of the curves in Fig. 2.8, which in theory are 7 μm for 1550 nm waves and 5 μm for 780 nm waves in RPE waveguides.

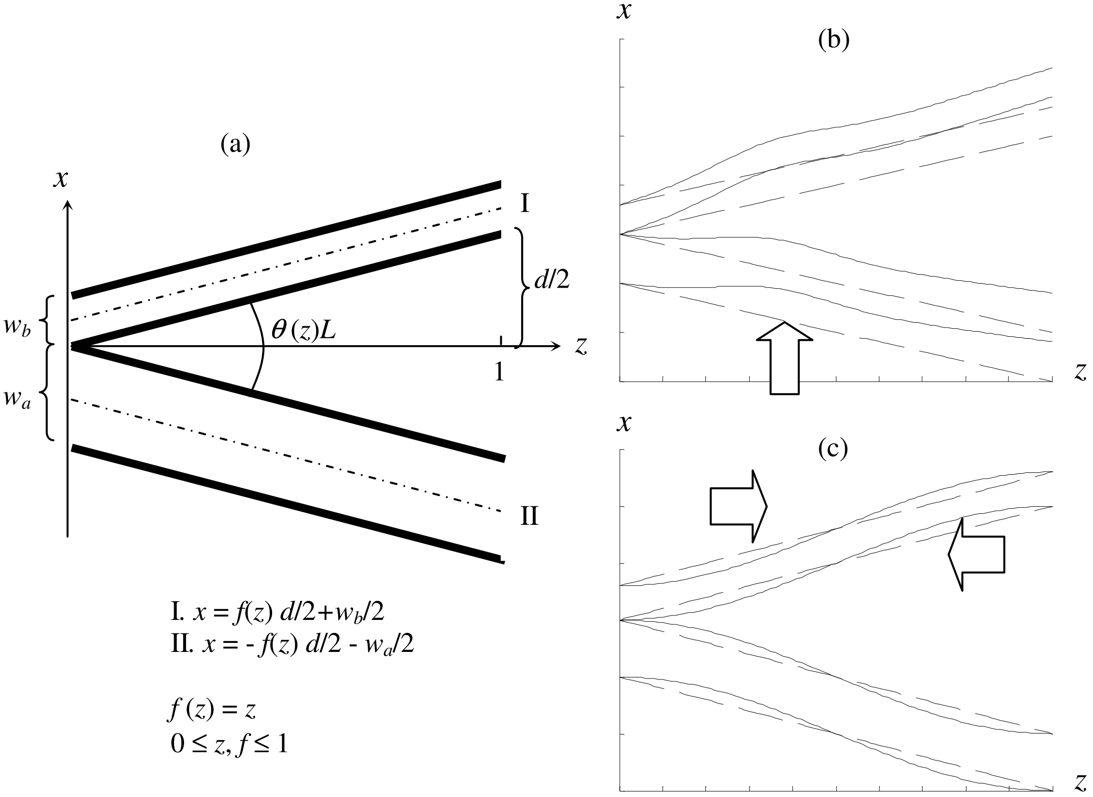

Figure 2.9: (a) The shape of our conventional asymmetric Y-junctions. I and II are the center traces of the two arms. (b) Varying the device shape by the “shifting” approach. (c) Varying the device shape by the “stretching” approach. The dashed curves in (b) and (c) are the conventional designs.

The two arms near the end of the Y-junction in Fig. 2.7 are far apart. If we launch a beam backwards from this end of the Y-junction, the first order mode of each arm should adiabatically evolve into one of the first two modes in the coupled region of the Y-junction, as we showed in Fig. 1.9. The key design parameter is $\delta w = |w_a - w_b|$, the width difference between the two arms, which should be a balance of two constraints: be large to ensure a high index difference between the two arms and be small enough to avoid making the second mode of the wider arm relevant. Once w is fixed we have limited choices for w_a and w_b, which can be experimentally checked. We fix the waveguide widths along the two arms as the optimal set of (w_a, w_b) to keep the best balance between the two constraints for δw.

For the shape optimization we start from our conventional design shown in Fig. 2.9(a) in which $\phi = 0$. The center trace of both arms can be described with the same function $f(z) = z$ and each arm has a constant local slope of $\theta(z)L/2 = d/2[\mathrm{d}f(z)/\mathrm{d}z] = d/2$. The coupling coefficient between the pth and qth modes is $\kappa_{pq}(z)$ and the power conversion from the qth mode into the pth mode at the end of the device is given by Eq. (2.33) in the low conversion limit.

To minimize the mode coupling in devices with a fixed length, it is reasonable to keep the inner edge-edge separation between the two arms monotonically increasing from 0 to the maximum. The shape variations should be adiabatic to avoid extra loss. Under these constraints the shape variation can be decomposed into two independent components.

The first one called the “shifting” approach is shown in Fig. 2.9(b). The two arms are shifted together in the x dimension with an amplitude $s(z)$ while the inner edge-edge separation is not affected. As a result, the center of the two arms become $x = f(z)\ d/2 + w_b/2 + s(z)$ and $x = -f(z)\ d/2 - w_a/2 + s(z)$ where $f(z) = z$. The local tilt angle becomes $\phi(z) = \mathrm{d}s(z)/\mathrm{d}z$ while the branching angle $\theta(z)$ is still constant.

The second one called the “stretching” approach is shown in Fig. 2.9(c). With the start and end fixed, the two arms are stretched or compressed together in the z-dimension so that $\phi(z) = 0$ while $\theta(z) = d/L\ [\mathrm{d}f(z)/\mathrm{d}z]$ is varying along z. In this approach $f(0) = 0$ and $f(1) = 1$ but $f(z)$ can vary nonlinearly with z.

For these designs we can deduce the coupling coefficients and the power conversion formula from the known results for the conventional design in Fig. 2.9(a).

In the "shifting" approach the formulae become

$$P_p = \left| \int_0^1 [\kappa^s_{pq}(z) \exp(j\ \delta\beta(z) L\ z)] dz \right|^2$$

$$\kappa^s_{pq}(z) = \kappa_{pq}(z) + \phi(z)\kappa^x_{pq}(z) \tag{2.38}$$

$$\kappa^x_{pq}(z) = \frac{1}{2\sqrt{n_p n_q}(n_p - n_q)} \iint_{A_\infty} \frac{\partial n^2(x,y,z)}{\partial x} E_p^*(x,y,z) E_q(x,y,z) dxdy$$

$\kappa_{pq}(z)$ describes the device variation along the z dimension while $\kappa^x_{pq}(z)$ describes the asymmetry of the device in the x dimension.

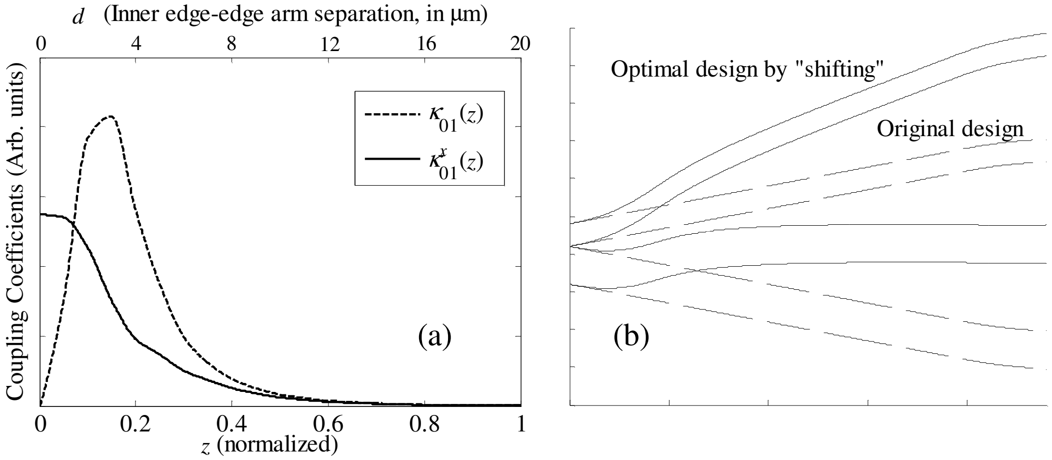

Figure 2.10: (a) The two coupling coefficients between the first two modes in the conventional design in Fig. 2.9(a); (b) the optimal device shape obtained from the "shifting" approach.

We show in Fig. 2.10(a) the typical coupling coefficient functions $\kappa_{01}(z)$ and $\kappa^x_{01}(z)$ for the conventional design in Fig. 2.9(a). The shape of $\kappa_{01}(z)$ is like an asymmetric "Gaussian", which reaches maximum at an inner edge-to-edge arm separation of d = 3 μm and exponentially decreases with larger d. At d = 12 μm $\kappa_{01}(z)$ is 15 dB lower than the maximum. In contrast $\kappa^x_{01}(z)$ monotonically decreases with d. In theory we can cancel the coupling coefficient $\kappa^s_{01}(z)$ by choosing $s(z)$ as

$$s(z) = \int_0^z \phi(z')dz' = -\int_0^z \kappa_{01}(z') / \kappa_{01}^x(z')dz' \tag{2.39}$$

In Fig. 2.10(b) we show the optimal shape deduced from Eq. (2.39) which satisfies $\kappa^s_{pq}(z) = 0$ and is close to a rotated version of the conventional design. The subtle shape variations are critical to cancel the mode coupling. When the coupling between the first mode and the second mode is completely canceled, the coupling between the second mode and the third mode reaches maximum. However, the "shifting" approach may still be useful because higher-order modes are often irrelevant.

In the "stretching" approach the formulae become

$$\begin{aligned} P_p(f) &= \left| \int_0^1 [\kappa^f_{pq}(z) \exp(j\ \delta\beta(f(z))L\ z)]dz \right|^2 \\ \kappa^f_{pq}(z) &= \kappa_{pq}(f) f'(z) \end{aligned} \tag{2.40}$$

Unlike the "shifting" approach, here the conversion efficiency can not be completely canceled because the integral of $\kappa^f_{pq}(z)$ over the length of the device is fixed under the constraints of $f(0) = 0$ and $f(1) = 1$. However we may obtain a desired target function $\kappa^f_{pq}(z)$ by varying $f(z)$. Similar to the "shifting" approach, details of the shape are also critical to the performance. For a device with $\kappa_{01}(z)$ in Fig. 2.9(a) we may apply the "stretching" approach by "stretching" the portion where d increases from 0 to 12 μm and "compressing" the remaining portions to keep the same device length. This approach may reduce the mode coupling in a short device while increasing coupling in a long device.

We can also obtain the power conversion for a combination of the "shifting" and the "stretching" approaches:

$$P_p(f,s) = \left| \int_0^1 [\kappa_{pq}(f) f'(z) + \kappa^x_{pq}(f) s'(z)] \exp(j\ \delta\beta(f(z))L\ z)dz \right|^2 \tag{2.41}$$

Variational analyses and numerical simulations show that the low crosstalk levels (typically -30dB) are limited by fabrication errors. Totally canceled crosstalk in diffused waveguides is difficult to achieve experimentally since the devices are designed with the simulated optimal shapes, whose accuracy is limited by the precision of our waveguide model. Moreover, the mask we fabricated may not reflect the designed fine features near the coupled region of an asymmetric Y-junction. Despite these limitations, we are able to observe the predicted tendency in experiments, which will be discussed in Section 6.1. The shape optimization approaches discussed in this section are also useful for other adiabatic devices, including bends, Ψ-junctions [81] and polarization splitters. [82]

2.7 Summary of Chapter 2

This chapter includes theoretical descriptions of $\chi^{(2)}$ parametric processes in RPE waveguides and the theory for optical circuit components.

After deriving coupled equations for $\chi^{(2)}$ parametric processes in waveguides involving three waves, we listed analytical solutions under special conditions. Then we analyzed the gain and temporal properties of the outputs from optical parametric generation. We further discussed cascaded processes including the cascading of SHG and OPA for CW waves and cascaded OPG with pulsed pumps. These theoretical descriptions will apply to the experiments in Chapters 3-5. For the purpose of mode demultiplexing, a parametric process must involve higher order waveguide modes. We described such processes in Section 2.4 before further discussing various optical circuit components. Based on the coupled mode theory and beam propagation method in Section 2.5 we can design optical circuit components including bends, directional couplers and asymmetric Y-junctions. The basic theory on bends and directional couplers applies to the design of quasi-group-velocity-matching devices that are used in Chapter 5. As a specific application of the coupled mode theory we discussed the optimization of asymmetric Y-junctions in Section 2.6.3, which will be experimentally verified in Section 6.1.

CHAPTER 3: HIGH PARAMETRIC GAIN IN REVERSE-PROTON-EXCHANGE LITHIUM NIOBATE WAVEGUIDES: OPA AND LOW-THRESHOLD OPG

Many applications require compact sources of tunable near- and mid-infrared ultra-short pulses with low average power. As one such source, parametric frequency converters that offer very wide tunability and require only a single pump laser have already been studied in detail. [1] Without external resonators, cavity length stabilization, or seed signals, the single-pass optical parametric generator (which is an optical parametric amplifier with $>10^{10}$ gain) offers inherent simplicity when compared with other frequency conversion systems, such as the synchronously-pumped optical parametric oscillator [83] and the continuum-seeded optical parametric amplifier [84]. However, single-pass pulse OPG has a high threshold and the temporal properties of the generated pulses depend strongly on the properties of the nonlinear materials.

Recently, ultra-short-pulse OPG systems have been studied extensively to obtain lower threshold, better pulse properties and higher conversion efficiency. In bulk materials, a threshold as low as 54 nJ with 500 fs pump pulses was reported for PPLN crystal by utilizing the high nonlinear coefficient of QPM materials. [85] Near-transform-limited (temporal and spatial) pulses were obtained with OPG in specific wavelength configurations. [64, 68, 69] Single-pass conversion efficiency of 40% was reached by matching the group velocities of the interacting waves. [71] One current challenge for practical OPG systems is to further lower the OPG threshold to levels attainable directly from laser oscillators while keeping good temporal properties of the pulses. A higher parametric gain is needed for this purpose.

In this chapter we demonstrate high parametric gain with OPA and low-threshold OPG in reverse-proton-exchange PPLN waveguides. Section 3.1 describes the design and fabrication parameters of the RPE waveguides for such experiments. In Section 3.2 we experimentally explore OPA with a CW pump by the cascading of SHG and OPA, where an internal (external) gain of 7 (6) dB is obtained for both the signal and the idler with only 175 mW CW pump power. Section 3.3 contains experimental results for OPG with picosecond pump pulses. A pump pulse with a FWHM of 1.8 ps at 769.6 nm yields a low OPG threshold of 200 pJ. The quasi-phase-matched OPG demonstrates up to 33% saturated photon conversion efficiency (internal) with 1 nJ pump pulses. The single-pass OPG is tunable from 1.15 μm to 2.3 μm for pump wavelengths between 770 nm and 789.5 nm. Section 3.4 sums up this chapter. Different approaches to improve the temporal properties of waveguide OPG will be discussed in Chapters 4 and 5.

3.1 RPE waveguides for OPG and OPA

As discussed in Section 1.3, the trade-off between focusing tightly for high intensities and focusing loosely to avoid diffraction is eliminated in waveguides. Thus, waveguide geometry can increase the parametric gain by tightly confining the optical fields over long interaction lengths and thereby lower the OPG threshold. [86] An OPG threshold of 380 pJ had been obtained in APE waveguides for picosecond pump pulses near 780 nm. [38] Because the refractive-index profile in the depth dimension in RPE waveguides is more symmetric than that of APE waveguides and thus the mode overlap is improved, the parametric gain in RPE waveguides is higher and the OPG threshold can be even lower.

Due to the phase-matching conditions, usually only a single waveguide mode is involved at each wavelength for parametric processes in waveguides. With z-cut congruent lithium niobate crystals, only TM modes can satisfy phase-matching conditions using d_{33}. Moreover, in proton-exchange z-cut lithium niobate, only TM modes are guided and the TM_{00} mode is often chosen for the best mode overlap in the parametric process.

However, for an optical parametric amplifier, the waveguide is of necessity multimode at the pump wavelength even if it supports a single mode at signal and idler wavelengths, posing a challenge for mode-launching. In multimode APE waveguides, a segmented tapered waveguide is one of the most effective ways to launch the pump beam into the TM_{00} mode. [50] In typical RPE waveguides, however, because the proton dose is lower and thus the refractive index difference is smaller than in APE waveguides, simpler adiabatic tapers also work well.

In our typical RPE devices for OPG, the waveguide width increases from 2 μm in the mode filter region to 7.5 μm in the nonlinear interaction region. The typical mode filter and taper lengths are 2 mm and 3 mm, respectively. By launching the pump from the mode filter side, > 99% of the power can be coupled into the TM_{00} mode at the end of the taper. The remnant power in the higher-order pump modes is too low to reach OPG threshold before the OPG of the TM_{00}-mode pump is in the deep saturation regime, and therefore has no effects on our results.

With long QPM gratings in RPE waveguides, we can obtain high parametric gain even with a CW pump, which will be demonstrated in Section 3.2 with the cascading of SHG and OPA. As we described in Section 2.3.1, the cascading of SHG and OPA requires two input waves in the 1550-nm band. The only difference between these OPA devices and the OPG devices is the mode filter width, which is now 3.5 μm to launch both the pump and the signal waves in the TM_{00} waveguide mode.

3.2 Continuous-wave OPA using the cascading of SHG and OPA

Although high parametric gain was experimentally demonstrated in waveguides for SHG [2] and DFG [16, 17, 87], only -5 dB internal parametric gain for the idler was obtained using ~ 200 mW CW pump power in annealed-proton-exchange waveguides. The reasons are the lower nonlinear efficiency in APE waveguides than in RPE waveguides and the shorter QPM-grating length of 41 mm. [17] When RPE waveguides were first tried for the cascading of SHG and OPA, an internal (external) gain of 5 (1.8) dB had been observed with a high loss of 0.35 dB/cm in the waveguides. [42] The external gain can be further improved by using RPE waveguides with a low propagation loss of <0.15 dB/cm which we recently fabricated. Here we demonstrate OPA in such low-loss RPE waveguides with 58-mm-long uniform QPM gratings, in which the cascading of SHG and OPA results in up to 7 (6) dB internal (external) gain for both the signal and idler. As we illustrate in Fig. 2.2, in this process the driving wave for the 1550-nm band OPA is the SHG product of a strong pump wave near 1550 nm.

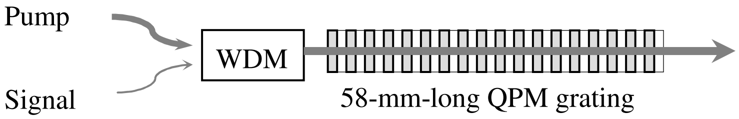

Figure 3.1: The configuration for the cascading of SHG and OPA in a RPE waveguide. The pump and signal are combined using a WDM coupler and then launched into a waveguide.

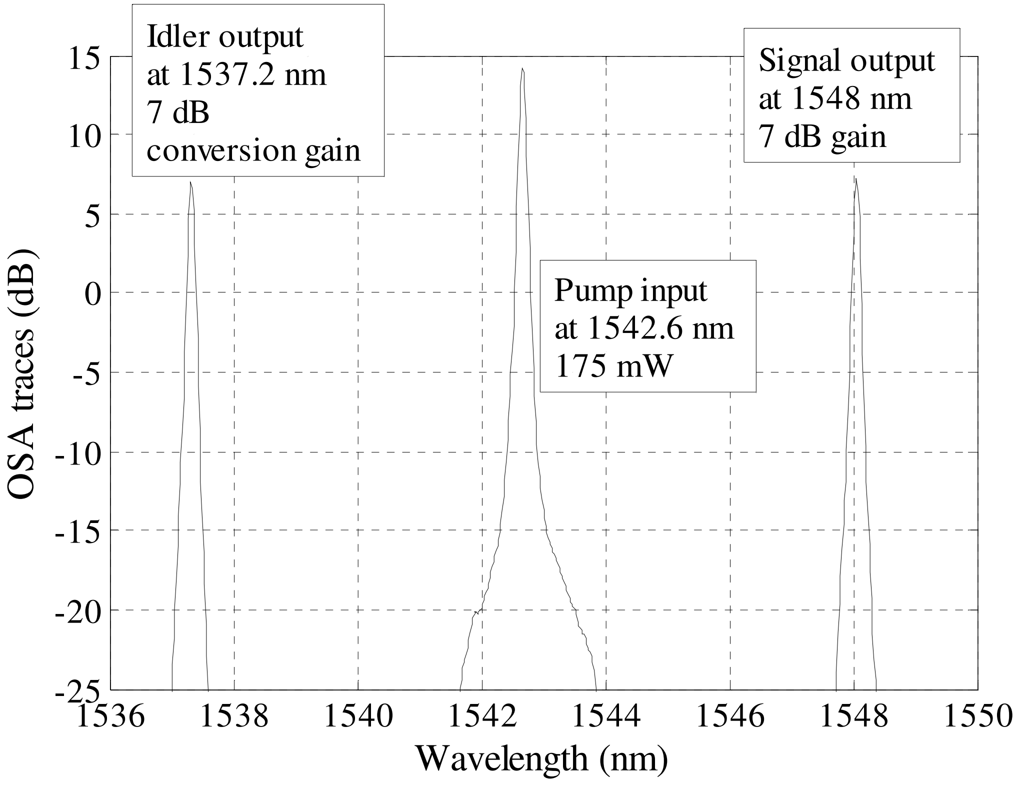

Figure 3.2: The power spectrum of the cascading of SHG and OPA in a RPE waveguide with a 58-mm-long QPM grating and 175 mW pump power. The gains shown are the internal gains.

In the configuration shown in Fig. 3.1, the pump at 1542.6 nm and the signal at 1548 nm are combined with a fiber WDM coupler and then coupled into the RPE waveguides on a fiber pig-tailing stage at room temperature. We measure the output with an optical spectrum analyzer (OSA) and calculate the signal (idler) gain by comparing peaks in the OSA traces with or without launching the pump wave. An example is shown in Fig. 3.2 showing an internal signal (idler) gain of 7 dB, where the pump (signal) power is 175 (0.44) mW and the input signal level measured at the end of the device without launching the pump is set as 0 dB. Considering the <0.15 dB/cm propagation loss in the 1550-nm band in a 63-mm-long waveguide, the external gain is ~6 dB.

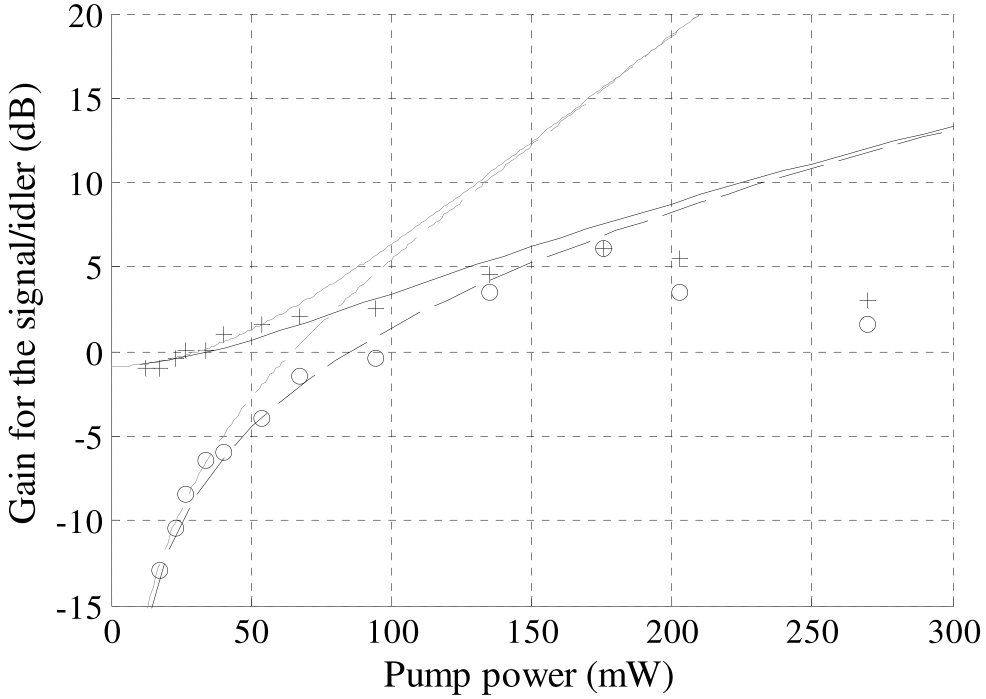

Figure 3.3: The external signal (idler) gain for the cascading of SHG and OPA in a RPE waveguide with a 58-mm-long QPM grating. The solid (dashed) curves are from simulations and the cross (circle) symbols are from measurements for the signal (idler). The black curves are from numerical simulations while the gray curves are from Eq. (2.26) in which pump depletion is neglected.

Figure 3.3 shows the external OPA gain for the signal (idler) as a function of the pump power. The cross (circle) symbols are from experimental measurements for the signal (idler) while the solid (dashed) curves are from simulations with 0.15 dB/cm loss for waves ~1540 nm and 0.3 dB/cm loss for waves ~770 nm. The normalized nonlinear coefficient η_0 for SHG was ~100%/W-cm^2. The black curves are numerical simulation results for Eq. (2.25) while the gray curves are obtained from the analytical formulae Eq. (2.26) in which pump depletion is neglected. The substantial difference between the black curves and the gray curves means that pump depletion is significant when the pump power is >50 mW. The numerical simulation results with the pump depletion in SHG fully considered match well with the experimental results for a pump power <175 mW.

When the pump power is >175 mW, notable discrepancy between the numerical and experimental results occurs and in the experiments the gain decreases with higher pump power. Possibly this discrepancy comes from non-uniformity in the long waveguides and QPM gratings. The pump is now significantly depleted; the simple theory in Section 2.3.1 cannot correctly predict the outcome in the regime of strong pump depletion. [42]

Another possible source for the discrepancy is the parasitic processes caused by higher-order quasi-phase-matching in the long QPM gratings, which are not included in the analysis in Section 2.3.1 and are difficult to eliminate. Such parasitic processes include the sum-frequency generation between the pump wave and the second-harmonic wave which generates green waves and the SHG of the second-harmonic wave near 770 nm which generates blue waves. High intensity green and blue waves would cause photorefractive damage (PRD) in congruent lithium niobate crystals at room temperature; [88, 89] the RPE waveguide devices therefore are heated to > 100 °C to avoid serious PRD. This is absolutely necessary for pulsed OPG where the peak pump power is >100 W which we will discuss further in Section 3.3.

Since the external OPA gain for the idler is >0 dB with 100-mW pump power, waveguide OPO may be constructed by using RPE lithium niobate waveguides as the gain media and using a fiber loop to form a cavity.

3.3 Experimental results for low-threshold OPG

OPG is OPA with >10^{10} parametric gain and uses vacuum noise as the input. In Section 2.1 we have estimated a picojoule OPG threshold in RPE waveguides for picosecond pump pulses near 780 nm.

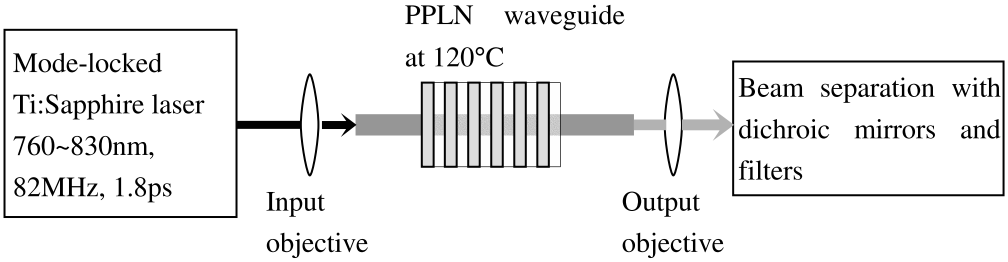
PPLN waveguide at 120°C
Mode-locked Ti:Sapphire laser 760~830nm, 82MHz, 1.8ps
Input objective
Output objective
Beam separation with dichroic mirrors and filters

Figure 3.4: The experimental setup for waveguide OPG.

As shown in Fig. 3.4, in the OPG experiments the pump laser is a mode-locked Ti:Sapphire laser generating 1.8 ps (FWHM) transform-limited pulses around 780 nm with a repetition rate of 82 MHz. A variable attenuator is used to control the peak power of the pulses while an acousto-optic modulator (AOM) at 10-kHz repetition rate with 1% duty cycle is used to lower the average power, as a precaution to avoid photorefractive damage in the congruent $LiNbO_3$ waveguides. The chips are heated to 120 °C for the same reason. The RPE waveguides are fabricated with a proton-exchange time of 24.5 hrs at 171 °C, an annealing time of 22 hrs at 312 °C, and a reverse-exchange time of 25 hrs at 300 °C. 0.5-mm-thick PPLN samples with QPM periods ranging from 15 μm to 16.65 μm and various grating lengths are used in the experiment. The effects of cascaded OPG which we described in Section 2.3.2 are excluded in this chapter and will be discussed in the following two chapters.

The conventional-OPG pump throughput and photon conversion efficiency curves (internal) with 1.8-ps pump pulses at 769.6 nm are shown in Fig. 3.5. The signal wavelength is centered at 1350 nm, with a bandwidth of 10 nm. In this measurement the QPM gratings have a period of 15.75 μm and is 40-mm long, which is >6 times the signal-pump group-velocity-mismatch length. The waveguide is 7-μm wide in the interaction regions.

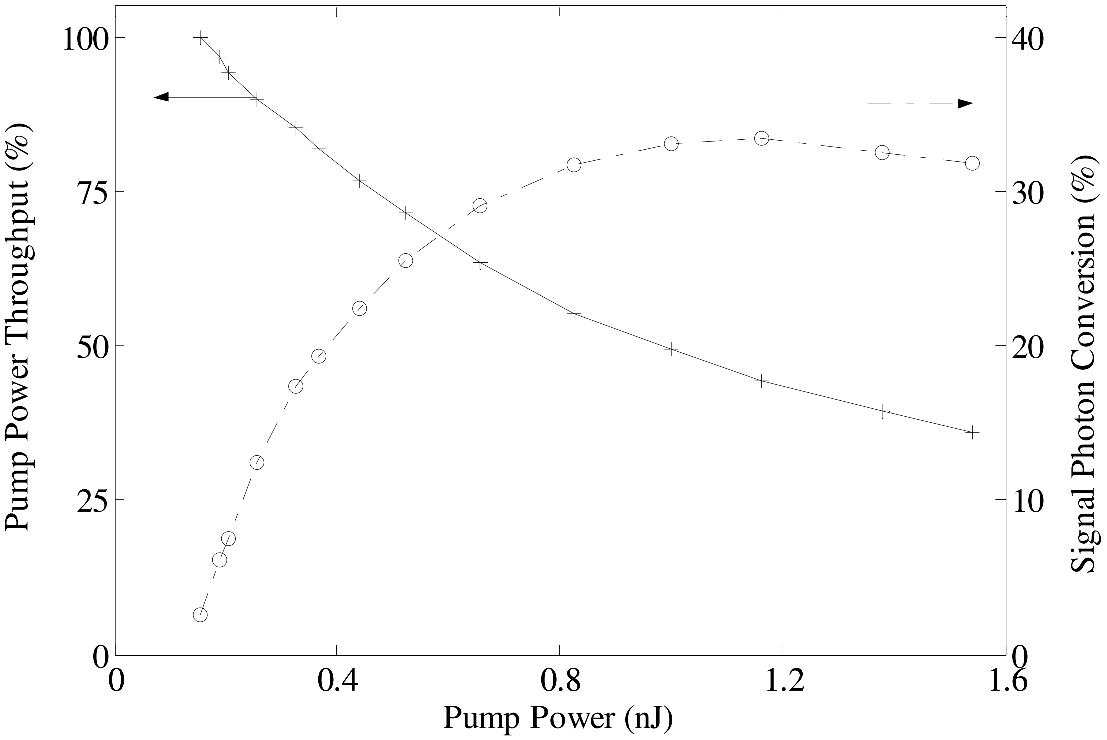

Figure 3.5: The pump throughput and the internal signal-photon conversion efficiency in single-pass OPG with a 40-mm-long QPM grating in the absence of cascaded OPG. The 1.8-ps-long (FWHM) pump pulse is at 769.6 nm and the signal wavelength is centered at 1350 nm.

The curves in Fig. 3.5 show an OPG threshold of 200 pJ, matching well with the calculated threshold of 190 pJ, using the theory for OPG in Section 2.2 and the measured normalized SHG conversion efficiency (internal) of 90 %/(W-cm^2) from similar samples. The maximum saturated internal photon conversion efficiency is 33%, matching the value of 35% estimated from simulations. The decrease in efficiency after saturation comes from SHG of the pump and other parasitic cascaded processes at high pump power.

The typical OPG tuning behavior of the RPE waveguides is shown in Fig. 3.6. The waveguide width is 7.5 μm and the 18-mm-long QPM grating has a period of 16.25 μm.

The theoretical prediction fits the measurements well. In a similar waveguide with a different QPM period, the output wavelengths range from 1.15 μm to 2.3 μm for pump wavelengths between 770 nm and 789.5 nm. The upper limit of the idler tuning range is the cutoff wavelength of the waveguide, which is estimated to be 2.5 μm for the RPE waveguides used in this experiment. Although the OPG threshold is lower for near degenerate operation, it is a weak function of the pump wavelength within the tuning range.

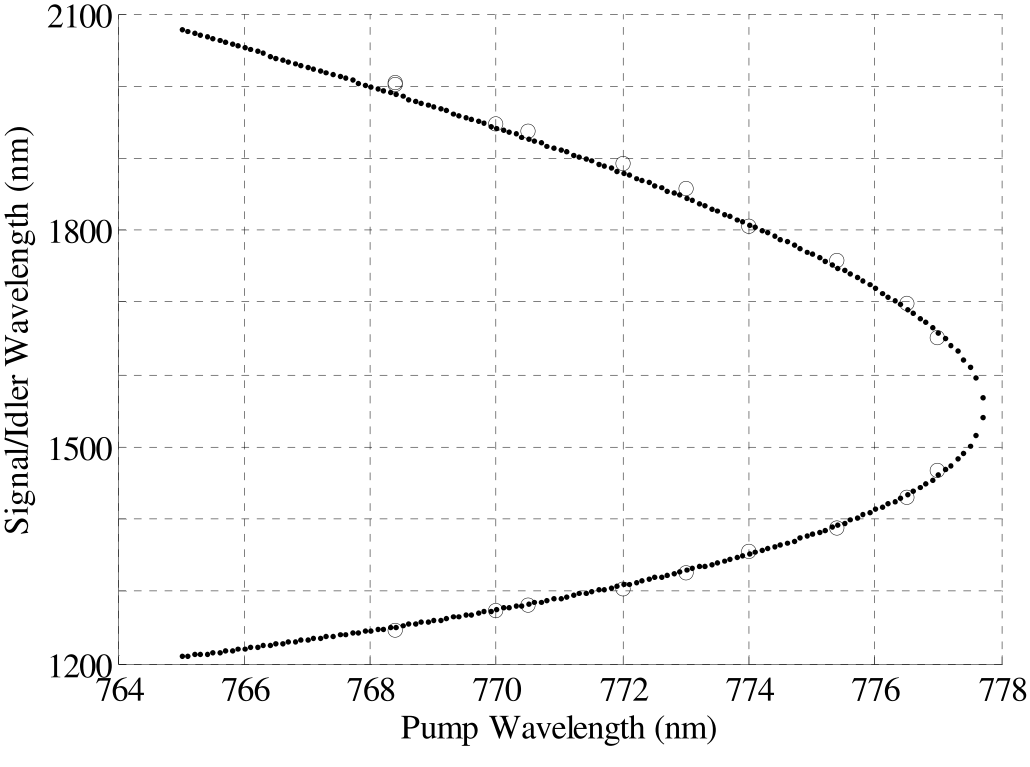

Figure 3.6: Pump tuning curve of a RPE PPLN waveguide at 120 °C. The dotted curve is a simulation based on our waveguide dispersion model. [49] The circle symbols are measurements. The output wavelength ranges from 1245 nm to 2005 nm for pump wavelength between 768.4 nm and 777.5 nm.

As we do not have a loss coefficient function versus wavelength, we do not include the loss terms in the coupled equations for the simulation. While this assumption may cause discrepancy in comparing the experimental and numerical results, the effects prove to be small in practice.

The two-photon absorption process in waveguides can also affect the OPG threshold. The high-order quasi-phase-matched SHG of the 780-nm pump generates blue radiation near 390 nm, which is above the two-photon absorption edge. For low-gain devices with a SHG conversion efficiency below 10 %/(W-cm^2), it would dominate and deplete the pump before the OPG threshold can be reached. However, for the high gain RPE waveguides, we can ignore it because the OPG gain is exponential while the SHG gain is quadratic in the grating length.

In congruent lithium niobate crystals, photorefractive damage is caused by green light or waves with even shorter wavelengths which are generated by parasitic processes. If the intensities of those waves are high the waveguides are slowly damaged by this effect even if they are heated up to 150 °C. This problem can be solved by replacing the congruent material with MgO-doped or near-stoichiometric lithium niobate crystals in which the PRD threshold is much higher. [45, 46, 90, 91]

3.4 Summary of Chapter 3

In this chapter we have demonstrated that periodically-poled RPE lithium niobate waveguides can operate as high gain parametric devices for OPA and OPG.

After describing the design parameters of the waveguides, we presented CW OPA with 7 (6) dB internal (external) gain for both the signal and the idler by SHG to generate the pump, followed by OPA. With a pulsed pump, and in the absence of cascaded OPG, we demonstrated thresholds as low as 200 pJ for picosecond optical parametric generation in RPE waveguides. A saturated internal photon conversion efficiency of 33% was obtained with 1 nJ of pump energy for a 1.8 ps (FWHM) pump pulse at 769.6 nm. The signal wavelength tuning range was from 1.15 μm to 2.3 μm with a pump wavelength between 770 nm and 789.5 nm.

Besides a low threshold for OPG, good temporal properties of the output pulses are also important. In the next two chapters we will explore different approaches to improve the temporal properties of the OPG output.

CHAPTER 4: CASCADED OPTICAL PARAMETRIC GENERATION IN REVERSE-PROTON-EXCHANGE LITHIUM NIOBATE WAVEGUIDES

In the previous chapter we described low-threshold OPG in RPE lithium niobate waveguides. In this chapter we begin exploring approaches to improve the temporal properties of the pulsed OPG.

As we discussed in Sections 2.2 and 2.3.2, the temporal properties of the pulses generated by conventional OPG depend strongly on the dispersion of the nonlinear material, and the bandwidth of the output pulses are usually much broader than the transform limit, except for special combinations of pump, signal and idler wavelengths. [64, 68] A challenge for practical OPG systems is to obtain OPG output with good temporal properties under general conditions. Cascaded OPG is one of the approaches to solve this problem.

In general one can narrow the spectrum of the signal and idler by adding extra frequency filters, at the expense of added complexity and substantial energy loss. However, this high loss can be avoided in cascaded OPG which uses an extra parametric process as the filter. Cascaded OPG can only occur at signal wavelengths where OPG and another parametric process are simultaneously phase-matched, which is illustrated in Fig. 2.3 using the case where the extra parametric process is the sum-frequency generation between the pump and the signal. When the group velocity of both the signal and idler waves is faster than the pump wave while the extra wave at the sum frequency is slower than the pump wave, simulations and experimental results show that the temporal properties of the cascaded OPG products can be better controlled than those of the conventional OPG products. [15]

In the early sections of this chapter we study the effects of cascading on pulsed OPG. In Section 4.1 we will discuss the effects of cascaded OPG on the photon conversion efficiency and pump depletion for OPG in uniform QPM gratings. In Section 4.2 we will study details of cascaded OPG in uniform QPM gratings of different lengths and demonstrate the improvements of temporal properties in cascaded OPG. Using a frequency-resolved cross-correlator, [92] we directly identify and distinguish the products from cascaded OPG and conventional OPG in both the frequency domain and the time domain.

Another important aspect for practical applications, the wavelength tuning ability, is different for conventional OPG and cascaded OPG. In the experiments described in Chapter 3, the signal and idler wavelengths from conventional OPG are widely tunable by tuning the pump wavelength (or the device temperature). However the center wavelength of the signal from cascaded OPG is not a strong function of the pump wavelength or the device temperature. In a RPE waveguide with a pump wavelength ~780 nm and a uniform QPM grating having a period around 16.2 μm it can only be tuned by several nanometers around three wavelengths: 1190 nm, 1280 nm, or 1430 nm because the extra phase-matched process in cascaded OPG limits the tuning ability of the device.

These three wavelengths correspond to the three strongest cascaded processes in uniform QPM gratings; other cascaded processes are insignificant. Besides optical parametric generation with first-order QPM ($K_g = K_g^{OPG} = \Delta k_{OPG}$), these three cascaded processes involve also second-harmonic generation of the signal, which generates yellow light around 595 nm by second-order QPM ($2K_g = K_g^{SHG} = \Delta k_{SHG}$), sum-frequency generation between the pump and the idler which generates green light around 550 nm by second-order QPM ($2K_g = K_g^{SFG,1} = \Delta k_{SFG,1}$), and sum-frequency generation between the pump and the signal which is illustrated in Fig. 2.3 and generates green light around 500 nm by third-order QPM ($3K_g = K_g^{SFG,2} = \Delta k_{SFG,2}$), respectively. The gain coefficient for the extra parametric process can be calculated from Eq. (1.2) if the duty cycle of the uniform QPM grating is known.

Although, as we discuss above, the tuning ability of cascaded OPG in a single device is limited, we can engineer QPM gratings and realize wide-band tuning by using several devices of different designs. By phase-modulating QPM gratings to synthesize desirable frequency responses we are able to control the wavelength of the near-transform-limited signal from cascaded OPG. With these engineered QPM gratings we may widely tune the signal wavelength by switching between different devices on the same chip, and temperature tune over a narrower wavelength range, while retaining controlled temporal properties. We will discuss phase-modulated QPM gratings in Section 4.3.

Without losing generality, in this chapter we only consider the strong cascaded OPG processes involving sum-frequency generation. With strong enough SFG gain, not only is the signal (idler) transform-limited, but so also is the visible SFG product. This phenomenon is similar to up-converted parametric generation. [93]

If not otherwise specified the basic experimental setup in this chapter is the same as that in Section 3.3.

4.1 Effects of cascaded OPG on photon conversion efficiency and pump depletion

Although the OPG threshold is not affected, the presence of cascaded OPG significantly changes the photon conversion efficiency and pump depletion.

In the experiments reported in this section, the FWHM of the pump pulses is 1.8 ps, all the interacting waves are in the TM_{00} mode, the QPM grating periods in the devices are 16.45 μm and the chips are heated to ~ 130 °C. The RPE waveguides are fabricated with our usual procedure described in Sections 1.3 and Section 3.3 with a proton-exchange depth of ~1.84 μm. The sum-frequency generation in cascaded OPG is between the idler and the pump using 2nd-order QPM. The pump is around 770 nm and the signal is near 1245 nm.

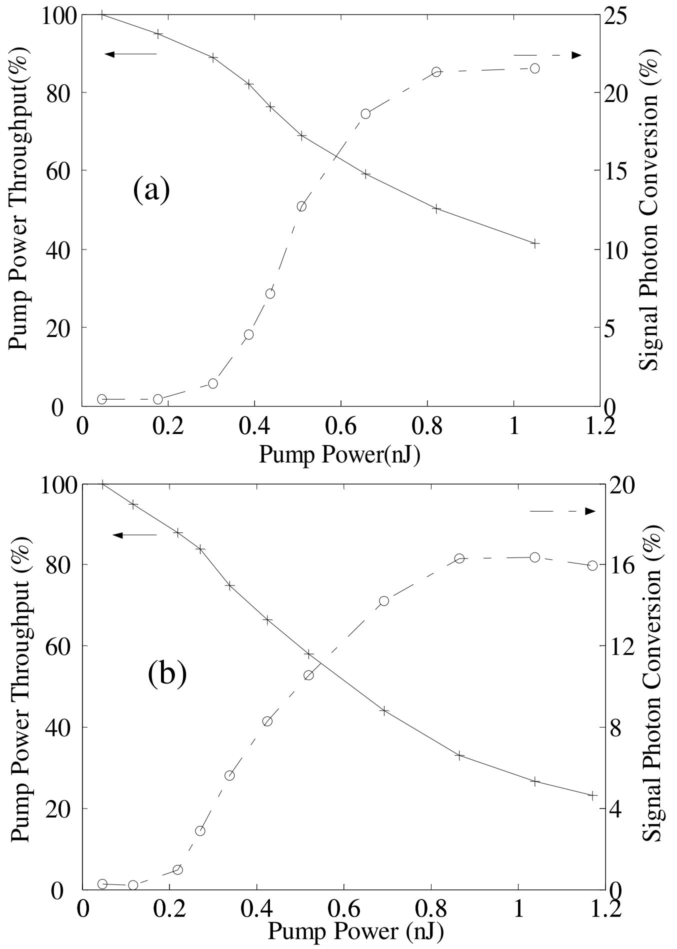

Figure 4.1: The internal pump throughput ratio and signal photon conversion efficiency. (a) for a 12-mm-long QPM grating, no cascaded OPG contributes; (b) for an 18-mm-long QPM grating, with contributions from cascaded OPG.

The internal pump throughput and signal photon conversion efficiency curves for two different grating lengths are compared in Fig. 4.1. For the same pump power range, the cascaded products are negligible in the devices with a 12-mm-long QPM grating, but become significant for a longer grating length of 18 mm. Although more pump depletion is observed for the longer QPM gratings, less signal photon conversion is recorded because the sum-frequency output accompanies the emergence of cascaded OPG. The thresholds for both cases are near 200 pJ, confirming the results from numerical simulations that the OPG threshold is a weak function of the grating length when it is >2.5 times the group-velocity-walkoff length between the signal and the pump.

4.2 Effects of Cascaded OPG on temporal properties

The temporal properties of cascaded OPG in uniform QPM gratings can be revealed by numerical simulations using the methods described in Section 2.3.2. Such results are illustrated in Fig. 4.2, using an example involving OPG and the sum-frequency generation between the signal near 1428 nm and the pump near 780 nm.

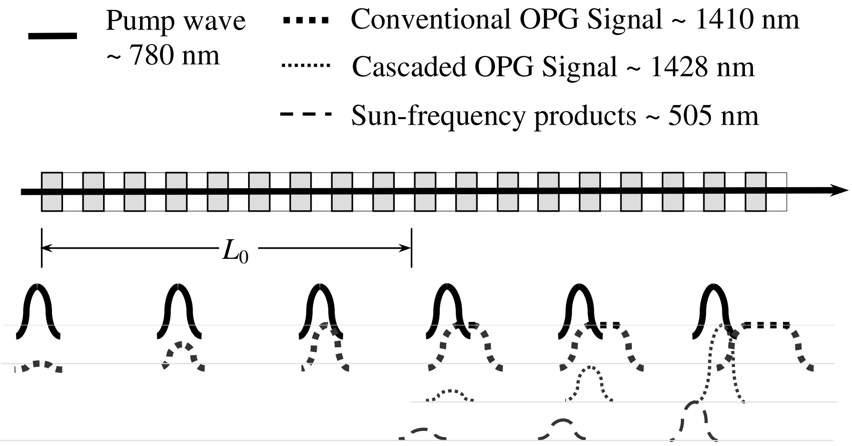
Pump wave ~ 780 nm
Conventional OPG Signal ~ 1410 nm
Cascaded OPG Signal ~ 1428 nm
Sun-frequency products ~ 505 nm
L_0

Figure 4.2: Illustration of the evolution of different pulse shapes for conventional OPG and cascaded OPG. No propagation loss is considered for the pump. L_0 is the build-up length for the sum-frequency generation in cascaded OPG, defined in Eq. (4.1).

If we fix the grating length and increase the pump power, conventional OPG will reach threshold first, with dips appearing at wavelengths where the quasi-phase-matching conditions for sum-frequency generation are satisfied. If the length of the QPM grating is much longer than the group-velocity-walkoff length between the signal and the pump, the output signal pulse would have a flat-top shape due to group-velocity-mismatch, if the pump is lossless. Further increasing the pump power, the cascaded OPG will reach its threshold if the QPM grating length is longer than build-up length L_0 for SFG, to be defined in Eq. (4.1).

The sum-frequency generation in cascaded OPG has a build-up length L_0 because both SFG and its back conversion are involved.

In pure sum-frequency generation, the power distribution among the interacting waves oscillates following $\sin^2(\sqrt{\eta_{SFG}P}L)=\sin^2[\pi L/(2L_0)]$ [11] where η_{SFG} is the normalized gain parameter in the sum-frequency generation and P is the peak pump power. L_0 is half the oscillation period, after which the back conversion of sum-frequency generation starts if there is no input sum frequency wave. Although the sum-frequency generation in cascaded OPG is more complex than pure sum-frequency generation, it still has a characteristic length which we call the build-up length and keep the notation L_0:

$$L_0 \sim (\pi/2)/\sqrt{\eta_{SFG}P} \tag{4.1}$$

As shown in Fig. 4.2, only after this length does the back conversion of sum-frequency generation start and does cascaded OPG occur. The cascaded OPG signal photons therefore are generated in the rear part of the QPM gratings.

We may roughly estimate L_0 = 5 mm with η_{SFG} = 10%/W-cm^2 for a peak pump power of 100 W which is near the OPG threshold for picosecond pulses. By numerically solving Eq. (2.29) we obtained L_0 ~ 12 mm. The discrepancy between these values for L_0 comes from the group-velocity-mismatch neglected in deriving the analytical estimation.

The threshold of cascaded OPG is higher than that of conventional OPG because sum-frequency generation is required. Once the threshold is reached, however, intrinsic to the cascaded process, the cascaded signal is synchronized to the pump and the group velocities of the waves are effectively matched, so that the cascaded OPG grows up exponentially faster than the conventional OPG products. In addition, if the QPM grating is much longer than L_0, the cascaded OPG products become dominant, and the whole output pulse would be near transform-limited.

These numerical results are experimentally verified with several different approaches, including comparing results from the same device at different pump power levels (Section 4.2.1), comparing results for different QPM grating lengths ranging from 6 mm to 42 mm (Section 4.2.2), and comparing properties of the signal (idler) in different frequency ranges for the same device at a fixed pump power level using a frequency-resolved cross-correlator (Section 4.2.3). Before showing experimental results using each of these approaches in the following subsections we will describe how we recorded signal (idler) pulse shapes.

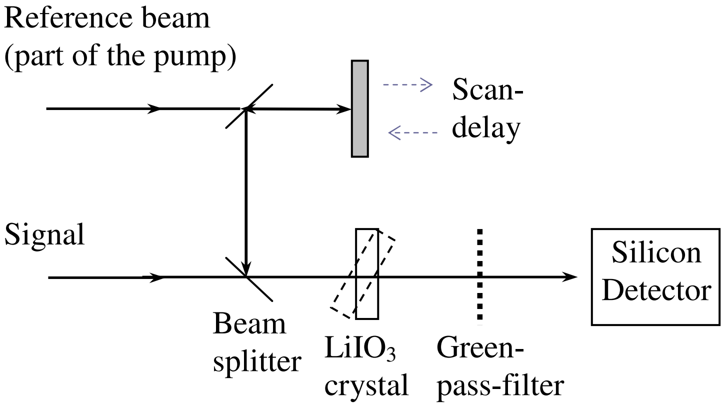

Figure 4.3: A diagram of the frequency-resolved cross-correlator. The scan-delay ensures that the pump and signal pulses temporally overlap in the LiIO$_3$ crystal and have maximum efficiency for sum-frequency generation. By replacing the LiIO$_3$ crystal and the silicon detector with a GaAsP photodiode we obtain a cross-correlator without frequency resolvability.

Cross-correlation based on two-photon-absorption [94, 95] is used in Sections 4.2.1 and 4.2.2, while frequency-resolved cross-correlation [92] is used in Section 4.2.3. The former uses a GaAsP photodiode while the latter uses a piece of LiIO$_3$ crystal and a silicon detector. The experimental setup for the latter is shown in Fig. 4.3. By angle phase-matching the type-I sum-frequency generation between the signal (idler) and a reference beam split from the pump wave, the 0.25-mm-thick LiIO$_3$ crystal serves as a tunable band-pass filter with a filter function of $\mathrm{sinc}^2[(\lambda-\lambda_0)/\Delta\lambda]$. The bandwidth $\Delta\lambda$ of the filter is ~38 nm for signal near 1430 nm. The center wavelength λ_0 is determined by the tilting angle of the $LiIO_3$ crystal. Using this "filter" we can obtain the pulse shape in selected spectral bands. [92] By replacing the $LiIO_3$ crystal and the silicon detector with a GaAsP photodiode we obtain a cross-correlator without frequency resolvability.

4.2.1 Temporal properties of OPG output at different pump power levels for a 18-mm-long QPM grating

The dynamics of the cascaded OPG process is clear from the temporal properties of the output, as shown in Fig. 4.4, which corresponds to the same device used for Fig. 4.1 (b). The shape and length of the pulse is measured with a cross-correlator based on the two-photon-induced photocurrent using GaAsP photodiodes, [94, 95] using a small portion split from the pump as the reference beam. When the pump power is increased, new peaks appear in both the frequency domain and the time domain. These new peaks correspond to the cascaded OPG output.

If we consider only the cascaded product component, the time-bandwidth product of the generated signal is 0.51 with a pulse length of 1.9 ps and a bandwidth of 1.4 nm. The conventional OPG product has a time-bandwidth product of 4.4. Time-bandwidth product for a transform-limited Gaussian pulse is 0.441. By making use of the cascaded process, we have generated a signal with a much reduced time-bandwidth product close to the transform limit.

The signal bandwidth in cascaded OPG is much narrower than that in conventional OPG. As a result, although in Fig. 4.4(b) the temporal peak of the cascaded OPG is lower than the conventional OPG peak, on the top four curves in Fig. 4.4(a) spectral peak of the cascaded OPG is higher. The peak positions in the spectra in Fig. 4.4(a) shift from conventional-OPG to cascaded-OPG with increasing pump pulse energy.

The time delay between the two different types of OPG products is 3.6 ps in Fig. 4.4(b), meaning that the majority of the cascaded OPG signal is generated near the end of the 18-mm-long QPM grating. In a longer QPM grating a greater portion of the output would be in the cascaded component, which we will discuss in Section 4.2.2.

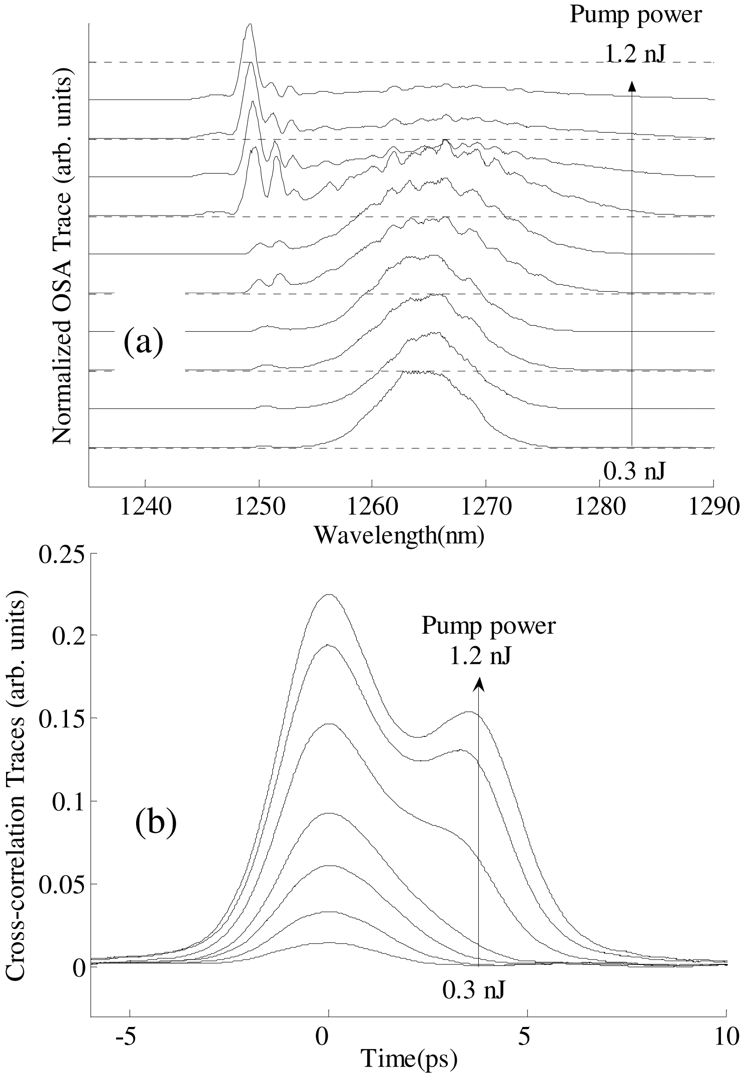

Figure 4.4: (a) Power spectra from optical spectrum analyzer traces (b) Cross-correlation traces for the output from OPG in an 18-mm-long QPM grating. Both cover the same pump power range from 0.3 nJ to 1.2 nJ. Note the peak positions in the spectra shift from conventional-OPG to cascaded-OPG with increasing pump pulse energy. Cross-correlation traces also show both products.

4.2.2 Cascaded OPG for QPM-grating lengths ranging from 6 mm to 42 mm at pump powers resulting in a constant photon conversion efficiency

Figure 4.5 shows the power spectra and the pulse shapes of the OPG signal from waveguides with uniform QPM gratings of different lengths.

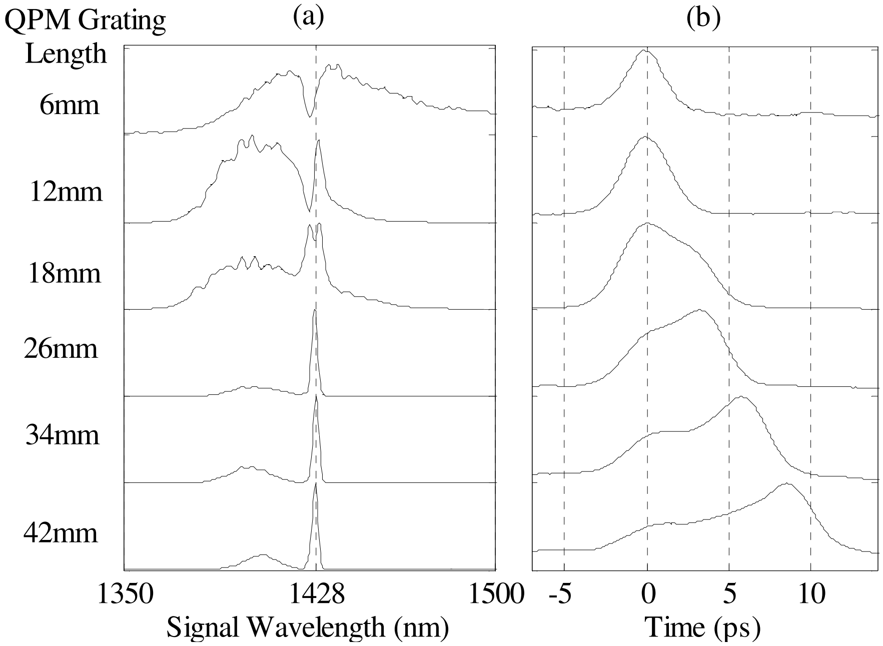

Figure 4.5: (a) The power spectra and (b) the pulse shapes for the signal from optical parametric generation in lithium niobate waveguides with different QPM-grating lengths. The photon conversion efficiencies for all these traces are ~10% except for the 6-mm-long grating for which it is only 2%. The peak of the conventional OPG products is set as the time zero for all the curves in (b). All the curves are normalized to their maxima.

All the devices are fabricated side-by-side on the same chip and the duty cycles of the QPM gratings are nominally 50%. The OPG threshold is around 200 pJ for the devices with a QPM-grating length over 18 mm, the same as was obtained in Chapter 3. For a fair comparison for the different QPM-grating lengths, the pulse shape and spectrum data are taken at pump powers resulting in a total photon conversion efficiency of ~10%, except for the 6-mm-long grating, which has only 2% efficiency with the maximum available pump power. This exception does not affect our conclusions in the following because cascaded OPG output is absent in the shortest 6-mm-long QPM gratings.

The pulse shapes were again obtained from cross-correlation based on two-photon-absorption in GaAsP photodiodes with a reference beam split from the pump. [94, 95] In such a measurement the signal and the idler in the entire frequency band were simultaneously recorded. Although the idler was not removed by a filter, according to simulations it would only slightly affect the pulse shape recorded by the cross-correlator because the group velocity mismatch between the signal around 1420 nm and the idler around 1750 nm was < 1/10 of that between the signal (idler) and the pump near 784 nm, [96] so that the signal and idler pulses are nearly overlapping in time. We will revisit this conclusion in Section 4.2.5 after we have discussed more experimental details of cascaded OPG.

By comparing different curves in Fig. 4.5 to simulations we can identify the conventional OPG and cascaded OPG products both in the frequency domain and in the time domain. In the frequency domain, the narrow peaks around 1428 nm correspond to the cascaded OPG products. In the time domain, the time zero is set at the peaks of the conventional OPG products.

Comparing the curves in Fig. 4.5 we can see how cascaded OPG and conventional OPG compete with each other. Only for gratings longer than 18 mm does the extra signal peak from cascaded OPG dominate in the frequency domain and become distinguishable in the time domain. When we isolate the cascaded OPG signal around 1428 nm from the conventional OPG signal in the time domain by deconvolving the cross-correlation traces for long QPM gratings, a time-bandwidth-product of ~0.4 is obtained for the cascaded OPG signal. The power spectra of the signal from QPM gratings shorter than 18 mm show strong interferences between the two different processes. We can deduce from Fig. 4.5 that the build-up length L_0 for the sum-frequency generation is ~12 mm for a pump power above the OPG threshold. These results complement those in Section 4.2.1, where the evolution of the pulse shapes at various pump power levels in a device with an 18-mm-long QPM grating was analyzed.

4.2.3 Frequency-resolved cross-correlation measurements

We have found the correspondence between the signal peaks in the time domain and the frequency domain and identified the conventional OPG and cascaded OPG peaks either by varying the pump power level, as in Section 4.2.1, or by comparing devices of different lengths as in Section 4.2.2. In a different approach, we can directly identify cascaded OPG and conventional OPG products by measuring a single device at a fixed pump power, using the frequency-resolved cross-correlator shown in Fig. 4.3.

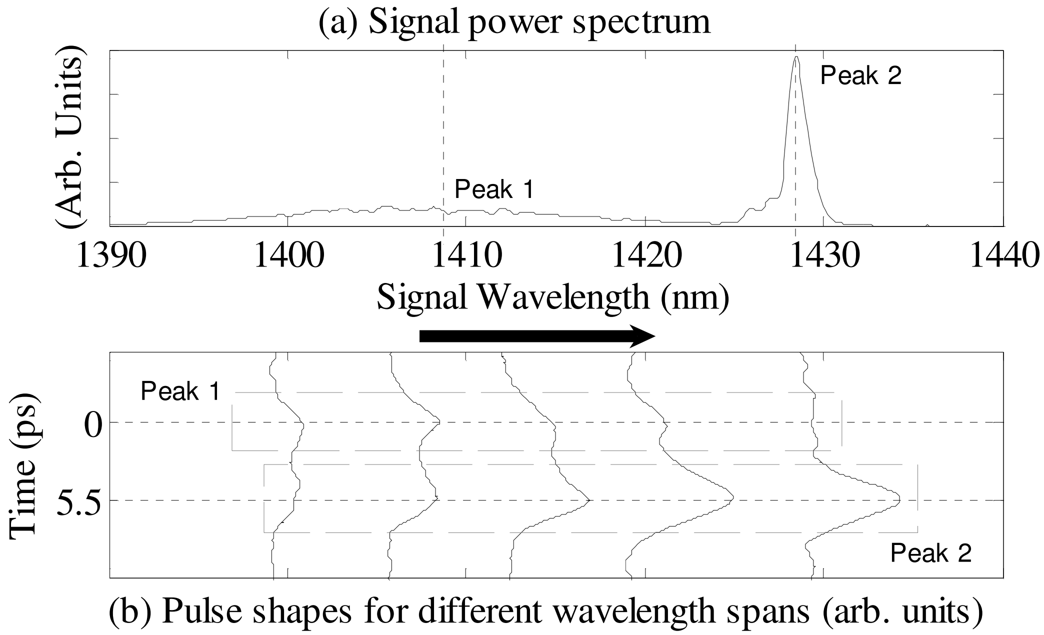
(a) Signal power spectrum

(b) Pulse shapes for different wavelength spans (arb. units)

Figure 4.6: (a) The signal power spectrum at a pump power level resulting in a photon conversion efficiency of ~10% with a pump wavelength of 784.4 nm. (b) Pulse shapes of the OPG signal in different wavelength ranges with a 38-nm-wide sinc^2-shape band-pass filter. In order to show the correct relative power the curves in (b) are not normalized. Baselines are shifted to indicate center signal wavelength for each trace, which can be read out from the *x*-axis of (a). On each curve, peak 1 corresponds to the conventional OPG products and peak 2 corresponds to the cascaded OPG products.

Results from such a measurement are shown in Fig. 4.6, including the power spectrum and the pulse shape for the signal from a device with a 34-mm-long QPM grating at a pump power level resulting in a photon conversion efficiency of ~10%.

Each curve in Fig. 4.6(b) is a frequency-resolved cross-correlation trace, corresponding to a wavelength range whose center is determined by the band-pass filter in the frequency-resolved cross-correlator. This center wavelength is indicated by the baseline of each curve and can be read out from the x-axis of Fig. 4.6(a). From the peak-intensity variations in the different curves in Fig. 4.6(b) we can deduce the correspondence between the two peaks in the frequency domain and the two sets of peaks in the time domain. The conventional OPG products and the cascaded OPG products are respectively marked as peak 1 and peak 2. Although the large bandwidth of the thin $LiIO_3$ crystal used in our frequency-resolved cross-correlator limited the contrast between the peaks on different curves in Fig. 4.6(b), the cascaded OPG and conventional OPG products are nevertheless identified and are consistent with results discussed in Sections 4.2.1 and 4.2.2.

4.2.4 Study of cascaded OPG and conventional OPG under different levels of pump depletion

By summing up the frequency-resolved cross-correlation traces in different wavelength ranges we can restore the pulse shape for the whole signal band with the idler contribution removed.

Figure 4.7 shows the power spectra and the pulse shapes under different levels of pump depletion obtained this way for the device used for Fig. 4.6. The dash-dotted curves were obtained at a pump power level resulting in a photon conversion efficiency of ~20% when the pump wavelength was 782.8 nm and cascaded OPG was absent. All other curves were obtained when the pump wavelength was 784.4 nm and the cascaded OPG signal was near 1428 nm. The photon conversion efficiency was respectively about 10%, 20% and 30% for the solid, dashed and dotted curves.

The experimental results match the simulation results obtained from solving Eq. (2.29), which are similar to the data, and for clarity are not shown in the figure. We can explain the different pulse shapes in Fig. 4.7(b) with the mechanisms of conventional OPG and cascaded OPG.

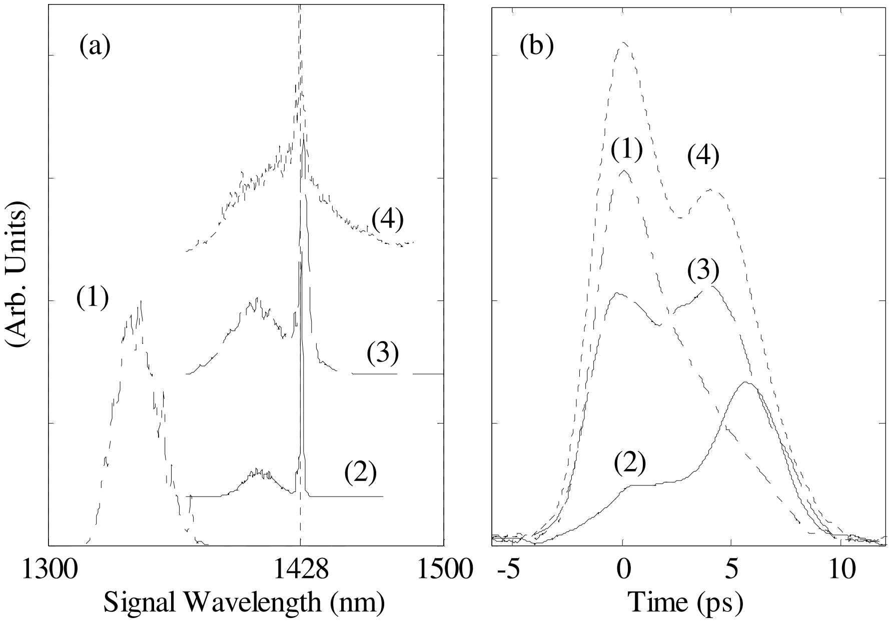

Figure 4.7: (a) The signal power spectra and (b) the pulse shape for OPG in a waveguide with a 34-mm-long QPM grating. In both figures, the dash-dotted curves (1) correspond to a pump wavelength of 782.8 nm and a photon conversion efficiency of ~20%; cascaded OPG is absent. For the solid (2), dashed (3) and dotted (4) curves, the pump wavelength is 784.4 nm, strong cascaded OPG is present, and they respectively correspond to a total photon conversion efficiency of about 10%, 20% and 30%. All the curves in (a) are normalized to their maxima and the baselines are shifted for a clear comparison in their peak positions, while the curves in (b) are not normalized and hence show a correct comparison in photon conversion efficiencies.

The dash-dotted curve in Fig. 4.7(b) corresponds to conventional OPG with no cascading. Because the grating length of 34 mm was much longer than the group-velocity-walkoff length of ~5 mm between the signal and the pump, the output signal pulse would have a flat-top shape due to group-velocity-mismatch if the pump were lossless, as illustrated in Fig. 4.2. However the propagation loss for the pump was ~0.3 dB/cm in the waveguides and the pump depletion was significant when the photon conversion efficiency was 20%, and the gain depends exponentially on the pump power, so that most of the conventional OPG signal photons are generated in the front part of the QPM grating. The signal pulse shape thus became asymmetric.

The solid, dashed and dotted curves in Fig. 4.7 correspond to combinations of cascaded OPG and conventional OPG under different levels of pump depletion and can be explained by further considering the mechanism of cascaded OPG which involves sum-frequency generation and its back conversion.

The pump power was slightly higher than the cascaded OPG threshold for the solid curve (2) in Fig. 4.7(b). Because the QPM grating length of 34 mm in the experiments was longer than the build-up length L_0 of ~12 mm at such a pump power level, cascaded OPG and conventional OPG coexisted. The exponential growth of cascaded OPG is much faster than that of conventional OPG because of the apparent group-velocity-matching between the signal (idler) and the pump. More photons therefore came from cascaded OPG than conventional OPG. The portion of signal photons coming from cascaded OPG was 85%.

In the cascaded OPG with strong pump depletion, not only does the back conversion of SFG coexist with SFG, the back conversion of OPG also coexists with OPG. For the dashed and dotted curves in Fig. 4.7(b), because the back conversion of OPG is becoming stronger with the even higher pump power, both the bandwidth and the pulse length of the cascaded OPG signal increased while the photon conversion efficiency no longer increased. Now more pump photons are converted into signal and idler photons in the front part of the QPM gratings via conventional OPG. We thus obtained the pulse shapes shown by the dashed and dotted curves in which conventional OPG dominates.

4.2.5 Pulse shapes of the signal and the idler from OPG and the optimized grating length for cascaded OPG

In Section 4.2.2 we asserted that we can obtain an accurate pulse shape for the signal by cross-correlation measurements without removing the idler. Here we experimentally verify it by comparing the solid curve in Fig. 4.7(b) to the solid curve on the fifth row (from top) in Fig. 4.5(b), which correspond to the same QPM grating length of 34 mm and the same photon conversion efficiency of ~10%. Although both the signal and the idler were measured in the case of Fig. 4.5(b) while only the signal was measured by the method used in the case of Fig. 4.7(b), the pulse shapes observed for the output were similar, confirming that the presence of the idler does not significantly affect the pulse shapes measured without frequency resolving the cross correlation.

For a detailed comparison, we show the signal and idler pulse shapes in Fig. 4.8, obtained by summing up the frequency-resolved cross-correlation traces for the signal and the idler from a device with a 42-mm-long QPM grating at a pump power level resulting in a photon conversion efficiency of ~20%. The two curves were calibrated for the efficiencies of the sum-frequency generation in the $LiIO_3$ crystal at the signal (idler) wavelengths. The peak positions in the two traces are slightly different because the group velocity of the idler near 1.8 μm is slightly faster than that of the signal near 1.4 μm.

We can deduce the optimized grating length by comparing curves in Fig. 4.8 to those in Fig. 4.7. In contrast to the signal pulses from a 34-mm-long QPM grating shown in Fig. 4.7, the signal and idler pulses in Fig. 4.8 have three peaks. These peaks are at around -1 ps, 4 ps and 6.5 ps for the idler. We obtained this complex pulse shape because the 42-mm-long grating was almost three times longer than the build-up length (~12 mm) of the sum-frequency generation in cascaded OPG. At a lower pump power level we even obtained a square pulse shape [15] because the pulse length of the pump in the cross-correlation was comparable to the time interval between the three peaks, smearing out the cross-correlation. The optimized grating length is therefore ~34 mm to obtain cascaded OPG signals with the best temporal properties.

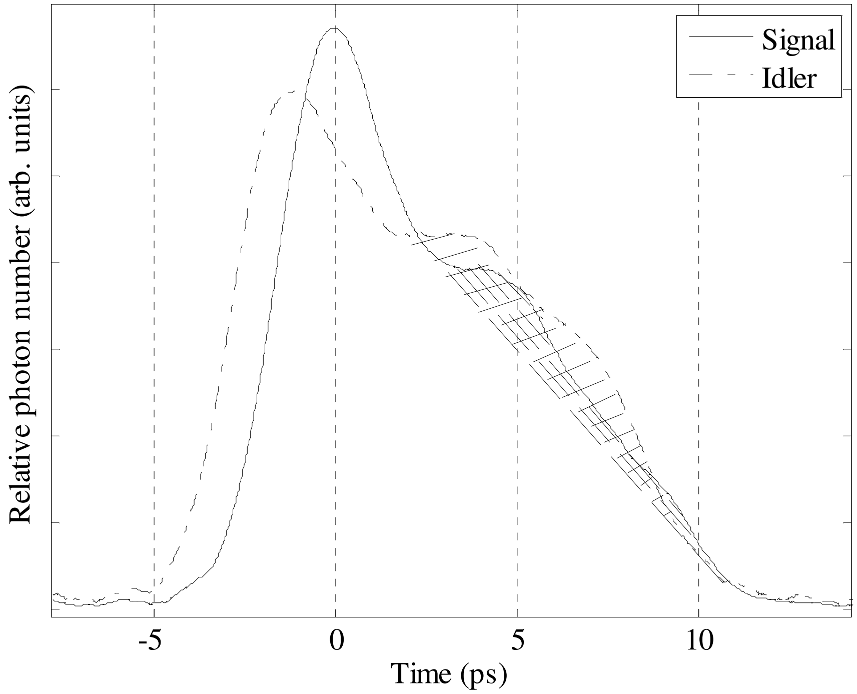

Figure 4.8: The pulse shapes of the signal and idler obtained by summing up the frequency-resolved cross-correlation traces from a 42-mm-long QPM grating at a pump power resulting in a photon conversion efficiency of ~20%. The shadowed regions under the curves correspond to the cascaded OPG products while the other regions correspond to the conventional OPG products.

4.3 Controlled cascaded OPG with engineered QPM gratings

To explore wide-band tuning of the transform-limited signal from cascaded OPG which is distinguishable from a background of conventional OPG signal, we design devices to generate various signal wavelengths from cascaded OPG.

As we discussed at the beginning of this chapter, cascaded OPG is weakly dependent on the pump-wavelength or temperature so that the signal wavelength tuning range is only several nanometers in uniform QPM gratings. Tuning over a broad range of signal wavelengths requires another method for controlling cascaded OPG. Devices with a QPM period Λ_{OPG} for OPG and different QPM periods Λ_{SFG} for sum-frequency generation will allow such control.

Several approaches [3, 4, 30, 36] exist for engineering such multi-component gratings. For this demonstration we chose phase-modulated-gratings because of their loosest fabrication tolerances. In periodically poled lithium niobate, the phase modulation is realized with a poling mask which periodically shifts the center positions of the domains with a period Λ_{ph}, as illustrated in Fig. 4.9(a). The shifting function is designed by numerical optimization to have QPM peaks with desired positions and amplitudes in the Fourier spectrum. [4]

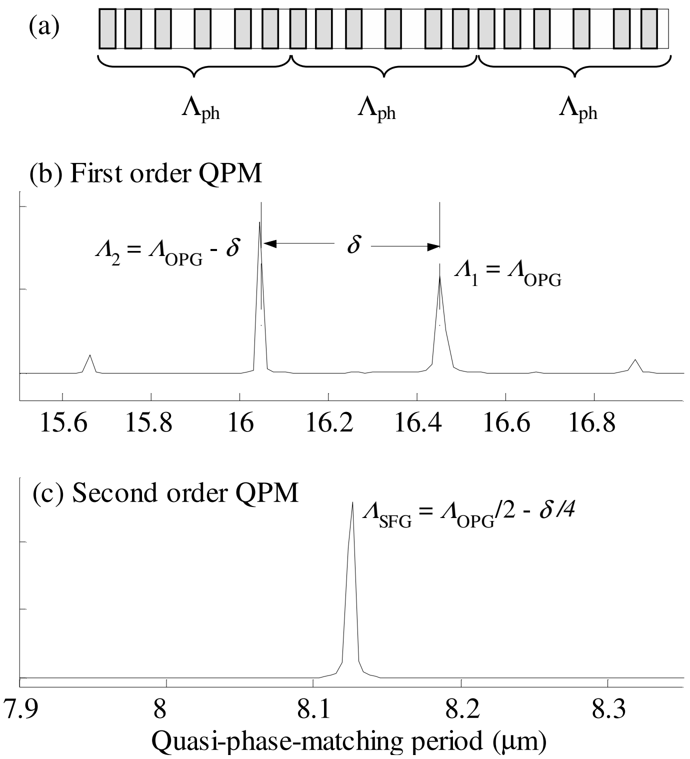

Figure 4.9: (a) A diagram of the phase modulated gratings. The center positions of the domains shift by an amount calculated from an optimized periodic phase function. Λ_{ph} is the phase modulation period. (b)(c) Simulated QPM peaks of phase-reversal gratings designed with $\Lambda_1 = \Lambda_{OPG} = 16.45$ μm, $\delta = 0.4$ μm and $\Lambda_2 = \Lambda_1 - \delta = 16.05$ μm (see text for definition of the symbols). The grating duty cycle is 1/3 and the two peaks near Λ_1 and Λ_2 have the same area in the spatial frequency domain.

To understand the properties of phase-modulated gratings, we study their simplest form, a phase-reversal grating, [3] the simplest phase-modulated-gratings with a QPM period Λ and a 50% duty cycle of phase-reversal. These gratings have two first-order QPM peaks of the same amplitude close to each other in the Fourier spectrum at $\Lambda_1 = \Lambda + \delta / 2$ and $\Lambda_2 = \Lambda - \delta / 2$ where $\delta = 2\Lambda^2/\Lambda_{ph} << \Lambda$. When the domain duty cycle is 50%, there is no second-order peak and only two third-order QPM peaks at $\Lambda_1 /3$ and $\Lambda_2 /3$. When the domain duty cycle is 1/3 there is only one second-order QPM peak at $\Lambda_{SFG} = \Lambda/2$ and no third-order QPM peak, which is shown in Fig. 4.9(b) and (c). If we want different amplitudes for the two first-order QPM peaks at Λ_1 and Λ_2, we can no longer use simple phase-reversal gratings, so we design phase-modulated gratings with the method described in Ref. [4]. The general features of higher order QPM peaks for such phase-modulated gratings are similar to those of the phase-reversal gratings, but offer more degrees of freedom to tailor details of the spatial Fourier spectrum.

For simplicity we prefer phase-modulated-gratings with a domain duty cycle of ~1/3, using the first-order QPM peak at $\Lambda_1 = \Lambda_{OPG}$ for OPG and the strongest second-order QPM peak at $\Lambda_{SFG} = \Lambda/2 = \Lambda_{OPG}/2 - \delta/4$ for sum-frequency generation. In the devices fabricated, $\Lambda_{OPG} = 16.45$ μm and the nominal domain duty cycles are ~40% in the 18-mm-long QPM gratings while δ varies. In order to keep a low OPG threshold, the designed amplitude ratio between the two peaks at Λ_1 and Λ_2 is 7:3 so that the normalized gain parameter η for OPG is nominally 70% of that in a uniform QPM grating. Both in simulations and in second-harmonic generation measurements, the sum of η at the two peaks Λ_1 and Λ_2 is >90% of η in a uniform QPM grating and the peak amplitude ratio is close to the designed value 7:3. For these parameters a series of second and third-order QPM peaks exist while the one at Λ_{SFG} is the strongest.

Figure 4.10 shows that the measured wavelengths of the signal from the strongest cascaded OPG match well with the simulations and vary almost linearly with δ in the signal wavelength range from 1280 nm to 1370 nm. The simulations are based on the waveguide dispersion from a model of reverse-proton-exchange lithium niobate waveguides without any adjustable parameters. [49] Similar to the results from uniform gratings, the signal peaks at these wavelengths had narrow bandwidths (such as 1.5 nm), indicating that near-transform-limit signal pulses were obtained. Although for $\delta \neq 0$ a weak signal from cascaded OPG appeared around 1280 nm which corresponded to the second-strongest second-order QPM peak, we can design more sophisticated QPM gratings to avoid this problem, though these require precise control of the waveguide uniformity and QPM grating duty cycles and await future experiments. [31]

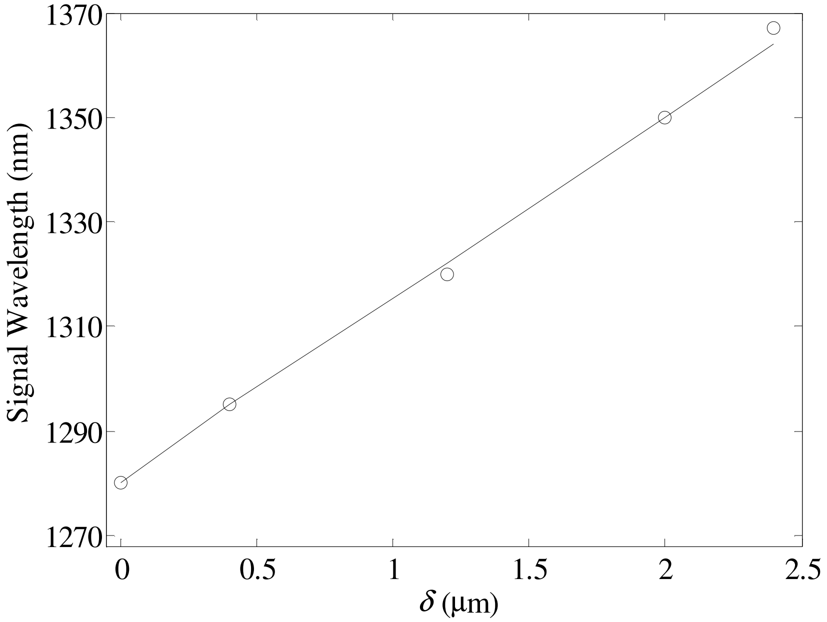

Figure 4.10: The wavelengths of the signal from the strongest cascaded OPG in different phase-modulated-gratings. δ is a parameter describing the QPM grating design, defined in the text and shown in Fig. 4.9. The solid line is from simulations without any adjustable parameter and the circle symbols are from experimental results.

4.4 Summary of Chapter 4 and problems in cascaded OPG

In summary, we experimentally studied cascaded optical parametric generation in RPE waveguides in congruent lithium niobate with uniform QPM grating of various lengths. By using a frequency-resolved cross-correlator, we characterized the temporal properties of the signal generated in cascaded OPG and studied the process in the strong-pump-depletion regime. We also demonstrated control over the signal wavelength from cascaded OPG by using phase-modulated-QPM gratings. By switching between waveguides with different grating designs and fine tuning the pump wavelength or device temperature, obtaining transform-limited and wavelength-tunable signal from cascaded OPG is possible.

Similar to conventional OPG, two problems limit practical applications of cascaded OPG in reverse-proton-exchange congruent lithium niobate waveguides. The most severe problem is photorefractive damage by the green and blue waves generated in the devices, even if we heat the chips to 130 °C. The blue wave comes from parasitic second-harmonic generation of the pump and most of the green wave comes from the sum-frequency generation involved in cascaded OPG. Although the latter is necessary in cascaded OPG and eliminating other parasitic products is difficult, this problem may be solved with new photorefractive-damage-resistant materials. [45, 46, 91] The second problem is the bottleneck in power conversion efficiency. Both cascaded OPG and conventional OPG using ultra-short pulses have a bottleneck in conversion efficiency because only part of the leading edge of the pump pulse participates in the nonlinear interactions. Further improvement requires more sophisticated QPM gratings engineered for cascaded OPG and may require new techniques.

Such an alternative to cascaded OPG to improve the temporal properties of the OPG products is to compensate for the group velocity mismatch between the signal (idler) and the pump with periodic waveguide structures. [8] Simulations and experimental results show that the signal generated in such a device also have well-controlled temporal properties, which is discussed in Chapter 5.

CHAPTER 5: APPLICATION OF QUASI-GROUP-VELOCITY-MATCHING IN OPTICAL PARAMETRIC GENERATION IN REVERSE-PROTON-EXCHANGE WAVEGUIDES

The temporal properties of the output have long been a limiting factor for the application of optical parametric generation. In Chapter 4 we demonstrated controllable temporal properties at desired wavelengths with cascaded OPG in lithium niobate waveguides. The control of temporal properties can also be achieved by directly manipulating the effective group velocities of the interacting waves. [15, 70, 71] Group-velocity-matching in nonlinear interactions has been frequently studied in recent years. In bulk materials used for $\chi^{(2)}$ nonlinear interactions it was realized by using different polarizations or tilting the wave fronts. [70, 71] Such approaches are prohibited in reverse-proton-exchange waveguides on z-cut lithium niobate wafers because only TM modes are guided and the wave fronts in waveguides cannot be tilted. In this chapter we report the application of an alternative approach, quasi-group-velocity-matching (QGVM), [8] for OPG in reverse-proton-exchange lithium niobate waveguides.

With 1.6-ps-long pump pulses near 785.1 nm we have obtained near degenerate output pulses with a time-bandwidth product as low as 1.1 from a device with QGVM. Compared to a much larger time-bandwidth product of 10.5 for near degenerate OPG in a device without QGVM, the temporal properties of OPG pulses are significantly improved.

In this chapter we first discuss the technique to fabricate tight bends that are required in the QGVM devices. We then describe the design of quasi-group-velocity-matching devices and demonstrate OPG with such designs.

5.1 Enabling technique: tight bends in RPE waveguides

Although a small bend radius is desired in PPLN waveguides to enhance device integration, it is limited by rapidly increasing radiation losses with decreasing bend radius. In Ti or Ni diffused lithium niobate waveguides techniques such as MgO in-diffusion reduced the acceptable bend radius to 5 mm. [97] However, for annealed- or reverse-proton-exchange waveguides the smallest bend radius with negligible bend losses is already 4 mm and MgO in-diffusion will not help further.

Based on the theory in Section 2.6.1, we experimentally tested two different approaches to reduce the bend radius: 1) increasing the index difference in the waveguide by deeper proton-exchange, and 2) adding air trenches beside the waveguides by wet etching after proton-exchange. We choose the former for the QGVM experiments because the fabrication procedure is simpler and the overall loss is lower.

5.1.1 Tight bends fabricated by a RPE process with a deeper proton-exchange depth

To avoid bend loss, the smallest bend radius R is 4 mm for s-bends in a typical reverse-proton-exchange waveguide, [49] for which the proton-exchange depth is 1.84 μm, the annealing time is 23 hrs at 310 °C and the time of reverse-proton-exchange is 25 hrs at 300.5 °C. We are able to reduce R to 1 mm without introducing extra bend loss by increasing the proton-exchange depth to 2.39 μm. Correspondingly the noncritical waveguide width [53] becomes 6.5 μm.

By increasing the proton-exchange depth, we not only increase the effective refractive index of the waveguide modes, but also shrink the mode size in the dimension of the waveguide width. From Eq. (2.36) the minimum bend radius thereby is much smaller than that for devices fabricated with the conventional RPE process.

One difference in the waveguide design for the new process is that the coupling loss between straight waveguides and bends must be considered for a small bend radius. For a joint between a straight waveguide and a bend with R = 1 mm, the necessary shift to optimize the mode coupling is ~1 μm, which is close to an estimation using the eigenmode size, the wavelength, the bend radius, and the method described in Section 2.6.1. When this shift is included in the waveguide design the bend loss for a cosine-type s-bend with a minimum bend radius of 1 mm is negligible. Such a tight s-bend is one of the key components in QGVM devices.

The price of a higher proton-exchange dose is a higher propagation loss in straight waveguides, <0.25 dB/cm for waves near 1570 nm (compared to that of <0.15 dB/cm with the conventional process) and <0.5 dB/cm for waves near 785 nm. This higher propagation loss is mainly scattering loss caused by the larger quantity of defects in the waveguides with a higher proton dose.

The proton-exchange depth in the new fabrication process is optimized for a balance between the smaller bend loss and the higher propagation loss in 6.5-μm-wide straight RPE waveguides. To find the optimal depth, we measured losses and SHG efficiency for devices with different proton-exchange depths. For a proton-exchange depth <2.39 μm the minimum bend radius with negligible bend loss is >1 mm. For a proton-exchange depth a little higher than 2.39 μm, the propagation loss for the pump wave is more than twice that of the signal and the idler because the scattering loss is higher at the pump wavelength than at the signal/idler wavelengths. We therefore selected a proton-exchange depth of 2.39 μm, for which the propagation loss of the pump is about twice that of the signal and idler, which is similar to waveguides fabricated with the conventional process.

The smallest bend radius for circular bends with negligible bend loss is larger than that for s-bends [7] and we experimentally determined it to be ~2 mm for RPE waveguides fabricated with the new fabrication process. U-turns with such a small bend radius can be fabricated on chips and is been used in applications such as OTDM on a lithium niobate chip. [7]

5.1.2 Tight bends fabricated by adding air trenches along the outside edge

As shown in Fig. 5.1, low-loss tight s-bends in RPE lithium niobate waveguides can be fabricated by simultaneously creating air trenches along the outside edge of the bends and shifting the waveguides at the joints between the straight and curved waveguides. [98]

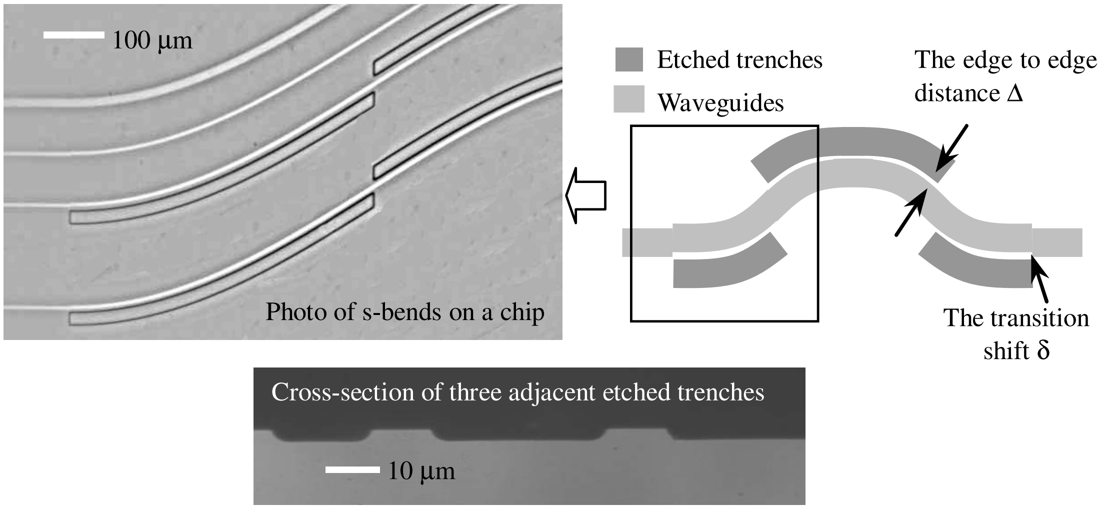
100 μm
Photo of s-bends on a chip
Etched trenches
Waveguides
The edge to edge distance Δ
The transition shift δ
Cross-section of three adjacent etched trenches
10 μm

Figure 5.1: Diagram for the air trenched s-bends and a photo of s-bends on a chip. In the photo of s-bends, the white stripes are the waveguide openings on the SiO_2 mask and the curved dark stripes with black edges are the etched trenches. The photo on the bottom is the cross section of three adjacent etched trenches on a witness sample under microscope.

Air trenches along the outside edge of the bends can reduce the radiation loss [98] because the index difference is increased and the mode coupling between guided modes and radiation modes is effectively reduced. By using the effective index method described in Section 2.6.1, we conclude that a deeper trench and a shorter distance between the trenches and the waveguides will result in a smaller bend radius. A trench depth on the order of the eigenmode size (typically 3 μm) limits the bend radius to ~1.5 mm in simulations. For this bend radius the necessary transition shift to optimize the mode coupling is ~1.1 μm in theory.

Air trenches are fabricated by wet-etching of the proton-exchange regions on the +*z* face of the z-cut lithium niobate wafers based on the differential hydrofluoric acid (HF) etching rate of lithium niobate, i.e. that the HF etching rate for the –*z* face or the proton-exchanged regions is >1000 times faster than for the +*z* face. [99] As a first step in the fabrication procedure, blank lithium-niobate wafers are carefully cleaned and covered with a layer of SiO_2 on the +*z* face by sputtering. Then lithography is done on the SiO_2 layer to define the trench patterns. Having done proton exchange in benzoic acid and obtained an exchange depth being equal to the desired trench depth, we put the wafer into violently stirred 50% HF solution at room temperature for >10 hrs to completely etch away the proton exchanged regions and obtain smooth trench walls. Then we flat polish the -*z* face and clean the wafer to ensure good poling quality in the following fabrication procedures. After that we follow the typical procedure in Fig. 1.7 to create reverse-proton-exchange waveguides. [2] Before the step of >10 hrs HF etching, it is essential that we avoid creating defects outside the trench regions, otherwise the waveguide loss will increase substantially.

Table 5.1: The lowest loss measured for s-bends with air trenches and transition shifts

Minimum Bend Radius	4 mm	3 mm	2 mm	1.5 mm	1 mm
Bend length (mm)	13	10.3	7.4	6	4.4
Bend loss (dB)	0	0.3	1.1	1.5	6.3

In experiments we fabricated 8-μm-wide waveguides with 2.7-μm-deep trenches beside s-bends. After etching, the distances between the trenches and the waveguides vary from 0.5 μm to 10.5 μm. The designed shifts at the joints vary from 0 to 2 μm. To explore bend losses in QGVM designs, the lengths of the bends are chosen to exactly compensate for the group velocity mismatch between 780 nm and 1550 nm waves after they both pass an 8-mm-long straight waveguide. We estimate the bend loss from the throughput ratio for 1550-nm waves in the straight vs. the bent waveguide. For different minimum bend radii, the lowest losses are listed in Table 5.1. S-bends with a minimum bend radius of 4 mm are used as the base because their throughputs are close to those of the straight waveguides, indicating negligible bend loss. The bend loss increases exponentially when the minimum bend radius decreases from 3 mm to 1 mm.

Details of the measurements for s-bends with a minimum bend radius of 1.5 mm are shown in Fig. 5.2. The bend loss improves by 8 dB compared to the devices without trenches and shifts at the joints of different curvatures. The curves show that a shorter distance between the trenches and the waveguides is preferable and the transition loss can be greatly improved by shifting the waveguides at the joints, with an optimal shift value > 1 μm.

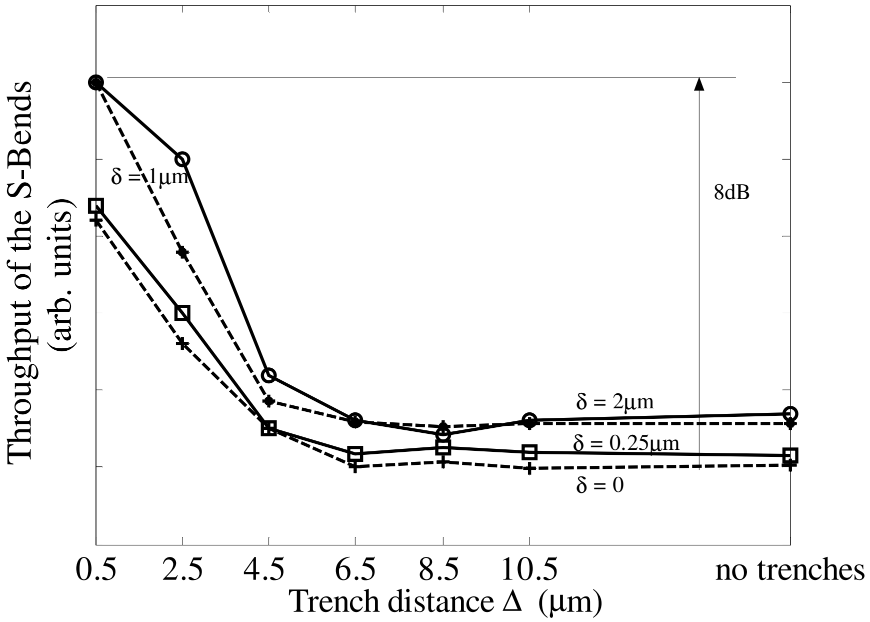

Figure 5.2: The throughput of the s-bends with different distances Δ between the trench and the waveguides and different transition shifts δ at the joints which are defined in Fig. 5.1. The minimum bend radius in the s-bends is 1.5 mm.

Besides s-bends, we also fabricated circular bends. With a bend radius of 2.5 mm, a trench depth of 2.7 μm, about 1-μm distance Δ between the trenches and the waveguides and 2-μm shifts δ at the joints, the 180° circular bends have a bend loss of 1.5 dB. The main loss in these devices may have come from the scattering loss caused by the roughness on the trench walls.

We may further improve the devices by optimizing the waveguide widths on both sides of the joints between straight waveguides and bends to obtain a higher mode coupling efficiency. [100]

This approach of adding air trenches is limited by the roughness of the trench walls with current wet-etching method, which causes ~1 dB/cm propagation loss for 1550-nm band waves. An alternative is to use the method of dicing plus polishing [45, 46] which may create smoother trench walls and result in a lower propagation loss.

5.2 Quasi-group-velocity-matching device design

With the design and the fabrication procedure of low-loss tight-radius bends available we are able to design quasi-group-velocity-matching devices.

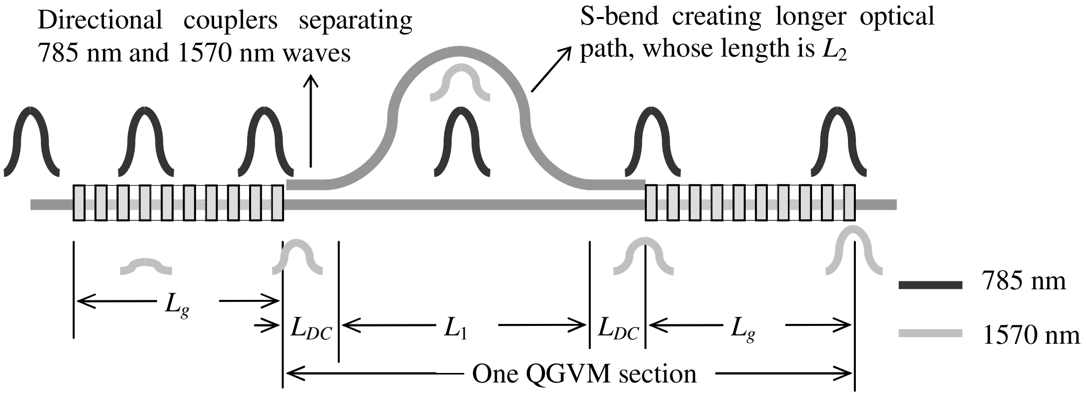
Directional couplers separating 785 nm and 1570 nm waves
S-bend creating longer optical path, whose length is L_2
L_g
L_{DC}
L_1
L_{DC}
L_g
One QGVM section
785 nm
1570 nm

Figure 5.3: Diagram of near-degenerate optical parametric generation using waveguides with one quasi-group-velocity-matching section, designed for a pump wave near 785 nm and signal and idler waves near 1570 nm. L_g is the length of each section of QPM gratings, L_{DC} is the length of each directional coupler and L_1 is the length of the straight waveguide between the two directional couplers.

The QGVM scheme shown in Fig. 5.3 is similar to that used for second-harmonic generation. [8] The length L_g of each QPM grating is ~4.8 mm, approximately the group-velocity-walkoff length between 1.6-ps-long pulses at 785 nm and 1570 nm. The length L_{DC} of each directional coupler is ~1 mm, designed to couple the 1570-nm waves into an adjacent waveguide while keeping the 785-nm waves in the straight path. The two directional couplers are connected with a straight waveguide (length is L_1) and a bend arm composed of two s-bends (total length is L_2) so that the signal and the idler (with a faster group velocity than the pump) will propagate through a longer optical path than the pump. To ensure that the pulse envelopes of the pump and signal (idler) efficiently overlap in every QPM grating the optimal design must satisfy:

$$L_2 - L_1 = (n_g^p / n_g^{s,i} - 1)(rL_g + L_1 + 2L_{DC}) \tag{5.1}$$

Here n_g^j ($j = p$, s, i respectively corresponds to the pump, signal and idler) is the group index in straight waveguides. Near degeneracy the same QGVM design works for both the signal and the idler because $n_g^s \approx n_g^i$ and the typical bandwidth of the directional couplers is >100 nm. The ratio r is a noncritical adjustable parameter with an optimal value slightly > 1 since the group index in the s-bends is slightly smaller than that in straight waveguides.

The bend arm in a QGVM section is composed of two cosine-type s-bends. The length L' of each s-bend is:

$$L' = \frac{2L}{\pi} E(-a^2), \quad a = \frac{\pi A}{2L} \tag{5.2}$$

Here A is the height and $L = L_1/2$ is the length of a cosine-type s-bend described by Eq. (2.35), whose minimum radius of curvature is $R = 2L^2/(\pi^2 A)$. Function $E(x)$ is the complete elliptic integral of the second kind for x. [58] We can combine Eq. (5.1) and Eq. (5.2) to solve A and L for desired designs.

In order to have more QGVM sections within a limited device length we prefer shorter L_1; the approximate length is proportional to the minimum bend radius R in the s-bends. To avoid bend loss, the smallest R is 4 mm in typical RPE waveguides fabricated with our conventional process and 1 mm in the new process where the proton-exchange depth is increased to 2.39 μm, as described in Section 5.1.1. Using $L_g \sim 4.8$ mm, $L_{DC} \sim 1$ mm, $r = 1$, and group indices estimated from SHG measurements, the typical length of L_1 is 13.7 mm with the conventional process and 4.5 mm with the new process. With the latter we are able to design devices with four QGVM sections on a 60-mm-long chip.

We design devices with both the conventional process and the new process described in Section 5.1.1 to check the effects of multiple QGVM sections and the propagation losses on the gain and temporal properties of the OPG output. The device structures are similar for the two fabrication processes. The pump wave near 785 nm in the free-space TEM_{00} mode is converted into almost pure TM_{00} waveguide mode at the beginning of the device by a single-mode filter, followed by QPM gratings and QGVM sections as shown in Fig. 5.3.

The waveguide widths and the mode filters are optimized. For the conventional process, the waveguide width is 1.5 μm in the mode filter and 8 μm otherwise. For the new process, the mode filter is a 1.5-μm-wide segmented waveguide with a duty cycle of 20% [50] and the waveguide width is 6.5 μm in other regions.

If not otherwise specified the chips are heated to 130 °C in the experiments to avoid photorefractive damage. The basic experimental setup is the same as that in Fig. 3.4.

5.3 Experimental results of OPG with QGVM

For 1.6-ps-long pump pulses near 785 nm the OPG threshold of the devices with four QGVM sections is 100 pJ. This is half the 200 pJ threshold in a conventional device with a continuous 25-mm-long QPM grating (the same as those in Chapter 3) and is a consequence of the more effective interaction of the pump and signal (idler) pulses with matched group velocities.

At a pump power level slightly above the OPG threshold when pump depletion is negligible, we measured the auto-correlation traces of the signal (idler) pulses using two-photon-absorption in a silicon photodiode [101] and recorded the power spectrum with an optical spectrum analyzer. The pump wavelength is 785.1 nm and the signal and the idler waves are near degeneracy.

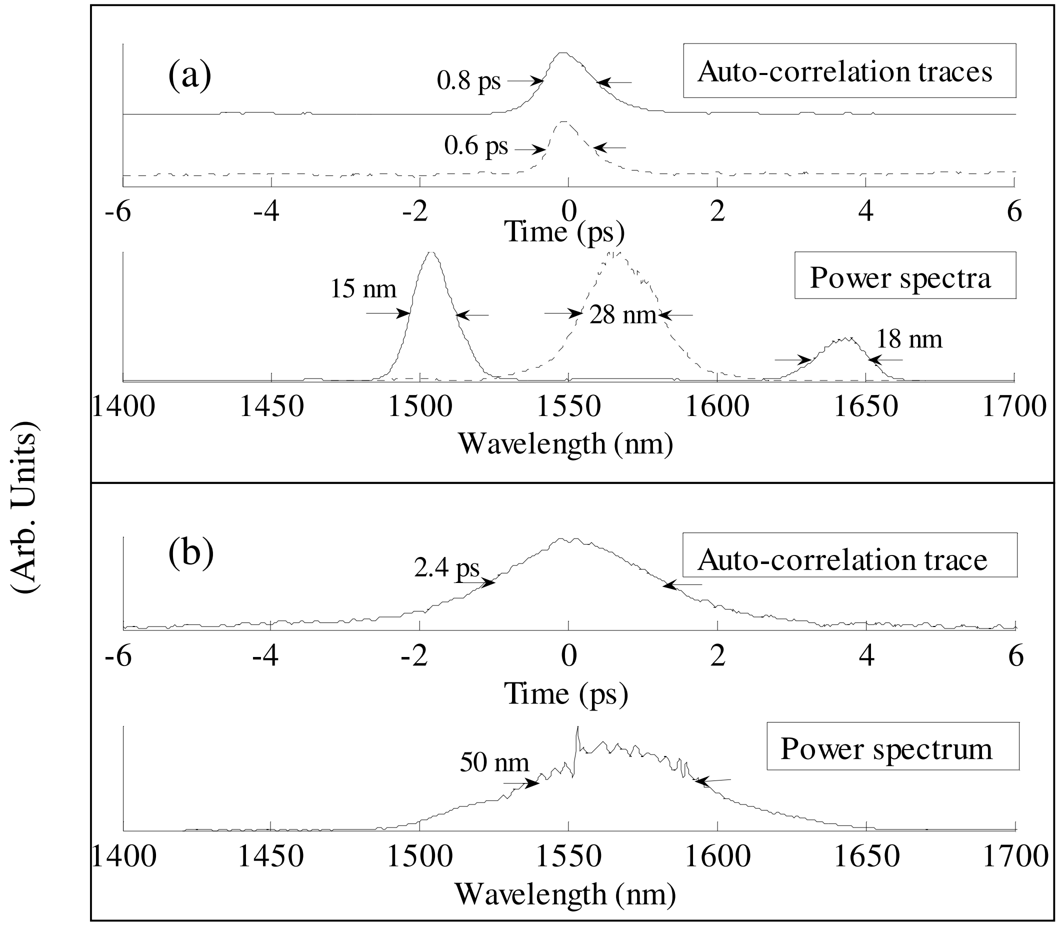

Figure 5.4: (a) Auto-correlation traces and power spectra of the output from a device with four QGVM sections; (b) those from a conventional device without QGVM. The solid curves correspond to a device temperature of 130 °C while the dotted curves correspond to a device temperature of 121.3 °C. The pump wavelength is 785.1 nm for all. The total length of QPM gratings is 24 mm in both cases. The pulse lengths and bandwidths in the figures are FWHM.

The solid curves in Fig. 5.4(a) show the results from a device with four QGVM sections at 130 °C. The bandwidth of the signal (idler) near 1503 (1645) nm is 15 (18) nm, the pulse length is 0.56 ps assuming a Gaussian pulse shape, and the time-bandwidth products are 1.1 for both the signal and the idler. The dotted curves show the output from the same device at 121.3 °C with the signal and idler merging at 1570 nm. The pulse length is 0.44 ps, the bandwidth is 28 nm, and the time-bandwidth product is 1.5.

As a comparison, Figure 5.4(b) shows the results from a conventional device without QGVM, that the bandwidth is >50 nm, the pulse length is 1.7 ps and the time-bandwidth product is 10.5. The total QPM grating lengths in both cases are 24 mm. The OPG output from a device with four QGVM sections thus is much closer to the transform limit than that from a conventional device.

In the experiments we vary the device temperature T and the pump wavelength λ_p, establishing that for the same device with QGVM the pulse length is a weak function of T and λ_p while the bandwidth is a strong function of them.

Figure 5.5 shows the power spectra for a device with the simplest QGVM design, which has only one QGVM section and is fabricated with the conventional process. T is fixed at 130 °C for curves in Fig. 5.5(a). λ_p is fixed at 781.2 nm for curves in Fig. 5.5(b) and their baselines indicate the various device temperatures which can be read from the vertical axis. Due to a filter effect coming from the carrier phase mismatch generated in the QGVM section the power spectrum changes significantly when λ_p varies by 0.3 nm or T varies by 2 °C. This filter effect notably contributes to the improvement in temporal properties of the OPG output.

While the experimental results are consistent with numerical simulations, a more insightful explanation of this filter effect comes from the analytical solutions to optical parametric amplification with CW waves. For CW OPA we can drop the terms corresponding to the group velocities in Eq. (2.7) and obtain analytical solutions like Eq. (2.9) when pump depletion is negligible.

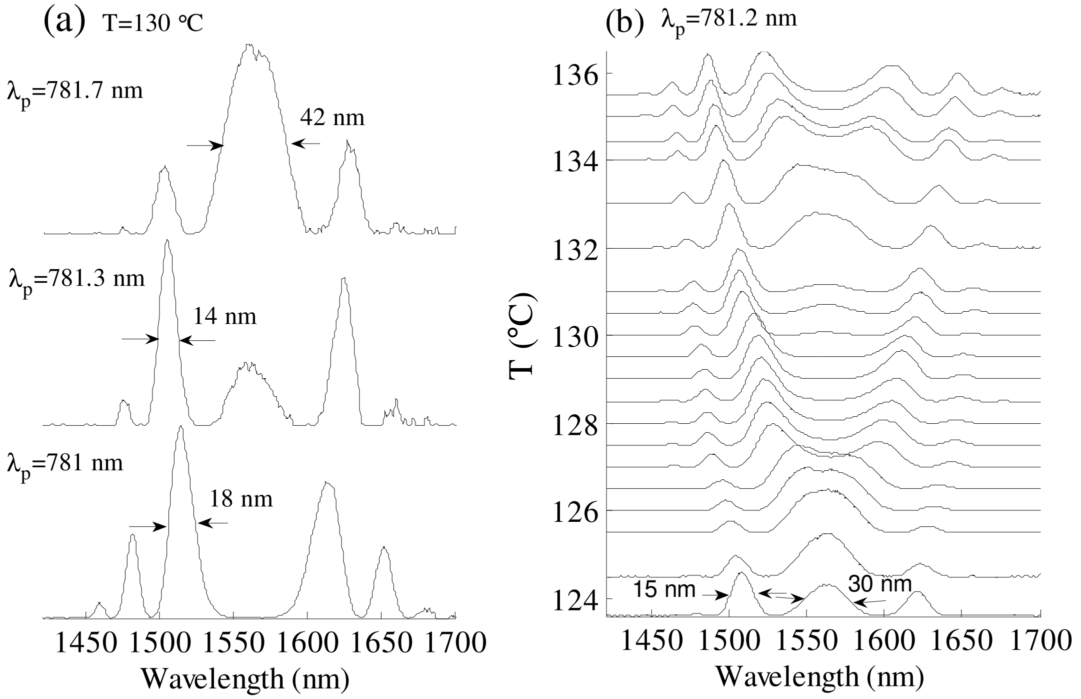

Figure 5.5: The power spectra of the output from a waveguide with one QGVM section. The total length of QPM gratings is 9.6 mm. The device temperature T is fixed at 130 °C in (a). The pump wavelength λ_p is fixed at 781.2 nm in (b). The baselines of the curves in (b) indicate the device temperature, which can be read from the vertical axis. All the traces are normalized to their maxima. The bandwidths shown in the figures are FWHM.

Suppose the phase mismatch between the three interacting waves is $\phi = \phi(\lambda_{s,i}) = 2\pi[n(\lambda_p)L_1/\lambda_p - n(\lambda_s)L_2/\lambda_s - n(\lambda_i)L_2/\lambda_i]$ at the beginning of the second QPM section, originating from the two different paths in a QGVM section. λ_j (j = p, s, i) is the wavelength and $n(\lambda_j)$ is the average refractive index over the corresponding waveguide length. With negligible pump depletion for OPA in a uniform QPM grating in a straight waveguide, the output signal photon flux is:

$$\begin{aligned} N_s = {} & N_{s0}\{\cosh^2\Gamma'' L_g + [\Delta k/(2\Gamma'')]^2 \sinh^2\Gamma'' L_g\} + N_{i0}(\Gamma'/\Gamma'')^2 \sinh^2\Gamma'' L_g + \\ & 2(\Gamma'/\Gamma'')\sinh\Gamma'' L_g \sqrt{N_{s0}N_{i0}}\{\cosh\Gamma'' L_g \cos\phi + [\Delta k/(2\Gamma'')]\sinh\Gamma'' L_g \sin\phi\} \\ \Gamma'' = {} & \sqrt{\Gamma'^2 - \Delta k^2/4}, \qquad \Delta k = k_p - k_s - k_i - 2\pi/\Lambda \end{aligned}$$

(5.3)

N_{s0} (N_{i0}) is the input photon flux of the signal (idler), L_g is the length of the QPM grating, Γ is the parametric gain coefficient for $\Delta k = 0$, k_j ($j = p, s, i$) is the wave vector, and Λ is the QPM grating period. For OPA $\Gamma >> \Delta k/2$ and α is real.

This solution can be simplified to $N_s \approx 4N_{s0}\sinh^2 \Gamma L_g \cos^2(\phi/2)$ in the high gain regime if $\Delta k \approx 0$ and $N_{s0} = N_{i0}$, which are satisfied in the QPM gratings for OPG with the QGVM scheme. Each QGVM section thus is equivalent to a combination of an amplifier with exponential gain and a frequency filter determined by the carrier phase mismatch. Because $\phi(\lambda_{s,i})$ vary by several π within the > 150 nm bandwidth for near-degenerate OPA with L_g ~ 4.8 mm, the signal power spectrum has several peaks and valleys and their positions vary when $\phi(\lambda_{s,i})$ changes with T and λ_p, as shown in Fig. 5.5.

By comparing the results shown in Fig. 5.4 and Fig. 5.5 we can deduce the effects of multiple QGVM sections. Side peaks are significant in the spectra in Fig. 5.5 when the device has only one QGVM section, but are negligible in Fig. 5.4(b) when the device has four QGVM sections. The reason is that each extra QGVM section is an extra frequency filter and the main peak is thus selected out. However the bandwidth of the main peak only varies slightly, possibly because each QGVM section randomly introduces a different phase-mismatch function $\phi(\lambda_{s,i})$ and the overall effect is not optimal. More detailed studies need precise control of the carrier phases in each QGVM section, which may be realized in the future by using electro-optical phase shifters.[102]

We also measure and simulate different devices to explore the consequences of the propagation losses. The propagation loss of the pump does not affect the frequency response but does reduce the parametric gain in the QPM gratings near the end of the device and prevents us from obtaining an even lower OPG threshold. The propagation loss of the signal and idler only reduces the photon conversion efficiency.

5.4 Summary of Chapter 5

With quasi-group-velocity-matching structures in reverse-proton-exchange lithium niobate waveguides we demonstrated an OPG threshold of 100 pJ, half of that in conventional devices described in Chapter 3. We obtained a time-bandwidth product as low as 1.1 for OPG outputs near degeneracy, compared to >10 in conventional single-grating devices

Different from cascaded OPG in Chapter 4, here waveguide structures instead of QPM gratings are engineered to change the apparent group velocities of the interacting waves. Although the improved time-bandwidth products shown in this chapter are larger than those in Chapter 4, they are for signal wavelengths near degeneracy instead of far away from degeneracy. Considering the scalability of QGVM structures, quasi-group-velocity-matching is an effective approach to improving the temporal properties of the OPG output and may find its place in applications based on OPG or optical parametric fluorescence, such as photon pair generation. [9]

Since the number of QGVM structures is important and more sections of QGVM means a longer waveguide, further improvements to the temporal properties of the OPG output would require a lower propagation loss in the waveguides.

The QGVM structure is not limited to RPE waveguides and we may implement it in other types of waveguides such as ridge waveguides or Ti- or Ni-diffused waveguides.

CHAPTER 6: TWO-MODE OPTICAL PARAMETRIC AMPLIFICATION USING ASYMMETRIC Y-JUNCTIONS

Optical parametric amplifiers are important sources for tunable ultra-short infrared pulses and are also useful photon sources. [1, 9] Channel waveguides can be used to enhance the intensities of the interacting waves over long interaction lengths, lowering the required pump power. One of the most efficient waveguides in lithium niobate reported to date is based on reverse-proton-exchange which we described in Section 1.3. [2] However, separating the photons of different wavelengths generated in these waveguides is difficult, especially near degeneracy. Inside the waveguides all the waves are propagating in the same direction and cannot be separated by angular selection. Outside the waveguides prisms or filters work only for wavelengths away from degeneracy and are difficult to integrate; polarization techniques fail because only TM modes are guided. In this chapter we demonstrate that mode demultiplexing with asymmetric Y-junctions is a good approach to separate the signal from the idler for parametric amplifications in annealed- or reverse-proton-exchange lithium niobate waveguides, which we test conveniently with optical parametric generation (vacuum noise amplified with ~10^{10} gain).

Demultiplexing with asymmetric Y-junctions involves higher order modes besides the TM_{00} waveguide mode. Integrated optical devices using higher order modes have many useful functions, including mode multiplexing in periodically poled lithium niobate optical frequency mixers, [8] cascaded semiconductor all-optical switches, [103] and silica-based waveguide arrays. [104] For these devices, low crosstalk is the key to good performance. Two main types of mode multiplexing are asymmetric Y-junctions [52, 105, 106] and MMI devices. [74] Asymmetric Y-junctions have been studied since the early days of integrated optics. Due to their adiabatic property asymmetric Y-junctions have advantages over MMI devices, including wide bandwidth, low excess loss, and simple configuration. In step-index waveguides, MMI devices are easier to fabricate than Y-junctions with sharp vertices. [107, 108] On the other hand, in diffused waveguides such as annealed- or reverse-proton-exchange PPLN waveguides asymmetric Y-junctions are relatively easier to fabricate because the refractive-index profiles are smooth in such waveguides. [47, 49]

This chapter is organized as following. In Section 6.1 we explore asymmetric Y-junctions with their shapes optimized using the theory in Section 2.6.3. Then in Section 6.2 we describe the design parameters of asymmetric Y-junctions used in the OPG experiments. After that we discuss the threshold, mode demultiplexing and tuning curve measurements for OPG involving TM_{10} modes in Section 6.3.

6.1 Experiments on the shape optimization of asymmetric Y-junctions

We design and fabricate asymmetric Y-junctions for 1550-nm waves in annealed- or reverse-proton-exchange waveguides to explore the effects of shape optimization, which is studied by comparing the mode multiplexing performance of the conventional and the optimal devices side-by-side on the same chip.

We characterize the mode multiplexing in PPLN waveguides using the nonlinear mode-mixing method, [5] where the amplitudes of different nonlinear interaction peaks in the SHG tuning curve are used to calculate the mode content out of a Y-junction. If we launch the first-harmonic wave for SHG into one arm of a Y-junction, the output first-harmonic wave will contain mode components including the TM_{00} mode and the TM_{10} mode. The SHG tuning curve will have several peaks at the second-harmonic frequencies corresponding to the TM_{00}, TM_{10} and TM_{20} waves, etc. The amplitudes of the peaks are determined by the mode contents in the first-harmonic wave and the efficiencies of the nonlinear interactions involved. In other words with known empirical or simulated nonlinear efficiencies we can deduce the mode contents by identifying the peak amplitude ratios on a SHG tuning curve. This method was described in detail in Ref. [5] and was successfully used to measure mode contrast ratios over 30 dB.

Annealed- or reverse-proton-exchange waveguides are respectively chosen to experimentally demonstrate the two different approaches in shape optimization described in Section 2.6.3, the shifting approach and the stretching approach. In this section w_a, w_b and θ have the same definition as in Fig. 2.7.

For the "shifting" approach we use annealed-proton-exchange waveguides [47] with $w_a = 5$ µm and $w_b = 4$ µm. These waveguides have a proton-exchange depth of 1.3 µm and are annealed at 330 °C for 26 hrs. For a conventional Y-junction and an optimized Y-junction designed for 1550 nm waves with the same branching angle $\theta = 0.0072$, the measured mode contrasts from multiplexing are listed in Table 6.1. P_0, P_1, and P_2 are the powers in the lowest three modes for the 1550-nm-band waves past the Y-junctions. "Wide (narrow) arm" means the SHG tuning curves are obtained with the pump wave launched from the wide (narrow) arm of the asymmetric Y-junction at the beginning of the waveguide.

Table 6.1: The mode contrast comparison between the conventional design and the design optimized by the "shifting" approach for asymmetric Y-junctions in \annealed-proton-exchange waveguides.

	Wide arm	Narrow arm	
	P_1/P_0 (dB)	P_0/P_1 (dB)	P_2/P_1 (dB)
Conventional	-12.0	-12.3	< -17.8
Optimal	-16.5	-15.7	-11.8
Improvement	4.5	3.4	<-6

Compared to the conventional design, the optimized design better suppresses the crosstalk between the first and second modes by >3.4 dB, but increases the crosstalk between the second and third modes by >6 dB. Fabrication errors limit the mode contrasts and cause the difference between the measured P_1/P_0 and P_0/P_1. Devices with a smaller branching angle and >20 dB contrast in the conventional design show less improvement with the optimization because the mode coupling caused by fabrication errors dominates over that due to the nominal design. However the tendencies match the theory in Section 2.6.3.

Reverse-proton-exchange waveguides are used to test the "stretching" approach. The proton-exchange depth is 1.85 μm, the annealing time is 23 hrs at 310 °C and the reverse-exchange time is 22.5 hrs at 300.5 °C. We choose $w_a = 5$ μm and $w_b = 3$ μm or $w_a = 4.5$ μm and $w_b = 3.5$ μm for comparison. In the design the function $f(z)$ defined in Section 2.6.3 is

$$f(z) = \begin{cases} z_0 - (z - z_0)^2 / z_0, & 0 \le z \le z_0 \\ z_0 + (z - z_0)^2 / (1 - z_0), & z_0 < z \le 1 \end{cases} \tag{6.1}$$

which is a "quadratic stretching" around z_0 where the coupling coefficient $\kappa_{01}(z)$ is maximal. In this type of shape optimization z_0 is the only critical parameter. From the waveguide models we estimate that the maximum of $\kappa_{01}(z)$ is reached at $z_0 = 0.1375$ for a 2-mm-long Y-junction with $\theta = 0.016$. We design devices with z_0 in the range between 0.1 and 0.15 to accommodate simulation and fabrication errors.

Comparing the optimized designs to a conventional Y-junction with the same branching angle, we observe 10 dB better performance in mode multiplexing in short devices ($\theta = 0.016$) and 3 dB worse performance in long devices ($\theta = 0.008$), which follows the tendency we expect from the theory in Section 2.6.3. For the designs with different w_a and w_b, the nominal optimal ones with $w_a = 5$ μm and $w_b = 3$ μm show 3 dB less improvement than the non-optimal ones with $w_a = 4.5$ μm and $w_b = 3.5$ μm because the fabrication errors again dominated over that due to the nominal design.

According to the above experimental results for the two different shape optimization approaches, designing the shape of the asymmetric Y-junctions properly can improve their performance in mode multiplexing. However, the performances are limited by fabrication errors and a more precise waveguide model is also necessary for better designs. For this reason, conventional designs are used in the OPG experiments in the following sections.

6.2 Waveguide structure and asymmetric Y-junctions for the OPG experiments

Mode demultiplexing with asymmetric Y-junctions is based on the adiabatic variation of the refractive index distribution along the device. Depending on from which end the waves are launched, within a wavelength range asymmetric Y-junctions are efficient mode multiplexers or demultiplexers. [5, 109] For waves near 1550 nm, a power contrast >30 dB between the TM_{00} and TM10 modes has been demonstrated. [5] To realize mode demultiplexing in OPG, we use an asymmetric Y-junction as a mode multiplexer for the pump and as a mode demultiplexer for the signal and the idler.

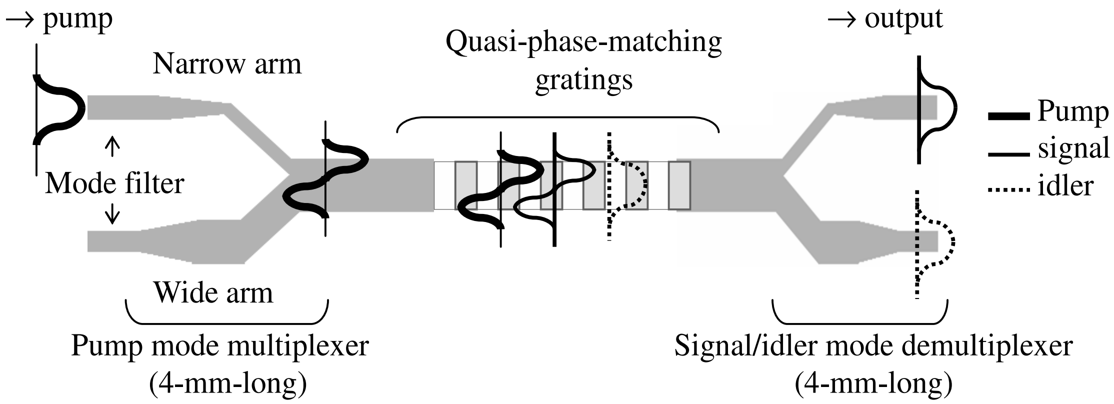
→ pump
Narrow arm
Mode filter
Wide arm
Pump mode multiplexer (4-mm-long)
Quasi-phase-matching gratings
→ output
Pump
signal
idler
Signal/idler mode demultiplexer (4-mm-long)

Figure 6.1: Typical device for OPG with two waveguide modes.

Figure 6.1 shows the design of such a device and illustrates how the modes of the interacting waves evolve along it. On the input side, the TEM_{00} pump beam launched into the narrow arm of the mode multiplexer is converted into the TM_{10} waveguide mode.

Then the pump propagates through the quasi-phase-matching region and generates signal and idler in two waveguide modes (the TM_{10} mode and the TM_{00} mode). [5, 51] On the output side, the signal and idler waves in different modes will emerge from the two different arms of the mode demultiplexer. The widths of the two arms of the asymmetric Y-junctions are 2 μm / 3 μm on the input side and 3 μm / 5 μm on the output side, respectively, designed for the pump near 780 nm and the signal (idler) near 1560 nm to obtain the best mode multiplexing/demultiplexing contrast between the also TM_{00} and TM_{10} modes.[18]

In the OPG experiments the chips are heated up to 130 °C. The quasi-phase-matching periods of the gratings are 16.45 μm. The devices are fabricated with our typical procedure described in Section 1.3. [49] The FWHM of the pump pulses is 1.8 ps. For different purposes we choose various waveguide widths from 8 μm to 14 μm in the interaction region and design devices with or without the mode demultiplexer for the signal and the idler. The basic experimental setup is the same as that in Fig. 3.4.

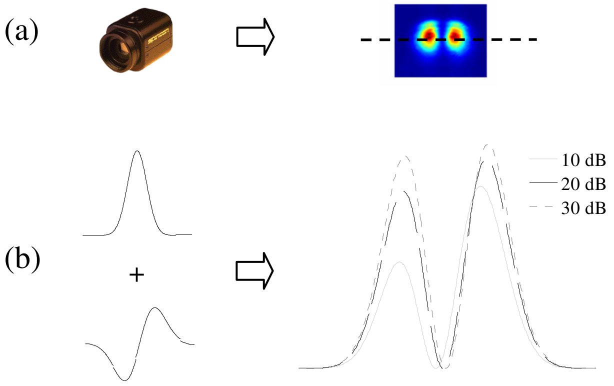

Figure 6.2: Illustration of the measurement of mode contrast out of a mode multiplexer by using a camera. (a) Mode shape recorded on a camera for an almost pure TM_{10} mode, which has two lobes. (b) Simulated cross section of the output mode (in the width dimension of the waveguide) when different power ratios (noted in the legend) between the TM_{00} and TM_{10} mode contents are considered.

Without the mode demultiplexer we can deduce the mode contrast out of the mode multiplexer by monitoring the output intensity distribution of the transmitted pump.

Almost pure TM_{00} or TM_{10} modes are obtained when we launch a CW wave near 780 nm in the TEM_{00} mode from the wide or narrow arm of the mode multiplexer for the pump. For a wave converted into almost pure TM_{10} mode, we can tune the wavelength to find the highest contrast between the peak intensities of the two lobes recorded on a camera, which is shown in Fig. 6.2(a). On the other hand, we can simulate the peak contrast between these two lobes by supposing different power ratios between the TM_{00} mode and TM_{10} mode contents, which is illustrated in Fig. 6.2(b). By comparing the measurements to the simulations we can deduce the mode contrast between the different mode contents out of a mode multiplexer. The highest mode contrast measured is >30 dB for near-780-nm waves.

6.3 Optical parametric generation involving both TM_{00} and TM_{10} waveguide modes

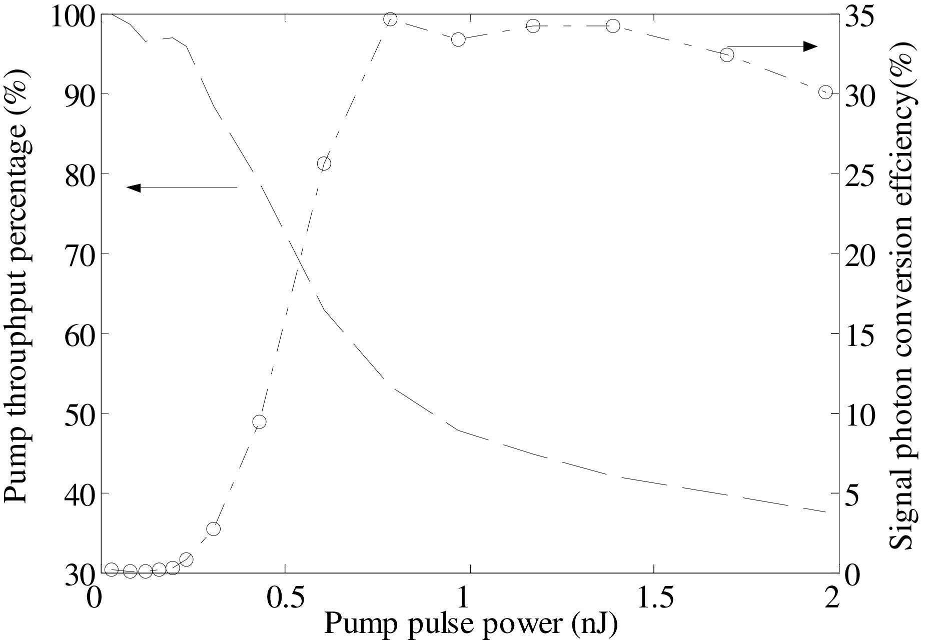

Figure 6.3: Threshold measurement for OPG with the pump in the TM_{10} mode.

Figure 6.3 shows the curves of photon conversion and pump throughput for OPG with the pump in pure TM_{10} mode. To make a fair comparison to the results in Chapter 3, the length of the QPM gratings is 42 mm and cascaded OPG processes are absent. With the pump at 785.7 nm, the OPG threshold is about 300 pJ, which is defined as when the parametric gain $G \sim \exp(2\sqrt{\eta P}L)$ reaches 100 dB. Here P is the pump power, L is the length of the gratings, and $\eta[\mathrm{W}^{-1}\mathrm{cm}^{-2}]$ is the normalized gain parameter in optical parametric amplification, which near degeneracy is equal to the normalized nonlinear conversion efficiency of second-harmonic generation. Compared to a threshold of 200 pJ and $\eta \sim 90\ \%/(\mathrm{W\text{-}cm}^2)$ with all waves in the TM_{00} mode which we demonstrated in Chapter 3, we can deduce $\eta \sim 60\%/(\mathrm{W\text{-}cm}^2)$ with the pump in the TM_{10} mode. The maximum photon conversion efficiency reaches 35% for a pump power of 780 pJ/pulse.

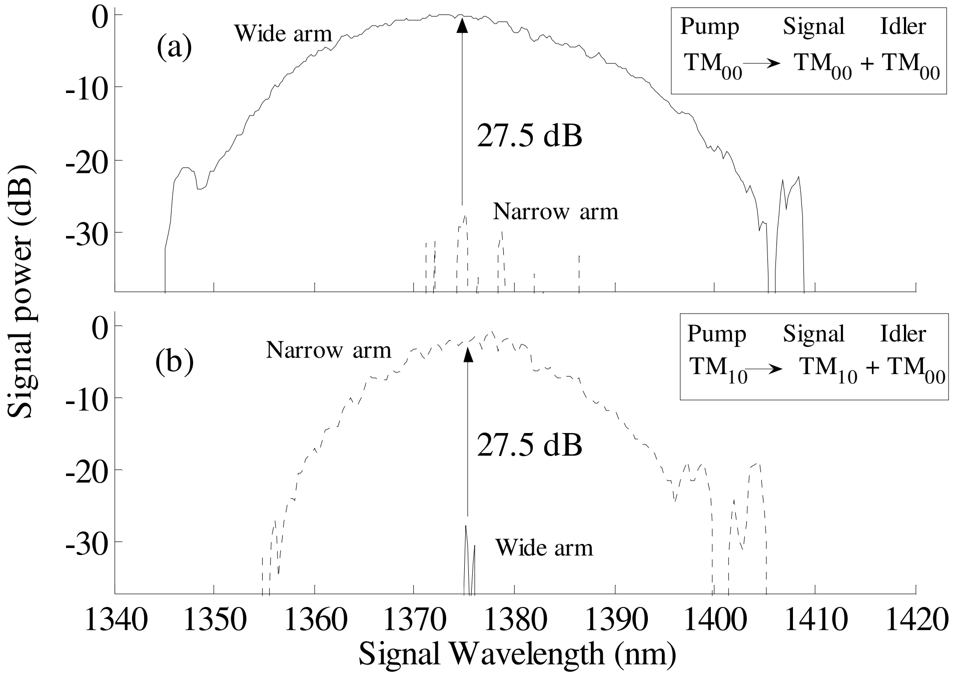

Figure 6.4: Power spectra of the OPG signal for the processes in the insets. The solid (dotted) curves show the signal emerging from the wide (narrow) arm of a mode demultiplexer. The idler near 1843 nm is not recorded.

The power spectra and wavelength tuning curves with the pump in the TM_{10} mode are more complex than those involving only TM_{00} modes, because two near-degenerate processes exist in this regime. With either the signal or the idler in the TM_{10} mode while the other is in the TM$_{00}$ mode, these two processes are separated in wavelength~~s~~ because the waveguide dispersion of the two modes are different. They are distinguishable by using asymmetric Y-junctions. Before demonstrating this behavior, we measure the mode separation ability of an asymmetric Y-junction by recording the power spectra of the signal that emerged from its two arms.

In Fig. 6.4 (a), all waves involved are in the TM$_{00}$ mode. In Fig. 6.4(b), the pump is in the TM$_{10}$ mode, the signal near 1375 nm is in the TM$_{10}$ mode while the idler near 1843 nm is in the TM$_{00}$ mode. The solid (dotted) curves are the power spectra of the signal out of the wide (narrow) arm of a mode demultiplexer; their power ratio thus gives the mode separation ability of the asymmetric Y-junction, which is 27.5 dB for both waves. Weak cascaded OPG products that we discussed in Chapter 4 appear around 1405 nm.

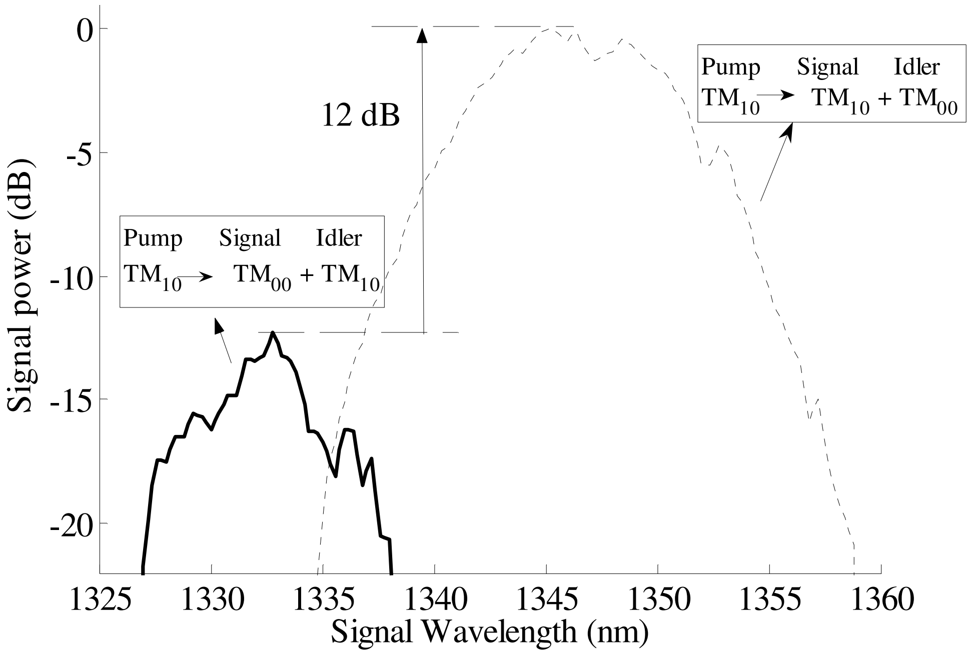

Figure 6.5: Power spectra of the OPG signal from the two near-degenerate processes with the pump in the TM$_{10}$ mode. The solid curve centered at 1332 nm shows the signal in the TM$_{00}$ mode (with the idler centered at 1908 nm in the TM$_{10}$ mode); the dotted curve centered at 1346 nm shows the signal in the TM$_{10}$ mode (with the idler centered at 1880 nm in the TM$_{00}$ mode).

With such good mode demultiplexers, we measure the signal power spectra for the two near-degenerate processes in a 14-μm-wide waveguide with the pump in the TM_{10} mode. In Fig. 6.5, the solid curve corresponds to signal in the TM_{00} mode while the dotted curve corresponds to signal in the TM_{10} mode. The idler waves in both cases are near 1.9 μm and are not shown. Simulations give a ratio of 0.7 between the normalized gain parameter η for the two cases. The parametric gain G is ~ 100 dB near the OPG threshold; G for the two cases would therefore differ by ~16 dB, matching well with the 12 dB value measured.

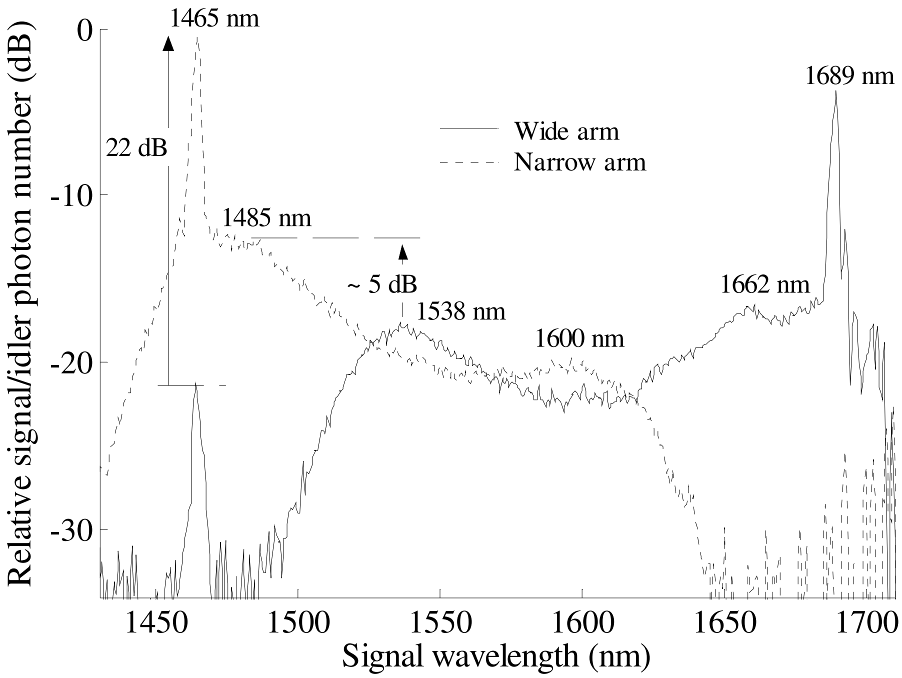

Figure 6.6: Spectra of the OPG products near degeneracy with the pump in the TM_{10} mode. The solid (dotted) curve shows the output from the wide (narrow) arm of a mode demultiplexer.

This difference in parametric gain depends on the waveguide width and the wavelengths in the interaction. For an 8-μm-wide waveguide on a different chip, this difference decreases to 5 dB when the wavelength of the pump is tuned to 784.4 nm to bring the signal and idler to near degeneracy. Fig. 6.6 shows the broad-band signal and idler near degeneracy out of the two arms of a mode demultiplexer. The solid (dotted) curve corresponds to the OPG product in the TM_{00} (TM_{10}) mode. The mode separation ability of the asymmetric Y-junctions is >20 dB from 1450 nm to 1700 nm. The sharp peaks near 1465 nm and 1689 nm are from cascaded OPG, which we discussed in Chapter 4 and would be absent in the low-gain regime if the devices are used for photon-pair sources. Other than these peaks, the curves have two pairs of peaks: 1485 nm and 1662 nm, 1538 nm and 1600 nm, corresponding to the center wavelengths of the signal and idler from the two near-degenerate processes. Due to the split of the two processes, the total bandwidth is wider than if only one process exists.

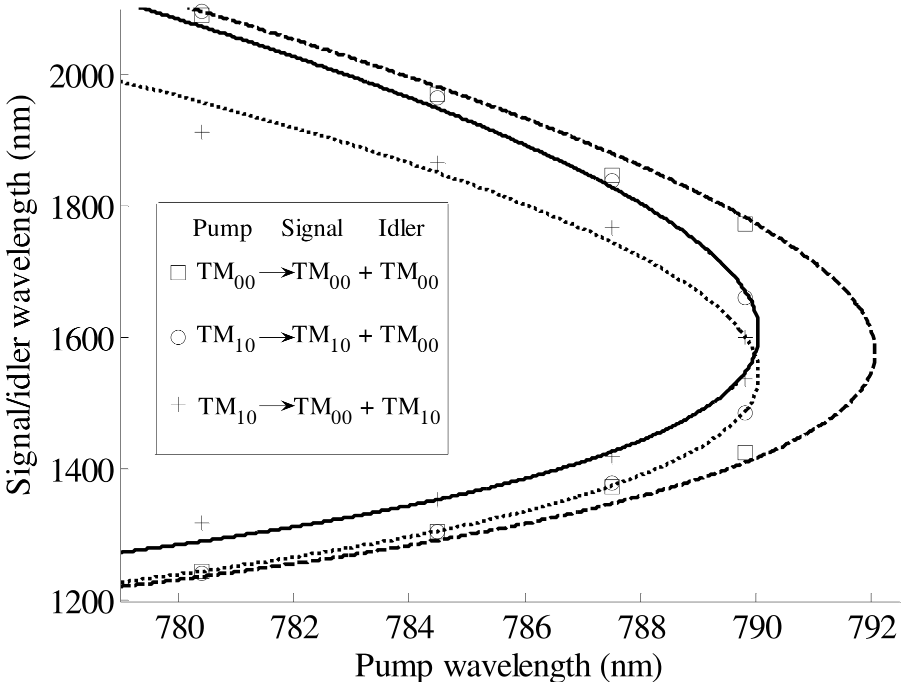

Figure 6.7: Wavelength tuning curves for OPG in a 9.5-μm-wide waveguide. The curves are from simulations. The dashed curve corresponds to OPG involving only TM_{00} modes. The solid (dotted) curve corresponds to the OPG products in the TM_{00} (TM_{10}) mode with the pump wave in the TM_{10} mode. The symbols are from measurements and correspond to the three processes in the inset.

The wavelength tuning curves for different OPG processes in a 9.5-μm-wide waveguide are deduced from the power spectra obtained at different pump wavelengths and are shown in Fig. 6.7. The curves are from simulations and the symbols are from measurements. The dashed curve corresponds to OPG with all waves in the TM_{00} mode. The solid (dotted) curve corresponds to the OPG products in the TM_{00} (TM_{10}) mode with the pump in the TM_{10} mode. The symbols correspond to the different OPG processes shown in the inset. Unlike OPG involving only TM_{00} modes, in general two pairs of signal / idler exist at every pump wavelength when the pump is in the TM_{10} mode. Moreover, instead of ending at degeneracy, the possible pump wavelength for OPG extends to where the group velocities of the signal (in the TM_{10} mode) and idler (in the TM_{00} mode) match, at the extreme point of both the solid and dotted curves in Fig. 6.7.

6.4 Summary of Chapter 6

Our waveguides with asymmetric Y-junctions are very effective in mode demultiplexing for two-mode optical parametric amplification. The mode contrast out of the mode multiplexer designed for a pump wavelength near 780 nm reached 30 dB and the mode separation ability of the mode demultiplexer designed for the signal and idler reached 27.5 dB. The threshold for OPG with the pump in the TM_{10} mode was as low as 300 pJ for 1.8-ps pump pulses near 785.7 nm and the maximum photon conversion efficiency reached 35% for a pump power of 780 pJ/pulse. We have therefore showed a new approach to generate and separate signal and idler waves for compact and efficient tunable light sources or photon-pair sources.

If a more compact waveguide structure is desired, the shape optimization in Section 6.1 may help to shorten the length of the asymmetric Y-junctions. Better control of the uniformity in mask fabrication, photolithography, proton-exchange and reverse-proton-exchange might be the key to further improving the performance of the asymmetric Y-junctions.

CHAPTER 7: SUMMARY

This chapter summarizes the work on high gain parametric processes in RPE waveguides and lists future directions and possible applications.

7.1 Summary of contributions

$\chi^{(2)}$ parametric processes with high normalized gains are important near- and mid-infrared light sources and photon pair sources. In this dissertation we have described details of high gain parametric processes in reverse-proton-exchange waveguides in three important aspects: illustrating high parametric gain, improving temporal properties of the output from picosecond OPG, and mode demultiplexing in OPA by using asymmetric Y-junctions. Our research shows that RPE waveguides and parametric processes can be well combined for practical applications. The details of the research contributions are summarized as follows.

First we demonstrated high parametric gain of RPE lithium niobate waveguides in OPA and OPG (Chapter 3). We presented CW OPA with 7 (6) dB internal (external) gain for both the signal and the idler by the cascading of SHG and OPA. In the absence of cascaded OPG, we demonstrated thresholds as low as 200 pJ for picosecond OPG. A saturated internal photon conversion efficiency of 33% was obtained with 1 nJ energy for a 1.8 ps (FWHM) pump pulse at 769.6 nm. The signal wavelength tuning range was from 1.15 μm to 2.3 μm with a pump wavelength between 770 nm and 789.5 nm.

We then demonstrated that the temporal properties of the OPG outputs can be improved by engineering either the QPM gratings (Chapter 4) or the waveguide structures (Chapter 5).

The former approach is based on cascaded OPG which involves simultaneous quasi-phase-matching of OPG and an extra process such as sum-frequency generation. By exploring OPG in devices with different QPM grating lengths and at different pump power levels, we identified and distinguished conventional OPG and cascaded OPG products in both the time domain and the frequency domain. We also characterized the temporal properties of the output from cascaded OPG using a frequency-resolved cross-correlator. We illustrated that the cascaded OPG products were near-transform-limited. We demonstrated control of the signal wavelength from cascaded OPG by using phase-modulated gratings. By switching between waveguides with different QPM grating designs and fine tuning the pump wavelengths or the device temperature, obtaining near-transform-limited and wavelength-tunable signal from cascaded OPG is possible.

The latter approach is based on quasi-group-velocity-matching (QGVM) in which we discretely and periodically change the apparent group velocities of the interacting waves. To realize QGVM we developed processes to fabricate tight bends in RPE lithium niobate waveguides with a minimum bend radius as small as 1 mm. With the QGVM scheme we improved the time-bandwidth product of the near-degenerate signal by about one order of magnitude.

After showing a low OPG threshold and the possibilities of improving the temporal properties of OPG output, we demonstrated an approach to effectively separate the signal and the idler waves by using two-mode OPA in RPE waveguides (Chapter 6). Using asymmetric Y-junctions, the mode separation ability of the mode demultiplexer designed for the signal and the idler in the 1550-nm band reached 27.5 dB. High parametric gain was retained in these devices: the threshold for OPG with the pump in the TM_{10} mode was as low as 300 pJ and the maximum photon conversion efficiency reached 35%. We have therefore illustrated a new approach to generating and separating signal and idler waves for compact and efficient tunable light sources or photon-pair sources in the communication band.

7.2 Future directions and applications

The most severe problem for OPG in current RPE waveguides is the photorefractive damage (PRD). Our RPE waveguides fabricated on z-cut congruent lithium niobate wafers were slowly damaged by green or blue waves at high pump power levels even if the chips were heated to 150 °C. An important direction for high gain parametric processes in waveguides thus is to replace congruent lithium niobate with photorefractive-damage resistant materials, such as MgO-doped or stoichiometric lithium niobate. [45, 91] We may also replace RPE waveguides with ridge waveguides since the latter can be more robust at high power levels. [45, 46] Cascaded OPG would be more useful by using these new materials since an extra wave that may cause PRD (such as the green wave generated by sum-frequency generation in Chapter 4) is essential in cascaded OPG. If the problem of PRD is solved RPE waveguides would find more applications in the high power regime.

Although we only demonstrated QGVM designs and asymmetric Y-junctions in the high power regime, in theory they can also work well in the low power regime. The methods described in Chapter 5 and Chapter 6 therefore may be applicable to optical parametric fluorescence and photon pair generation even if we use RPE waveguides in congruent lithium niobate because PRD would not occur in the low power regime. We may thereby improve the temporal properties of the outputs and enhance device integration for low power applications.

For applications such as photon-pair sources, a lower propagation loss may substantially improve the performance. [110] If the QGVM scheme is used in such applications the waveguide loss would be the bottleneck because we desire more than four QGVM sections in a single device. Fabricated by using the process we described in Section 5.1.1 with a proton-exchange depth of 2.39 μm, the tight s-bends with a minimum radius of 1 mm have no bend loss but have a much higher propagation loss than conventional RPE waveguides. To overcome this problem we may need new techniques.

If this problem of propagation loss is solved, RPE waveguides with very small bend radius would also be useful in fabricating a singly-resonant OPO on a chip. Such an OPO cavity contains a directional coupler, two asymmetric Y-junctions and two U-turn circular bends, as shown in Fig. 7.1.

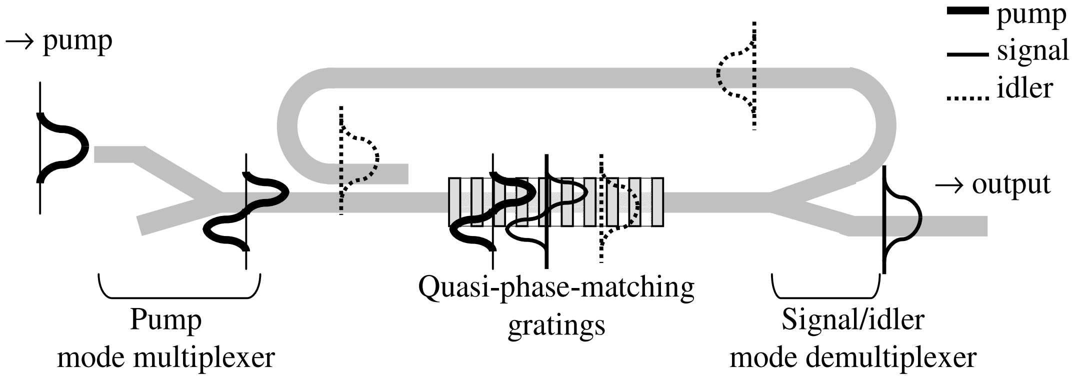

Figure 7.1: Diagram of a singly-resonant waveguide OPO on a lithium niobate chip. The main difference from Fig. 6.1 is that the idler is coupled back to form a loop by using two U-turn circular bends and one directional coupler.

Here the pump and the signal are in the TM_{10} mode while the idler is in the TM_{00} mode in the nonlinear interaction region. The asymmetric Y-junction on the input end converts the pump in the free space TEM_{00} mode into the TM_{10} waveguide mode. This asymmetric Y-junction may be unnecessary if we use tilted or staggered QPM gratings [51] and choose another parametric process in which the pump and the idler are both in the TM_{00} mode while the signal is in the TM_{10} mode.

The asymmetric Y-junction on the output side separates the signal and the idler in different modes. The signal comes out from one arm while the idler comes out from the other arm and would be fed back into the nonlinear interaction region by using two U-turn circular bends and a directional coupler. Although forming an external cavity by fiber pig-tailing may help us to build a better controlled OPO, the scheme in Fig. 7.1 is monolithic and more compact.

In the following we briefly sum up possible approaches to improve the experiments discussed in this thesis and propose further applications of them.

In Section 3.2 we discussed that the cascading of SHG and OPA resulted in 7 (6) dB internal (external) OPA gain in RPE waveguides. The parametric gain would be much higher if we pump the OPA with a 780-nm-band input wave instead of the SHG of a 1560-nm-band wave, avoiding problems that are related to pump depletion in SHG. If the problem of photorefractive damage is solved we may launch 400 mW pump power at 780 nm into the device and obtain a parametric gain >20 dB, which is comparable to EDFA. The advantages of such an OPA over EDFA include a broader bandwidth (>100 nm) and a broadly designable center wavelength for the amplification band.

In Chapter 4 we pointed out that sophisticated QPM gratings may be designed to suppress unwanted parasitic processes and enhance the cascaded processes. [30, 36] With such designs we may use the first-order QPM peaks instead of higher order QPM peaks for the extra parametric process involved in cascaded OPG and obtain a higher parametric gain for the cascaded process.

In Chapter 5 we discussed that the QGVM scheme may perform better by adding electrical-optic phase shifters in each QGVM section and synchronizing the filter effects in all the sections. The device fabrication process would require one extra lithography step for adding electrodes, which can be performed after RPE waveguides are fabricated on a full wafer. [7]

In Chapter 6 we discussed the use of asymmetric Y-junctions in OPG. They are also useful in optical systems such as compact cross-correlator or auto-correlator [111] because the performance of the mode demultiplexers using asymmetric Y-junctions is better than most filters and RPE waveguides are easy to be integrate with fiber optics by fiber-pig-tailing.

Other techniques that are not covered in this dissertation may also apply to high gain parametric processes in RPE waveguides. An example is using chirped QPM gratings. For both SHG and OPO using bulk PPLN devices, combining chirped QPM gratings with chirped pump pulses improved their performance. [55, 56] Although it cannot improve the temporal properties of the OPG outputs, after the problem of PRD is solved such a technique may be very useful for OPA, OPO or short-pulse SHG in waveguides.

BIBLIOGRAPHY

1. W. R. Bosenberg and R. C. Eckardt, *Optical Parametric Devices.* J. Opt. Soc. Am. B, 1995. **12**(11): p. 2084-2322.
2. K. R. Parameswaran, R. K. Route, J. R. Kurz, R. V. Roussev, M. M. Fejer, and M. Fujimura, *Highly efficient second-harmonic generation in buried waveguides formed by annealed and reverse proton exchange in periodically poled lithium niobate.* Optics Letters, 2002. **27**: p. 179-181.
3. M. H. Chou, K. R. Parameswaran, and M. M. Fejer, *Multiple-channel wavelength conversion by use of engineered quasi-phase-matching structures in* $LiNbO_3$ *waveguides.* Optics Letters, 1999. **24**: p. 1157-1159.
4. M. Asobe, O. Tadanaga, H. Miyazawa, Y. Nishida, and H. Suzuki, *Multiple quasi-phase-matched* $LiNbO_3$ *wavelength converter with a continuously phase-modulated domain structure.* Optics Letters, 2003. **28**: p. 558-560
5. J. R. Kurz, J. Huang, X. Xie, T. Saida, and M. M. Fejer, *Mode multiplexing in optical frequency mixers.* Optics Lett. , 2004. **29**: p. 551-553.
6. J. R. Kurz, K. R. Parameswaran, R. V. Roussev, and M. M. Fejer, *Optical-Frequency Balanced Mixer.* Opt. Lett., 2001. **26**: p. 1283-1285.
7. J. R. Kurz, *Integrated Optical-Frequency Mixers*, in *Department of Applied Physics*. 2003, Stanford University.
8. J. Huang, J. R. Kurz, C. Langrock, A. M. Schober, and M. M. Fejer, *Quasi-group-velocity matching using integrated-optic structures.* Optics Letters, 2004. **29**: p. 2482-2484.
9. S. Tanzilli, H. D. Riedmatten, H. Tittel, H. Zbinden, P. Baldi, M. D. Micheli, D. B. Ostrowsky, and N. Gisin, *Highly efficient photon-pair source using periodically poled lithium niobate waveguide.* Electronics Letters, 2001. **37**: p. 26-28.
10. A. S. Chirkin, *Entangled and squeezed photon states at consecutive and simultaneous quasi-phase-matched wave interactions.* J. Opt. B: Quantum Semiclass. Opt., 2002. **4**: p. S91-S97.
11. R. W. Boyd, *Nonlinear Optics*. 1992, San Diego, California, USA: Academic Press.
12. J. A. Amstrong, N.Bloembergen, J. Ducuing, and P. S. Pershan, *Interactions between light waves in a nonlinear dielectric.* Physical Review, 1962. **127**(6): p. 1918-1939.
13. K. J. Mcneil, P. D. Drummond, and D. F. Walls, *Self pulsing in second harmonic generation.* Opt. Commun., 1978. **27**(2): p. 292-294.
14. P. D. Drummond, K. J. McNeil, and D. F. Walls, *Nonequlibrium transitions in sub-2nd harmonic-generation.1. Semi-classical theory.* Optica Acta, 1980. **27**(3): p. 321-335.

15. X. Xie, A. M. Schober, C. Langrock, R. V. Roussev, J. R. Kurz, and M. M. Fejer, *Picojoule threshold, picosecond optical parametric generation in reverse proton-exchanged lithium niobate waveguides.* Journal of the Optical Society of America B (Optical Physics), 2004. **21**: p. 1397-1402.
16. M. H. Chou, I. Brener, M. M. Fejer, E. E. Chaban, and S. B. Christman, *1.5-μm-band wavelength conversion based on cascaded second-order nonlinearity in* $LiNbO_3$ *waveguides.* Photonics Technol. Lett, 1999. **11**(653-655).
17. M.-H. Chou, *Optical frequency mixers using three-wave mixing for optical fiber communications*, in *Department of Applied Physics*. 1999, Stanford University.
18. X. Xie, T. Saida, J. Huang, and M. M. Fejer. *Shape optimization of asymmetric Y-junction for mode multiplexing in proton-exchange lithium niobate waveguides*. in *Integrated Optics: Devices, Materials, and Technologies IX*. 2005. San Jose.
19. X. Xie and M. M. Fejer, *Two-spatial-mode parametric amplifier in lithium niobate waveguides with asymmetric Y junctions.* Optics Letters, 2006. **31**(6): p. 799-801.
20. Y. H. Xue, N. B. Ming, J. S. Zhu, and D. Feng, *The second harmonic generation in* $LiNb0_3$ *crystals with period laminar ferroelectric domains.* Chinese Phys., 1984. **4**: p. 554-564.
21. W. S. Wang, Q. Zhou, Z. H. Geng, and D. Feng, *Study of LiTaO3 crystals grown with a modulated structure: I. Second harmonic generation in LiTaO3, crystals with periodic laminar ferroelectric domains.* J. Cryst. Growth, 1986. **79**: p. 706-709.
22. G. A. Magel, M. M. Fejer, and R. L. Byer, *Quasi-phase-matched second harmonic generation of blue light in periodically poled* $LiNbO_3$. Appl. Phys. Lett., 1990. **56**: p. 108-110.
23. A. Feisst and P. Koidl, *Current induced periodic ferroelectric domain structures in* $LiNbO_3$*, applied for efficient nonlinear optical frequency mixing.* Appl. Phys. Lett., 1985. **47**: p. 1125-1127.
24. M. Okada, K. Takizawa, and S. Ieiri, *Second harmonic generation by periodic laminar structure of nonlinear optical crystal.* Opt. Commun., 1976. **18**: p. 331-334.
25. G. D. Miller, *Periodically poled lithium niobate modeling, fabrication, and nonlinear-optical performance*, in *Electrical Engineering*. 1998, Stanford University.
26. L. A. Eyres, P. J. Tourreau, T. J. Pinguet, C. B. Ebert, J. S. Harris, M. M. Fejer, L. Becouarn, B. Gerard, and E. Lallier, *All-Epitaxial Fabrication of Thick, Orientation-Patterned GaAs Films for Nonlinear Optical Frequency Conversion.* Appl. Phys. Lett., 2001. **79**: p. 904-906.
27. R. Haïdar, P. Kupecek, and E. Rosencher, *Nonresonant quasi-phase matching in GaAs plates by Fresnel birefringence.* Applied Physics Letters, 2003. **83**(8): p. 1506-1508.
28. R. Haïdar, P. Kupecek, E. Rosencher, R. Triboulet, and P. Lemasson, *Quasi-phase-matched difference frequency generation (8–13 μm) in an isotropic*

semiconductor using total reflection. Applied Physics Letters 2003. **82**(8): p. 1167-1169.

29. M. M. Fejer, G. A. Magel, D. H. Jundt, and R. L. Byer, *Quasi-Phase-Matched Second Harmonic Generation: Tuning and Tolerances.* IEEE J. Quantum. Electron. , 1992. **QE-28**: p. 2631-2654.
30. H. Liu, Y. Y. Zhu, S. N. Zhu, C. Zhang, and N. B. Ming, *Aperiodic optical superlattices engineered for optical frequency conversion.* Applied Physics Letters, 2001. **79**: p. 728-730.
31. J. Huang, X. P. Xie, C. Langrock, R. V. Roussev, D. S. Hum, and M. M. Fejer, *Amplitude modulation and apodization of quasi-phase-matched interactions.* Optics Letters, 2006. **31**(5): p. 604-606.
32. A. M. Schober, *Parametric Interactions of Short Optical Piulses in Quasi-phase-matched Nonlinear Devices*, in *Applied Physics*. 2005, Stanford University.
33. A. M. Schober, G. Imeshev, and M. M. Fejer, *Tunable-chirp pulse compression in quasi-phase-matched second-harmonic generation.* Optics Letters, 2002. **27**(13): p. 1129-31.
34. M. A. Arbore, A. Galvanauskas, D. Harter, M. H. Chou, and M. M. Fejer, *Engineerable compression of ultrashort pulses by use of second-harmonic generation in chirped-period-poled lithium niobate.* Optics Letters, 1997. **22**(17): p. 1341–1343.
35. J. R. Kurz, A. M. Schober, D. S. Hum, A. J. Saltzman, and M. M. Fejer, *Nonlinear physical optics with transversely patterned quasi-phase-matching gratings.* IEEE Journal of Selected Topics in Quantum Electronics, 2002. **8**(3): p. 660-4.
36. T. Kartaloglu, Z. G. Figen, and O. Aytur, *Simultaneous phase matching of optical parametric oscillation and second-harmonic generation in aperiodically poled lithium niobate.* Journal of the Optical Society of America B (Optical Physics), 2003. **20**: p. 343-349.
37. G. Imeshev, *Tailoring of Ultrafast Frequency Conversion with Quasi-phase-matching Gratings*, in *Applied Physics*. 2000, Stanford University.
38. M. A. Arbore, *Generation and Manipulation of Infrared Light Using Quasi-phase-matched Devices: Ultrashort-puulse, Aperiodic-grating and Guided-wave Frequency Conversion*, in *Electrical Engineering*. 1998, Stanford University.
39. G. I. Stegeman and C. T. Seaton, *Nonlinear integrated optics.* Journal of Applied Physics, 1985. **58**(12): p. R57-78.
40. G. I. A. Stegeman, D. N. Christodoulides, and M. Segev, *Optical spatial solitons: historical perspectives.* IEEE Journal of Selected Topics in Quantum Electronics, 2000. **6**(6): p. 1419-27.
41. R. L. Byer, *Parametric oscillators and nonlinear materials*, in *Nonlinear Optics*, P. G. H. a. B. S. Wherrtt, Editor. 1977, Academic Press: New York. p. 47-160.
42. K. R. Parameswaran, *Highly efficient optical frequency mixers*, in *Department of Electrical Engineering*. 2002, Stanford University.
43. D. Marcuse, *Chap. 3, Theory of Dielectric Optical Waveguides*. 1974: Academic Press.

44. A. W. Snyder and J. D. Love, *Optical waveguide theory*. 1983, London, New York: Chapman and Hall.
45. M. Asobe, H. Miyazawa, O. Tadanaga, Y. Nishida, and H. Suzuki, *A Highly Damage-Resistant Zn:LiNbO$_3$ Ridge Waveguide and its Application to a Polarization-Independent Wavelength Converter.* IEEE Journal of Quantum Electronics, 2003. **39**(10): p. 1327-1333.
46. T. Sugita, K. Mizuuchi, K. Yamamoto, K. Fukuda, T. Kai, I. Nakayama, and K. Takahashi, *Highly efficient second-harmonic generation in direct-bonded MgO:LiNbO$_3$ pure crystal waveguide* Electronics Letters, 2004. **40**(21): p. 1359-1361.
47. M. L. Bortz and M. M. Fejer, *Annealed proton-exchanged LiNbO$_3$ waveguides.* Optics Letters, 1991. **16**: p. 1844-1846.
48. J. L. Jackel and J. J. Johnson, *Reverse exchange method for burying proton exchanged waveguides.* Electronics Letters, 1991. **27**: p. 1360-1361.
49. R. Roussev, X. P. Xie, K. R. Parameswaran, M. M. Fejer, and J. Tian. *Accurate semi-empirical model for annealed proton exchanged waveguides in z-cut lithium niobate*. in *LEOS*. 2003. Tuscon, Arizona.
50. M. H. Chou, M. A. Arbore, and M. M. Fejer, *Adiabatically tapered periodic segmentation of channel waveguides for mode-size transformation and fundamental mode excitation.* Optics Letters, 1996. **21**: p. 794-796.
51. J. R. Kurz, X. P. Xie, and M. M. Fejer, *Odd waveguide mode quasi-phase matching with angled and staggered gratings.* Opt. Lett., 2002. **27**: p. 1445-1447.
52. W. K. Burns and A. F. Milton, *Mode conversion in planar dielectric separating waveguide.* J. Quantum Electron., 1975. **11**: p. 32.
53. M. L. Bortz, S. J. Field, M. M. Fejer, D. W. Nam, R. G. Waarts, and D. F. Welch, *Noncritical quasi-phase-matched second harmonic generation in an annealed proton-exchanged LiNbO$_3$ waveguide.* IEEE Journal of Quantum Electronics, 1994. **30**(12): p. 2953-60.
54. P. S. Kuo, K. L. Vodopyanov, M. M. Fejer, D. M. Simanovskii, X. Yu, J. S. Harris, D. Bliss, and D. Weyburne, *Optical parametric generation of a mid-infrared continuum in orientation-patterned GaAs.* Optics Letters, 2006. **31**(1): p. 71-73.
55. T. Beddard, M. Ebrahimzadeh, T. D. Reid, and W. Sibbett, *Five-optical-cycle pulse generation in the mid infrared from an optical parametric oscillator based on aperiodically poled lithium niobate.* Optics Letters, 2000. **25**: p. 1052-1054.
56. G. Imeshev, M. A. Arbore, M. M. Fejer, A. Galvanauskas, M. G. Fermann, and D. Harter, *Ultrashort pulse second-harmonic generation with longitudinally nonuniform quasi-phase-matching gratings: pulse compression and shaping*. J. Opt. Soc. Am. B, 2000. **17**: p. 304-318.
57. B. S. Azimov, Y. N. Kazamzin, A. P. Sukhorukov, and A. K. Sukhorukova, *Interaction of weak pulses with a low-frequency high-intensity wave in a dispersive medium.* Sov. Phys. JETP, 1980. **51**(1): p. 40-46.
58. M. Abramowitz and I. A. Stegun, *Handbook of mathematical functions*. 1972, New York, NY: Dover Publications, Inc.

59. G. P. Agrawal, *Split-step Fourier method*, in *Nonlinear Fiber Optics*. 2001, Academic Press. p. 51-55.

60. A. Seilmeier and W. Kaiser, *Generation of tunable picosecond light pulses covering the frequency range between 2700 and 32,000 cm^{-1}*. Applied Physics Letters, 1980. **23**(2): p. 113-19.

61. R. L. Byer and S. E. Harris, *Power and Bandwidth of Spontaneous Parametric Emission.* Physical Review, 1968. **168**(3): p. 1064–1068.

62. R. L. Byer, *Optical parametric oscillators*, in *Quantum Electronics:A Treatise,Volume I, Nonlinear. Optics, Part B*. 1975, Academic, NewYork, 1975. p. 587–702.

63. G. P. Agrawal, *Nonlinear Fiber Optics*. third ed. 2001: Academic Press.

64. T. Südmeyer, F. Brunner, R. Paschotta, T. Usami, H. Ito, M. Nakamura, K. Kitamura, and U. Keller. *Femtosecond optical parametric generation (OPG) in periodically poled stoichiometric $LiTaO_3$ with > 1W average power*. in *CLEO*. 2002. Long Beach, CA, USA.

65. A. Picozzi and M. Haelterman, *Influence of walkoff, dispersion, and diffraction on the coherence of parametric fluorescence.* Physical Review E, 2001. **63**(5): p. 056611(11).

66. K. A. Tillman, D. T. Reid, D. Artigas, J. Hellstro¨m, V. Pasiskevicius, and F. Laurell, *Low-threshold, high-repetition-frequency femtosecond optical parametric oscillator based on chirped-pulse frequency conversion.* J. Opt. Soc. Am. B, 2003. **20**(6): p. 1309-1316.

67. D. Artigas and D. T. Reid, *Efficient femtosecond optical parametric oscillators based on aperiodically poled nonlinear crystals.* Optics Letters, 2002. **27**(10): p. 851-853.

68. T. Südmeyer, J. A. D. Au, R. Paschotta, U. Keller, P. G. R. Smith, G. W. Ross, and D. C. Hanna, *Novel ultrafast parametric systems: high repetition rate single-pass OPG and fibre-feedback OPO.* J. Phys. D: Appl. Phys., 2001. **34**: p. 2433-2439.

69. R. Danielius, A. Piskarskas, A. Stabinis, G. P. Banfi, P. D. Trapani, and R. Righini, *Traveling-wave parametric generation of widely tunable, highly coherent femtosecond light pulses.* J. Opt. Soc. Am. B, 1993. **10**: p. 2222-2232.

70. A. V. Smith, *Group-velocity-matched three-wave mixing in birefringent crystals.* Optics Letters, 2001. **26**: p. 719-721.

71. P. D. Trapani, A. Andreoni, C. Solcia, P. Foggi, R. Danielius, A. Dubietis, and A. Piskarskas, *Matching of group velocities in three-wave parametric interaction with femtosecond pulses and application to traveling-wave generators.* J. Opt. Soc. Am. B, 1995. **12**: p. 2237-2244.

72. R. Scarmozzino, A. Gopinath, R. Pregla, and S. Helfert, *Numerical techniques for modeling guided-wave photonic devices.* IEEE Journal of Selected Topics in Quantum Electronics, 2000. **6**(1): p. 150-62.

73. K. Kawano and T. Kitoh, *Introduction to optical waveguide analysis, solving Maxwell's equations and the schrÖdinger equation*. 2001: John Wiley & Sons, Inc.

74. J. Leuthold, R. Hess, J. Eckner, P. A. Besse, and H. Melchior, *Spatial mode filters realized with multimode interference couplers.* Opt. Lett., 1996. **21**: p. 836.
75. M. Rivera, *A Finite-Difference BPM Analysis of Bent Dielectric Waveguides.* Journal of Lightwave Technology, 1995. **13**(2): p. 233-238.
76. E.-G. Neumann and R. Nat, *Curved dielectric optical waveguides with reduced transition losses.* IEE Proc Part H, 1982. **129**(5): p. 278-280.
77. A. Nesterov and U. Troppenz, *A plane-wave boundary method for analysis of bent optical waveguides.* Journal of Lightwave Technology, 2003. **21**(10): p. 2434-7.
78. J. S. Gu, P. A. Besse, and H. Melchior, *Novel method for analysis of curved optical rib-waveguides.* Electronics Letters, 1989. **25**(4): p. 278-80.
79. E. C. M. Pennings, R. J. Deri, and R. J. Hawkings, *Simple method for estimating usable bend radii of deeply etched optical rib waveguides.* Electronics Letters, 1991. **27**(17): p. 1532-1534.
80. A. Yariv and P. Yeh, *Optical waves in crystals*. 2003: John Wiley & Sons. Inc.
81. E. Kapon and R. N. Thurston, *Multichannel waveguide junctions for guided-wave optics,".* Appl. Phys. Lett., 1987. **50**: p. 1710.
82. Y. Shani, C. H. Henry, R. C. Kistler, R. F. Kazarinov, and K. J. Orlowsky, *Integrated optic adiabatic polarization splitter on silicon.* Appl. Phys. Lett., 1990. **56**: p. 120.
83. K. C. Burr, C. L. Tang, M. A. Arbore, and M. M. Fejer, *High-repetition-rate femtosecond optical parametric oscillator based on periodically poled lithium niobate.* Applied Physics Letters, 1997. **70**: p. 3341-3343.
84. T. Wilhelm, J. Piel, and E. Riedle, *Sub-20- fs pulses tunable across the visible from a blue-pumped single-pass noncollinear parametric converter.* Optics Letters, 1997. **22**: p. 1494-1496.
85. A. Galvanauskas, M. A. Arbore, M. M. Fejer, M. E. Fermann, and D. Harter, *Fiber-laser-based femtosecond parametric generator in bulk periodically poled* $LiNbO_3$. Optics Letters, 1997. **22**: p. 105-107.
86. K. Gallo, M. D. Micheli, and P. Baldi, *Parametric fluorescence in periodically poled* $LiNbO_3$ *buried waveguides.* Applied Physics Letters, 2002. **80**: p. 4492-4494.
87. M. H. Chou, J. Hauden, M. A. Arbore, and M. M. Fejer, *1.5* μm *band wavelength conversion based on difference frequency generation in* $LiNbO_3$ *waveguides with integrated coupling structures.* Opt. Lett., 1998. **23**: p. 1004-1006.
88. C. Q. Xu, H. Okayama, and Y. Ogawa, *Photorefractive damage of* $LiNbO_3$ *quasiphase matched wavelength converters.* Journal of Applied Physics, 2000. **87**(7): p. 3203-8.
89. F. Jermann, M. Simon, and E. Kratzig, *Photorefractive properties of congruent and stoichiometric lithium niobate at high light intensities.* Journal of the Optical Society of America B (Optical Physics), 1995. **12**(11): p. 2066-70.
90. Y. Furukawa, K. Kitamura, S. Takekawa, A. Miyamoto, M. Terao, and N. Suda, *Photorefraction in* $LiNbO_3$ *as a function of [Li]/[Nb] and MgO concentrations.* Applied Physics Letters, 2000. **77**: p. 2494-2496.

91. M. Katz, R. K. Route, D. S. Hum, K. R. Parameswaran, G. D. Miller, and M. M. Fejer, *Vapor-transport equilibrated near-stoichiometric lithium tantalate for frequency-conversion applications.* Optics Letters, 2004. **29**: p. 1775-1777.

92. C. Radzewicz, P. Wasylczyk, and J. S. Krasinski, *A poor man's FROG.* Optics Communications, 2000. **186**: p. 329.

93. R. Danielius, A. Piskarskas, P. D. Trapani, A. Andreoni, C. Solcia, and P. Foggi, *Visible pulses of 100 fs and 100 mJ from an upconverted parametric generator.* Applied Optics, 1996. **35**: p. 5336-5339

94. J. K. Ranka, L. Gaeta, A. Baltuska, M. S. Pshenichnikov, and D. A. Wiersma, *Autocorrelation measurement of 6-fs pulses based on the two-photon-induced photocurrent in a GaAsP photodiode.* Optics Letters, 1997. **22**: p. 1344-1346.

95. W. Schade, D. L. Osborn, J. Preusser, and S. R. Leone, *Two-color cross-correlation of fs-laser pulses by two-photon induced photoconductivity for near and far field optical measurements.* Optics Communications, 1998. **150**: p. 27-32.

96. D. H. Jundt, *Temperature-dependent Sellmeier equation for the index of refraction, n_e, in congruent lithium niobate.* Optics Letters, 1997. **22**(20): p. 1553-5.

97. M. Majd, B. Schuppert, and K. Petermann, *Low-loss Ti:LiNbO$_3$-waveguide bends prepared by MgO Indiffusion.* Journal of Lightwave Technology, 1990. **8**: p. 1670-1673.

98. C. Seo and J. C. Chen, *Low transition losses in bent rib waveguides.* Journal of lightwave technology, 1996. **14**(10): p. 2255-2259.

99. F. Laurell, J. Webjorn, G. Arvidson, and J. Holmberg, *Wet etching of proton-exchanged lithium niobate – a novel processing technique.* Journal of lightwave technology, 1992. **10**(11): p. 1606-1609.

100. M. K. Smit, E. C. M. Pennings, and H. Blok, *A normalized approach to the design of low-loss optical waveguide bends.* Journal of Lightwave Technology, 1993. **11**(11): p. 1737-42.

101. L. P. Barry, P. G. B. J. M. Dudley, J. D. Harvey, and R. Leonhardt, *Autocorrelation of ultrashort pulses at 1.5um based on nonlinear response of silicon photodiodes.* Electronics Letters, 1996. **32**: p. 1922-1923.

102. D. Marcuse, *Optimal electrode design for integrated optics modulators.* IEEE J. Quant. E., 1982. **18**: p. 393-398.

103. J. Leuthold, P. A. Besse, E. Gamper, M. Dulk, S. Fischer, and H. Melchoir, *Cascadable dual-order mode all-optical switch with integrated data- and control-signal separators.* Electron. Lett., 1998. **34**: p. 1598.

104. M. Kohtoku, H. Takahashi, T. Kitoh, T. Shibata, Y. Inoue, and Y. Hibino, *Low-loss flat-top passband arrayed waveguide gratings realised by first-order mode assistance method.* Electron. Lett. , 2002. **38**: p. 792.

105. H. Yajima, *Coupled mode analysis of dielectric planar branching waveguides.* J. Quantum Electron., 1978. **QE-14**: p. 749.

106. J. J. G. M. v. d. Tol and J. H. Laahuis, *Measurement of mode splitting in asymmetric Y-junction.* Photon. Technol. Lett., 1992. **4**(454).

107. Y. Shani, U. Koren, B. I. Miller, M. G. Young, M. Oron, and R. Alferness, *Buried rib passive waveguide Y-junction with sharp vertex on InP*. Photon. Technol. Lett. , 1991. **3**: p. 210.

108. M. H. Hu, J. Z. Huang, R. Scarmozzino, M. Levy, and R. M. J. Osgood, *A low-loss and compact waveguide Y-branch using refractive-index tapering*. Photon. Technol. Lett., 1997. **9**: p. 203.

109. T. Negami, H. Haga, and S. Yamamoto, *Guided wave optical wavelength demultiplexer using an asymmetric Y junction.* Appl. Phys. Lett. , 1989. **54**: p. 1080-1082.

110. C. Langrock, E. Diamanti, R. V. Roussev, Y. Yamamoto, M. M. Fejer, and H. Takasue, *Highly efficient single-photon detection at communication wavelengths by use of upconversion in reverse-proton-exchanged periodically poled* $LiNbO_3$ *waveguides.* Optics Letters, 2005. **30**(13): p. 1725-7.

111. S. D. Yang, A. M. Weiner, K. R. Parameswaran, and M. M. Fejer, *400-Photon-per-pulse ultrashort pulse autocorrelation measurement with aperiodically poled lithium niobate waveguides at 1.55 mm.* Optics Letters, 2004. **29**(17): p. 2070-2072.